ORNL-6100

ornl

OAK RIDGE NATIONAL LABORATORY

MARTIN MARIETTA

The $Ba(OH)_2 \cdot 8H_2O$ Process for the Removal and Immobilization of Carbon-14: Final Report

G. L. Haag
D. W. Holladay
W. W. Pitt, Jr.
G. C. Young

OPERATED BY
MARTIN MARIETTA ENERGY SYSTEMS, INC.
FOR THE UNITED STATES
DEPARTMENT OF ENERGY

Printed in the United States of America. Available from
National Technical Information Service
U.S. Department of Commerce
5285 Port Royal Road, Springfield, Virginia 22161
NTIS price codes—Printed Copy: A05 Microfiche A01

ORNL-6100
Dist. Category UC-70

Contract No. DE-AC05-84OR21400

CHEMICAL TECHNOLOGY DIVISION

NUCLEAR AND CHEMICAL WASTE MANAGEMENT

Carbon-14 Immobilization
(Activity No. AR 05 15 05 0; FTP/A No. ONL-WA05)

THE $Ba(OH)_2 \cdot 8H_2O$ PROCESS FOR THE REMOVAL AND IMMOBILIZATION OF CARBON-14: FINAL REPORT

G. L. Haag*
D. W. Holladay
W. W. Pitt, Jr.
G. C. Young

*Present address: Amoco Production Company Research Center, Tulsa, Okla.

Date of Issue - January 1986

This research was sponsored by the Office of Defense Waste and Byproducts Management, U.S. Department of Energy.

Prepared by the
OAK RIDGE NATIONAL LABORATOARY
Oak Ridge, Tennessee 37831
operated by
MARTIN MARIETTA ENERGY SYSTEMS, INC.
for the
U.S. DEPARTMENT OF ENERGY

CONTENTS

LIST OF FIGURES

LIST OF TABLES

THE $Ba(OH)_2 \cdot 8H_2O$ PROCESS FOR THE REMOVAL AND IMMOBILIZATION OF CARBON-14: FINAL REPORT

G. L. Haag*
D. W. Holladay
W. W. Pitt, Jr.
G. C. Young

ABSTRACT

The airborne release of ^{14}C from various nuclear facilities has been identified as a potential biohazard due to the long half-life of ^{14}C (5730 years) and the ease with which it may be assimilated into the biosphere. At ORNL, technology has been developed for the removal and immobilization of this radionuclide. Prior studies have indicated that ^{14}C will likely exist in the oxidized form as CO_2 and will contribute slightly to the bulk CO_2 concentration of the gas stream, which is air-like in nature (~300 ppm_v CO_2). The technology that has been developed utilizes the CO_2–$Ba(OH)_2 \cdot 8H_2O$ gas-solid reaction with the mode of gas-solid contacting being a fixed bed. The product, $BaCO_3$, possesses excellent thermal and chemical stability, prerequisites for the long-term disposal of nuclear wastes. For optimal process operation, studies have indicated that an operating window of adequate size does exist. When operating within the window, high CO_2 removal efficiency (effluent concentrations <100 ppb_v), high reactant utilization (>99%), and an acceptable pressure drop across the bed (3 kPa/m at a superficial velocity of 13 cm/s) are possible. Three areas of experimental investigation are reported: (1) microscale studies on 150-mg samples to provide information concerning surface properties, kinetics, and equilibrium vapor pressures; (2) macroscale studies on large fixed beds (4.2 kg of reactant) to determine the effects of humidity, temperature, and gas flow rate upon bed pressure drop and CO_2 breakthrough; and (3) design, construction, and operation of a pilot unit capable of continuously processing a 34-m^3/h (20-ft^3/min) air-based gas stream.

1. INTRODUCTION

The airborne release of ^{14}C from the nuclear fuel cycle has been identified as a potential biohazard due to the long half-life of ^{14}C

*Present address: Amoco Production Company Research Center, Tulsa, Okla.

(5730 years) and the ease with which it may be assimilated into the biosphere.[1-20] At Oak Ridge National Laboratory (ORNL) technology has been developed (as part of the Airborne Waste Management Program) for the removal and immobilization of this radionuclide which is a weak -emitter. Prior studies have indicated that ^{14}C will likely exist in the oxidized form as CO_2 and will contribute slightly to the bulk CO_2 concentration of the gas stream, which is air-like in nature (~330 ppm_v CO_2) due to various air inleakages and purges.

In the development of a technology for controlling the release of ^{14}C from the nuclear fuel cycle, the following criteria were established for candidate processes:

1. acceptable process efficiency, with a nominal decontamination factor of 10;
2. acceptable final product form for long-term waste disposal;
3. excellent on-line process characteristics;
4. process operation at near-ambient conditions; and
5. acceptable process costs (<$10/man-rem).

Based upon these criteria, an operationally simple process based on the reaction $Ba(OH)_2 \cdot 8H_2O + CO_2 \rightarrow BaCaO_3 + 9H_2O$ and utilizing fixed-bed canisters of barium hydroxide has been developed at ORNL. At ambient temperatures and pressures, this process is capable of removing CO_2 (330 ppm_v) in air to concentrations of <100 ppb_v. Thermodynamic calculations indicate equilibrium concentrations to be at the part-per-trillion level.[21,22] The product, $BaCO_3$, possesses excellent thermal and chemical stability since it decomposes at 1450°C and is sparingly soluble in water (0.124 mmol/L at 25°C).[23,24] Furthermore, the soluble reactant undergoes 100% conversion, thus ensuring an extremely stable material for final disposal. Gas throughputs are such that reactor size remains practical for the treatment of anticipated process streams. For a design superficial velocity of 13 cm/s, a reactor with a diameter of 0.70 m (27 in.) would be required for the treatment of a 170-m^3/h (100-ft^3/min) off-gas stream with a CO_2 content of 330 ppm_v. Although extensive cost studies have not been completed, initial comparative studies with alternative technologies have indicated the process to be extremely cost competitive.[16,20,25-33] The estimated process cost is <$10/man-rem.

For an in-depth review of $Ba(OH)_2$ hydrate chemistry and its reactivity toward CO_2, refer to ref. 32. The intent of the next three sections will be to document the reactant used in these studies and to highlight the results of the micro- and bench-scale experimental studies as reported in ref. 22.

2. $Ba(OH)_2 \cdot 8H_2O$ REACTANT

Experimental studies concentrated upon the use of flakes of $Ba(OH)_2 \cdot 8H_2O$. These studies showed that this chemical species was more reactive toward CO^2 than either the tri- or mono-hydrate. The material (Fig. 1) is a free-flowing solid and when reacted with CO_2 under proper conditions, the flake form remains intact upon conversion to $BaCO_3$. Vendor specifications indicate that the material is substoichiometric in water and possesses an overall hydration of 7.0 to 7.9 H_2O. Discussions with the vendor indicated that the water deficiency is intentional so as to ensure a free-flowing, nonsticking product.

The flakes are prepared by distributing a $Ba(OH)_2$ hydrate magma (~78°C) on a stainless steel conveyor belt, which is cooled on the underside with cooling water.[34] The resulting flakes have variable thicknesses [an average thickness ~0.10 cm (1/16 in.)]. The results of a particle-size analysis on material originating from two batches are presented in Table 1. Analysis of samples obtained from these batches indicated stoichiometries of approximately 7.5 and 7.0 H_2O, respectively. For a given batch, little variation was observed in the extent of hydration. X-ray analysis of the two samples failed to confirm the presence of $Ba(OH)_2 \cdot 3H_2O$, the next stable hydrate of lower stoichiometry. However, the existence of a $Ba(OH)_2 \cdot 3H_2O$—$Ba(OH)_2 \cdot 8H_2O$ eutectic with an overall water stoichiometry of 7.19 has been reported.[35,36] We speculated that the trihydrate species was not detected because of its extremely small crystallite size. Sorption isotherm studies indicated that the reactant displayed negligible microporosity ($d < 2$ nm) or restrictive mesoporosity ($2 \text{ nm} < d < 150$ nm). Mercury porosimetry studies indicated that the pore

ORNL-Photo 6941-81

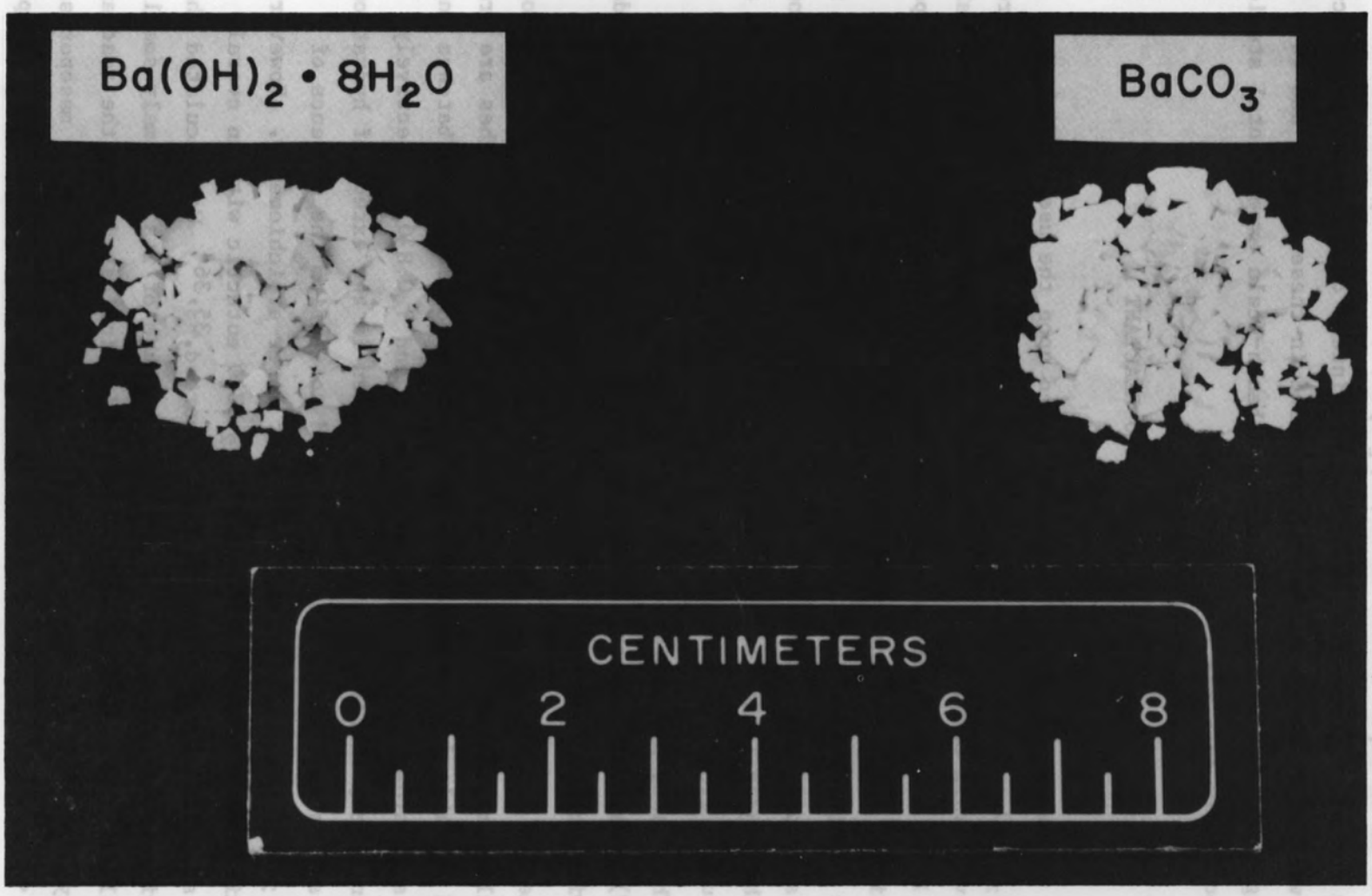

Fig. 1. Photograph of commercial $Ba(OH)_2 \cdot 8H_2O$ flakes and $BaCO_3$ flake product. The product was obtained at a process relative humidity <60%. (Original photograph: 7.3 by 9.5 cm, magnification, 16.5 and 13X, respectively.)

Table 1. Particle-size analysis of commercial $Ba(OH)_2 \cdot 8H_2O$ flakes obtained from two different batches

Particle size		Weight percent	
Mesh	mm	Batch 1	Batch 2
4 →	4.75	18.5	5.8
8 → 4	2.36 → 4.75	46.9	33.0
20 → 8	0.850 → 236	31.6	54.5
50 → 20	0.300 → 0.850	2.0	4.9
120 →	0.125 → 0.300	0.4	1.2
→ 120	→ 0.125	0.6	0.6

size distribution was bimodal with maxima of 0.17 and 1.0 μm and that the flake porosity was 12%. When a flake was exposed to a water vapor pressure less than or greater than the vapor pressure of $Ba(OH)_2 \cdot 8H_2O$, the material either dehydrated to the trihydrate or hydrated to the octahydrate. Rehydration was observed to proceed in one of two regimes and was dependent upon the relative humidity. This factor will be addressed in subsequent sections. The best correlation for predicting the vapor pressure of $Ba(OH)_2 \cdot 8H_2O$ appears to be that presented by Kondakov et al.:[37]

$$\log P = -\frac{58230}{19.155T} + 13.238,$$

where

P = pressure, Pa or N/m^2,

T = temperature, K.

A comprehensive, chronological review of the published vapor pressure data on $Ba(OH)_2 \cdot 8H_2O$ is presented in ref. 22.

Operating conditions exist for which the integrity of the flake form is retained upon conversion to $BaCO_3$. Because of the low molar volume of the product as compared to that of the reactant (a ratio of 0.31) and an initial particle voidage of 12%, one would predict a final product porosity of 73%. Mercury porosimetry studies have shown product porosities of 66 to 72%. Visual evidence of this porosity may be observed by comparing scanning electron micrographs of the reactant and product (Fig. 2).

The following $Ba(OH)_2$ hydrate nomenclature will be used in the remainder of this paper: The substoichiometric flakes will be referred to as commercial $Ba(OH)_2 \cdot 8H_2O$ (7.5). Where it is of significance, the term in parenthesis will refer to the initial hydration stoichiometry. The term $Ba(OH)_2 \cdot 8H_2O$ will refer to the stable crystalline species with 8 waters of hydration.

3. MICROSCALE STUDIES

Basic studies were conducted on the hydrates of $Ba(OH)_2$ and the $BaCO_3$ product realizing that an understanding (or at least an awareness) of phenomena which occur on the microscale is often required to develop an understanding of macroscale phenomena. Analytical techniques consisted of: (1) scanning electron microscopy; (2) mercury intrusion for porosimetry determination; (3) acid-base titrations and overall mass balances to determine the extent of conversion and hydration; (4) x-ray diffraction analysis; (5) single-point BET analysis; and (6) operation of a microbalance system whereby studies of a kinetic, thermodynamic, and surface morphological nature could be performed on 150-mg samples (Figs. 3 and 4). Results from these studies were useful in the characterization of the $Ba(OH)_2 \cdot 8H_2O$ reactant, which was reported in the preceding section. The intent of this section is to highlight experimental results from the microscale studies, which are as follows:

ORNL-Photo 1305-83

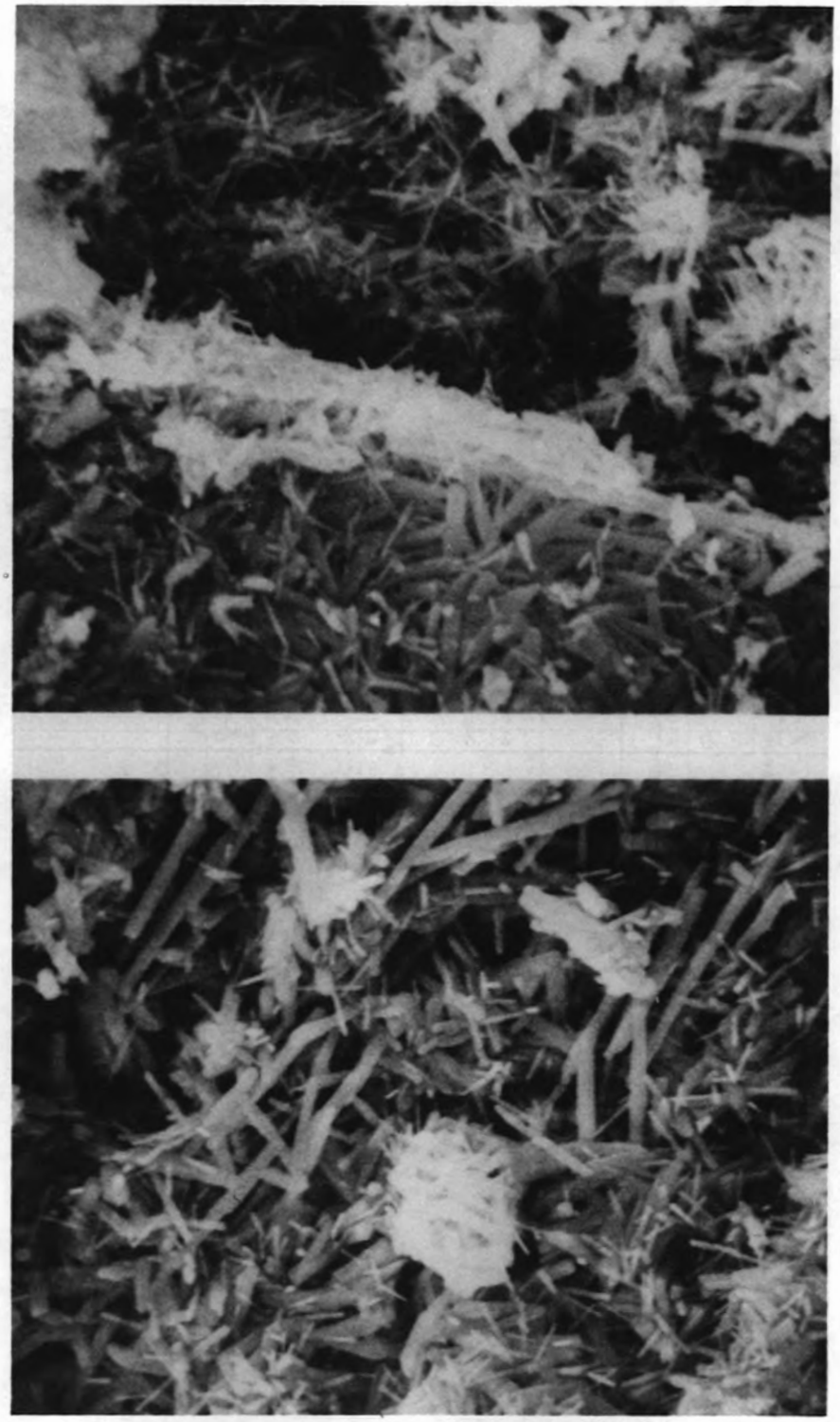

Fig. 2. Scanning electron micrographs of a flake of commercial $Ba(OH)_2 \cdot 8H_2O$ (top) and the $BaCO_3$ product. The product was obtained at a process humidity <60% (original photo, 8.9 x 11.4 cm; magnification, 5000x).

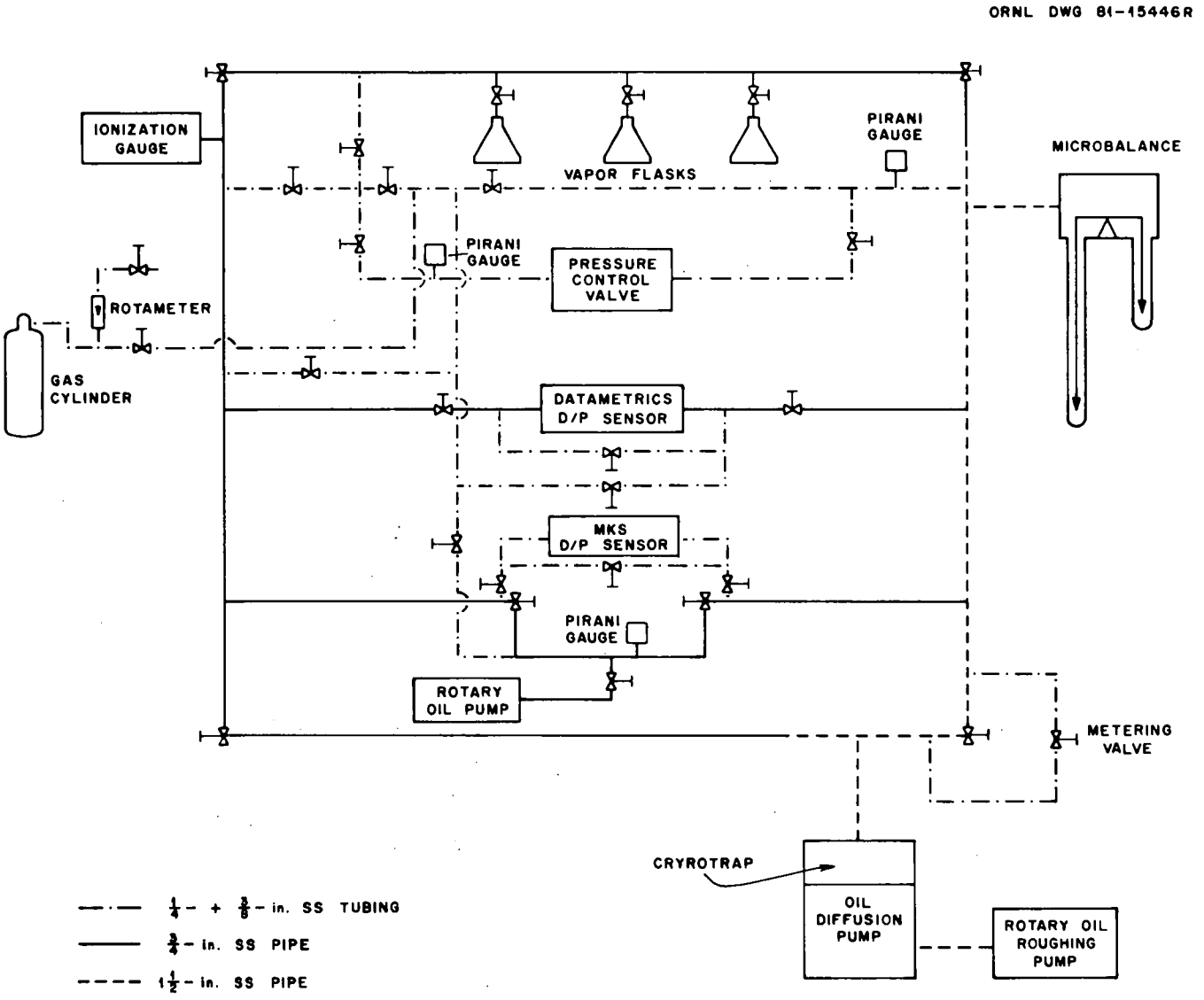

Fig. 3. Schematic of the microbalance system.

ORNL-Photo 8162-81

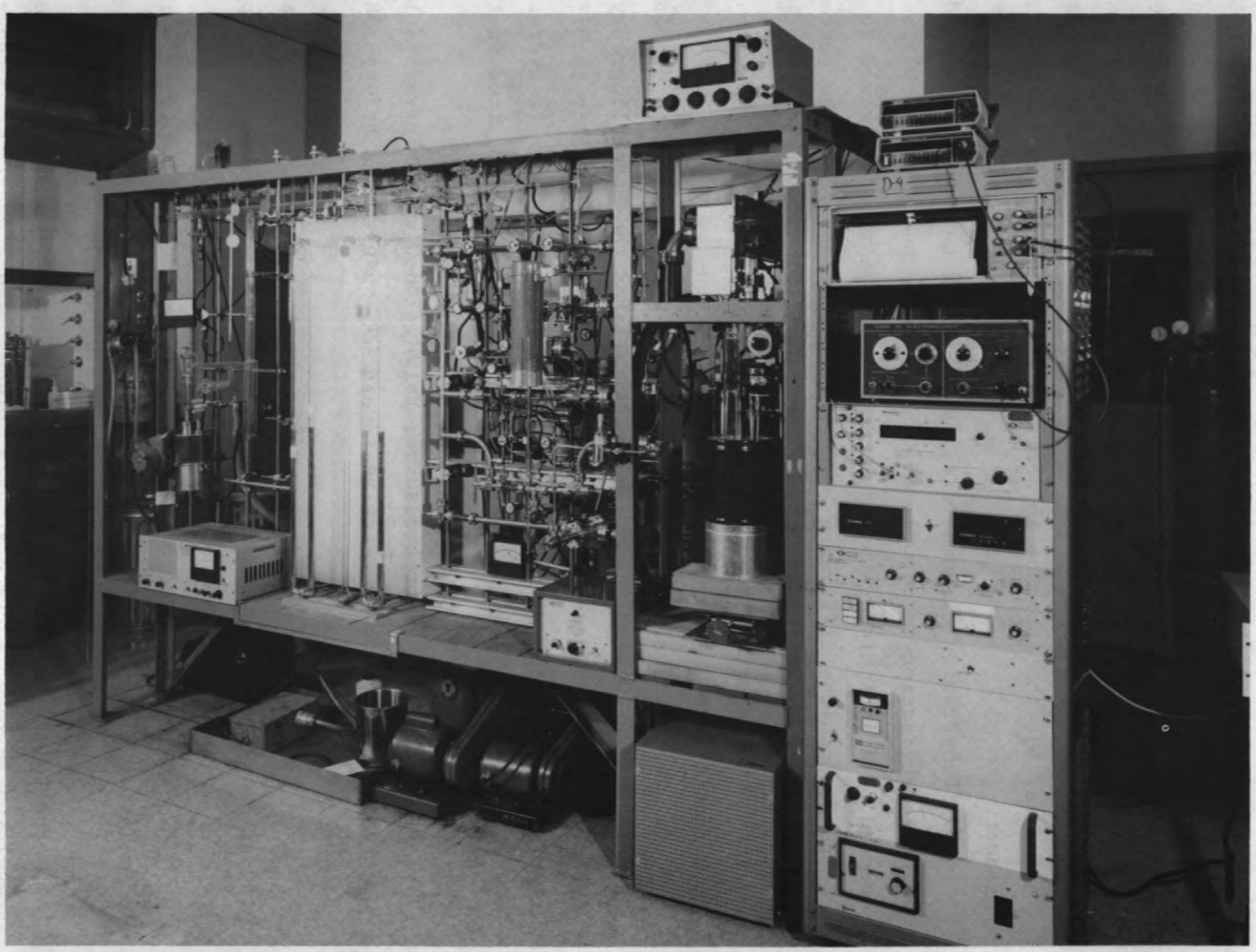

Fig. 4. Photograph of microbalance system.

1. Methods to prepare $Ba(OH)_2 \cdot H_2O$, $Ba(OH)_2 \cdot 3H_2O$, and $Ba(OH)_2 \cdot 8H_2O$ were developed, and the presence of these species was confirmed.

2. Commercial $Ba(OH)_2 \cdot 8H_2O$ flakes were found to display negligible surface area. Hydration to $Ba(OH)_2 \cdot 8H_2O$ was observed to proceed in one of two regimes. For relative humidities <60%, the increase in surface area was small and the flake form remained intact. For relative humidities >60%, the flake recrystallized in a manner which resulted in greater surface area, but the increase in activity also resulted in a more fragile product.

3. Dehydration of commercial $Ba(OH)_2 \cdot 8H_2O$ to $Ba(OH)_2 \cdot 3H_2O$ and subsequent rehydration to $Ba(OH)_2 \cdot 8H_2O$ at relative humidities <60% was modeled by a shrinking core model. The relative rate was found to be dependent upon the difference between the water sorbed on the surface for a given P/P_0 value (i.e., fraction of saturation pressure or relative humidity/100) and that required on the surface for $Ba(OH)_2 \cdot 8H_2O$ to exist in a stable form.

4. There was evidence of considerable hydrogen bonding within the $Ba(OH)_2 \cdot 8H_2O$ crystal. These results paralleled the crystallography studies of Monohar and Ramaseshan in which they cited difficulty in differentiating the location of the hydroxyl ions from the waters of hydration.[38]

5. The vapor pressure correlation for $Ba(OH)_2 \cdot 8H_2O$ cited in the previous section was indirectly verified at two temperatures.

6. At low CO_2 vapor pressures, $Ba(OH)_2 \cdot 8H_2O$ was observed to be three orders of magnitude more reactive toward CO_2 than either $Ba(OH)_2 \cdot 3H_2O$ or $Ba(OH)_2 \cdot H_2O$.

7. For relative humidities <60%, the increase in surface area with product conversion was found to be a very strong function of the specific rate of reaction and was not a linear function of conversion.

8. The surface area of $BaCO_3$ product was determined to be a function of relative humidity. In a manner analogous to the dehydration of commercial $Ba(OH)_2 \cdot 8H_2O$ and the rehydration of $Ba(OH)_2 \cdot 3H_2O$, surface water appeared to aid in the transport of the reactant and product species, thus resulting in lower surface areas at higher values of P/P_0. However, the authors feel that the increase in surface water could not account for the

drastic difference in CO_2 reactivity observed for the various hydrate species. The difference in reactivity appears to result from the additional water in the crystal structure and the greater mobility of the hydroxyl ions.

9. Since analysis of nitrogen sorption isotherm data gave no indications of hysteresis, if capillary condensation should occur, one would speculate it would result from the wall effects of noncircular pores (e.g., V-shaped points of intersurface contact). Detailed information appears in ref. 22.

4. FIXED-BED MICROSCALE STUDIES

Over 18,000 hours of experimental operating time have been completed on fixed beds of $Ba(OH)_2 \cdot 8H_2O$. These beds (10.2-cm ID x 30 to 50-cm length) typically contained 2.9 to 4.3 kg of reactant. A schematic of the experimental system, which has been described in detail in a previous paper,[22] is presented in Fig. 5. The intent of this aspect of the study was to determine the effects of air flow rate (superficial gas velocities of 7 to 21 cm/s), operating temperature (22 to 42°C), and water vapor pressure or relative humidity (0 to 80%) on the operational characteristics of the fixed bed, most notably (1) the shape of the breakthrough curve and (2) the pressure drop across the fixed bed. Since the reaction is endothermic, the reactor was jacketed and the temperatures of the influent and effluent streams were held constant. Figure 6 presents a typical breakthrough curve and pressure drop plot. For this particular run, the pressure drop increase was noticeable and was not solely a function of bed conversion.

In the course of these fixed-bed studies, it was observed that for a given mass throughput, certain process conditions resulted in a greater pressure drop than others. In several instances, the increase in pressure drop during a run behaved in an autocatalytic manner and necessitated discontinuation of the run. The increase in pressure drop appeared to result from two phenomena: (1) a slow gradual increase that was a function

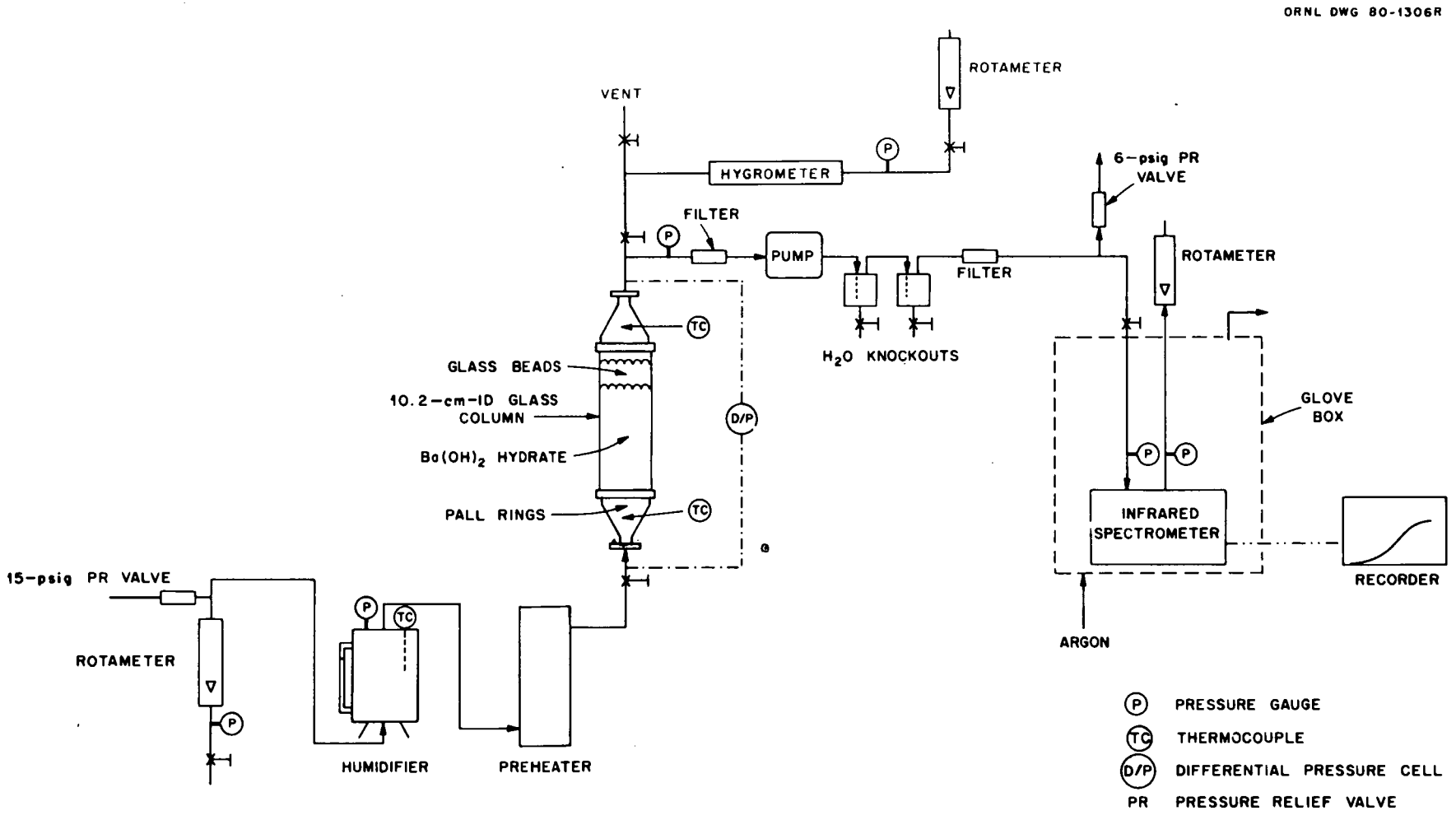

Fig. 5. Schematic of the fixed-bed experimental equipment.

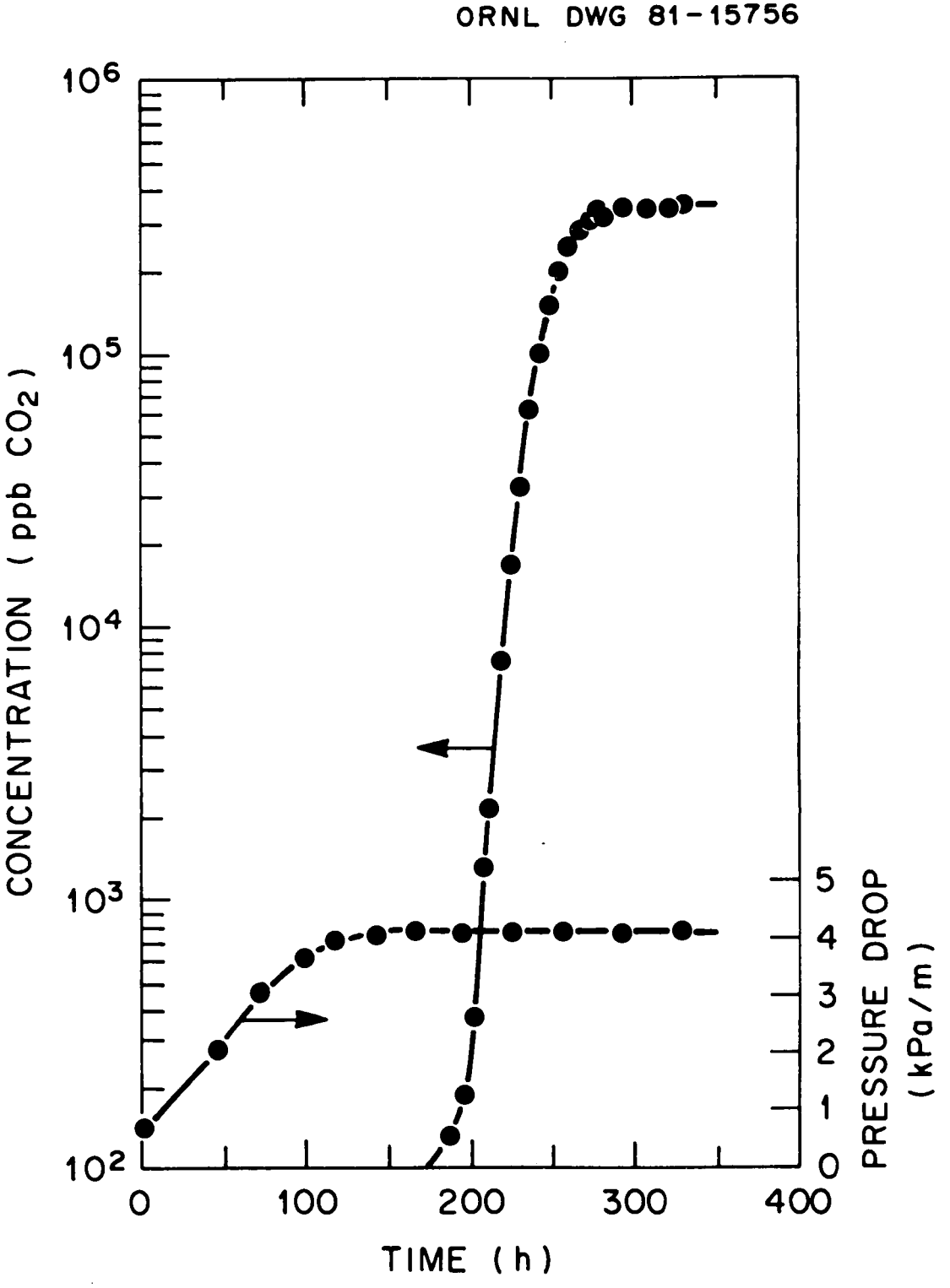

Fig. 6. Logarithm of the experimental breakthrough profile and the change in pressure drop across the bed presented as function of time (superficial gas velocity, ~13 cm/s).

of bed conversion and (2) a rapid increase that was a function of relative humidity. The magnitude of the latter often overshadowed the former. The observed pressure drop, plotted as a function of relative humidity at two temperatures (295 and 305 K) and a superficial velocity of ∿13 cm/s, is presented in Fig. 7. It is significant that the data are consistent at the two temperatures even though the saturation vapor pressures differed by a factor of 1.8. Furthermore, the dependency upon relative humidity indicates the presence of a surface adsorption phenomenon. For physical adsorption on surfaces, the extent of adsorption is dependent upon the extent of saturation, P/P_0, or in the case of water, the relative humidity. The fact that the pressure drop became more severe at ~60% relative humidity indicates that capillary condensation is likely present. Since no hysteresis was observed during nitrogen adsorption studies, we can speculate that the condensation occurs at V-shaped contact points or pores. The presence of the condensed water then provides sites of rapid recrystallizaton. Because the flaked reactant was prepared by the rapid cooling of a magma that was substoichiometric in octahydrate (7.0 to 7.9 waters of hydration), the rate of recrystallization is very likely enhanced by a need to reduce internal energy locked within the flake. This energy may be present as defects within the crystallites or surface energy resulting from the small size of the crystallites and the presence of the $Ba(OH)_2 \cdot 3H_2O$—$Ba(OH)_2 \cdot 8H_2O$ eutectic. Photographs of commercial $Ba(OH)_2 \cdot 8H_2O$ flakes after recrystallization at a relative humidity >60% are presented in Fig. 8. For rehydration at lower humidities, external changes of the flake were small.

The functional dependency of pressure drop upon relative humidity is helpful in understanding the autocatalytic pressure drop behavior observed at high relative humidities. For a fixed influent water vapor concentration, any increase in system pressure at constant temperature will result in an increase in the water vapor pressure and likewise the relative humidity, P/P_0. Therefore, as the pressure drop across the bed increases, so does the relative humidity within the bed and each continues

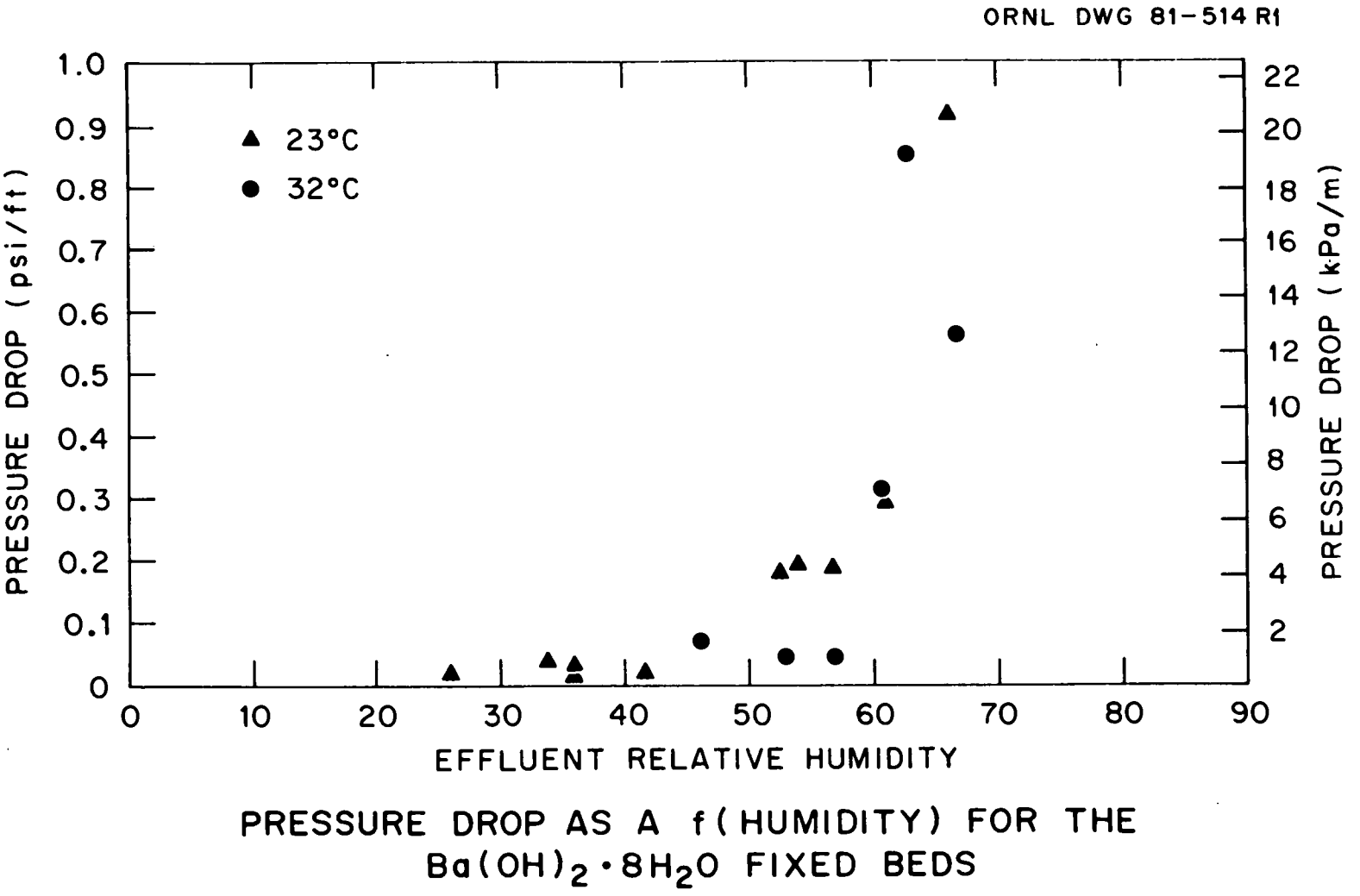

Fig. 7. Pressure drop as a function of relative humidity during fixed-bed studies on commercial $Ba(OH)_2 \cdot 8H_2O$ flakes, reference superficial gas velocity of ~13 cm/s.

ORNL-Photo 1306-83

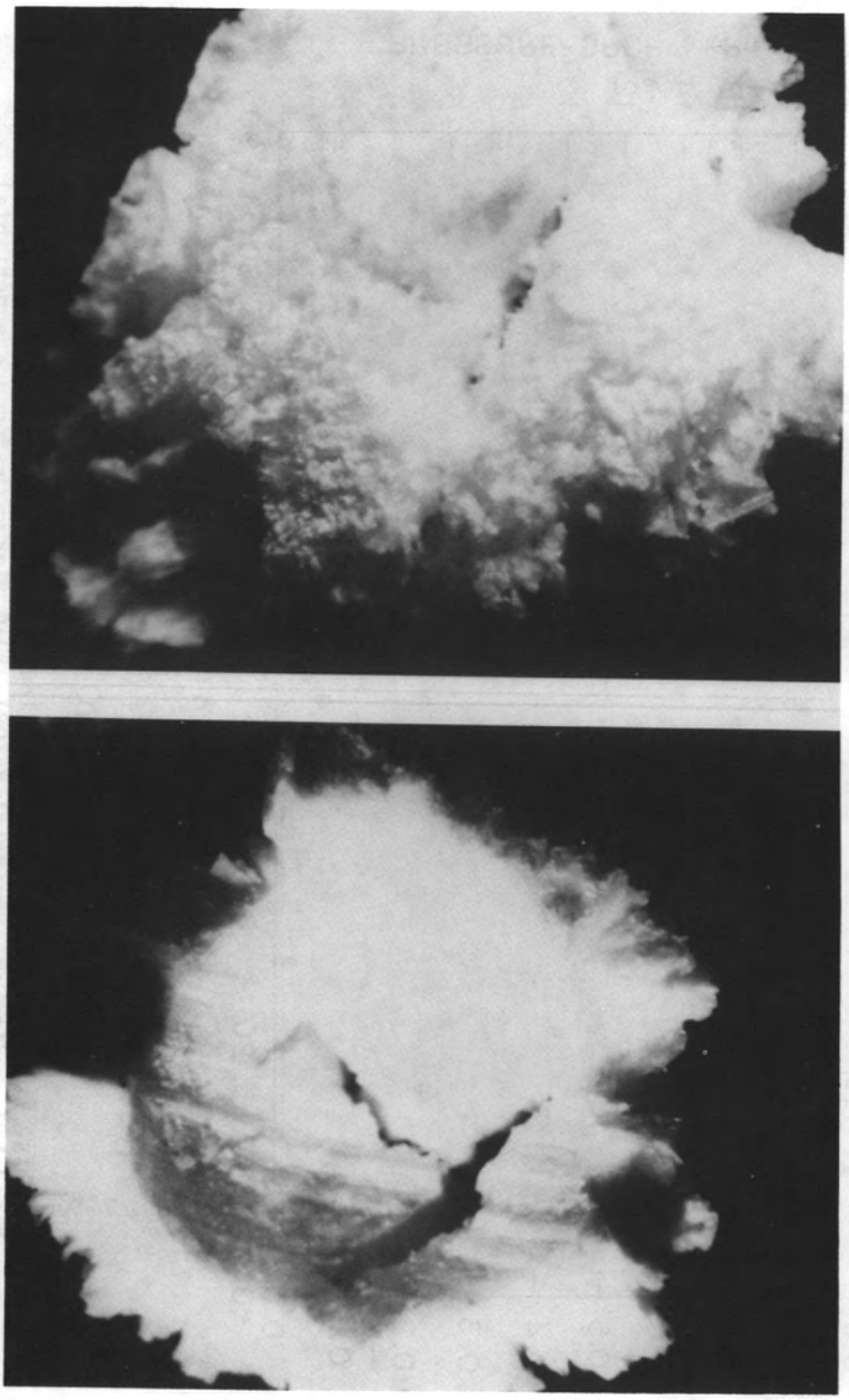

Fig. 8. Top and bottom views of a commerical $Ba(OH)_2 \cdot 8H_2O$ flake subjected to relative humidity >60%. (Original photograph: 2.85 by 3.75 in.; magnification, 16.5 and 13X, respectively.

to increase until the run must be terminated. At lower relative humidities, the rate of increase in pressure drop as a function of relative humidity is not sufficient to autocatalyze the process.

The pressure drop dependency upon relative humidity also restricts the upper flow rate that the process may treat. Increased gas flows result in greater pressure drops across the bed (i.e., a greater pressure at the entrance to the bed). Therefore, the relative humidity at the entrance of the bed must be <60%, but the influent water vapor pressure must be greater than the dissociation vapor pressure of $Ba(OH)_2 \cdot 8H_2O$.

Extensive modeling studies were performed on the breakthrough curves from the fixed-bed studies. Because of the nature of the governing partial differential equations and their respective boundary conditions, solutions were of a numerical nature. An in-depth review of the method of analysis and of the associated assumptions is presented elsewhere.[22] The analysis indicated that the rate expression could be modeled by an equation of the form:

$$R = K_F A_0 (1 - X) C,$$

where

K_F = gas film mass transfer coefficient,
A_0 = initial surface area available for mass transfer,
X = fractional conversion of reactant,
C = bulk CO_2 concentration.

Data analysis indicated $K_F A_0$ to be a weak function of temperature and a strong function of velocity, indicative of gas-film control. Considerable dispersion in the value of the $K_F A_0$ coefficients was observed for a given mass throughput. There were indications that the dispersion resulted from differences in the actual area available for mass transfer and the possible presence of localized channeling. Based upon published correlations for the K_F coefficient, the correlation for the $K_F A_0$

coefficient possessed a greater functional dependency upon velocity than expected. However for representative values of A_0, the magnitude of K_F was characteristic of reported values in the literature. Because the studies were conducted on flaked material with considerable interparticle contact, we speculate that the amount of surface area available for mass transfer increased as a function of gas velocity, thus resulting in the greater than anticipated functional dependency of K_FA_0 upon velocity. This factor may also account for the greater than anticipated dispersion in K_FA_0 as some localized packing arrangements would be more conducive to restructuring. Representative breakthrough curves and the model-predicted curves are presented in Fig. 9.

5. PILOT DEVELOPMENT STUDIES

The next step in the development of this technology for ^{14}C control was the design, construction, and operation of a pilot-scale process. Specific goals of this aspect of process development were to provide:

1. the basis for the design of a ^{14}C immobilization module for future testing under radioactive conditions;
2. data at operating conditions not achievable with present bench-scale equipment, in particular, operation at near-adiabatic conditions;
3. necessary scale-up data; and
4. operating data on key hardware items and instrumentation.

Figure 10 gives a flow schematic of the ^{14}C immobilization pilot unit; a photograph of the system is presented in Fig. 11. The designed gas throughput at a superficial velocity of 13 cm/s in the reactor is 34 m^3/h (20 ft^3/min). The system consists of two reactors which contain 30.5-cm-ID canisters loaded with 32 kg (70 lb) of commercial $Ba(OH)_2 \cdot 8H_2O$ reactant. A second cannister, 24.4-cm-ID, enabled process operation at a superficial velocity of 20 cm/s for the previously referenced flow rate of 34 m^3/h. Continuous operation of the process is possible because of the size of the canisters and the relatively long loading times prior to CO_2

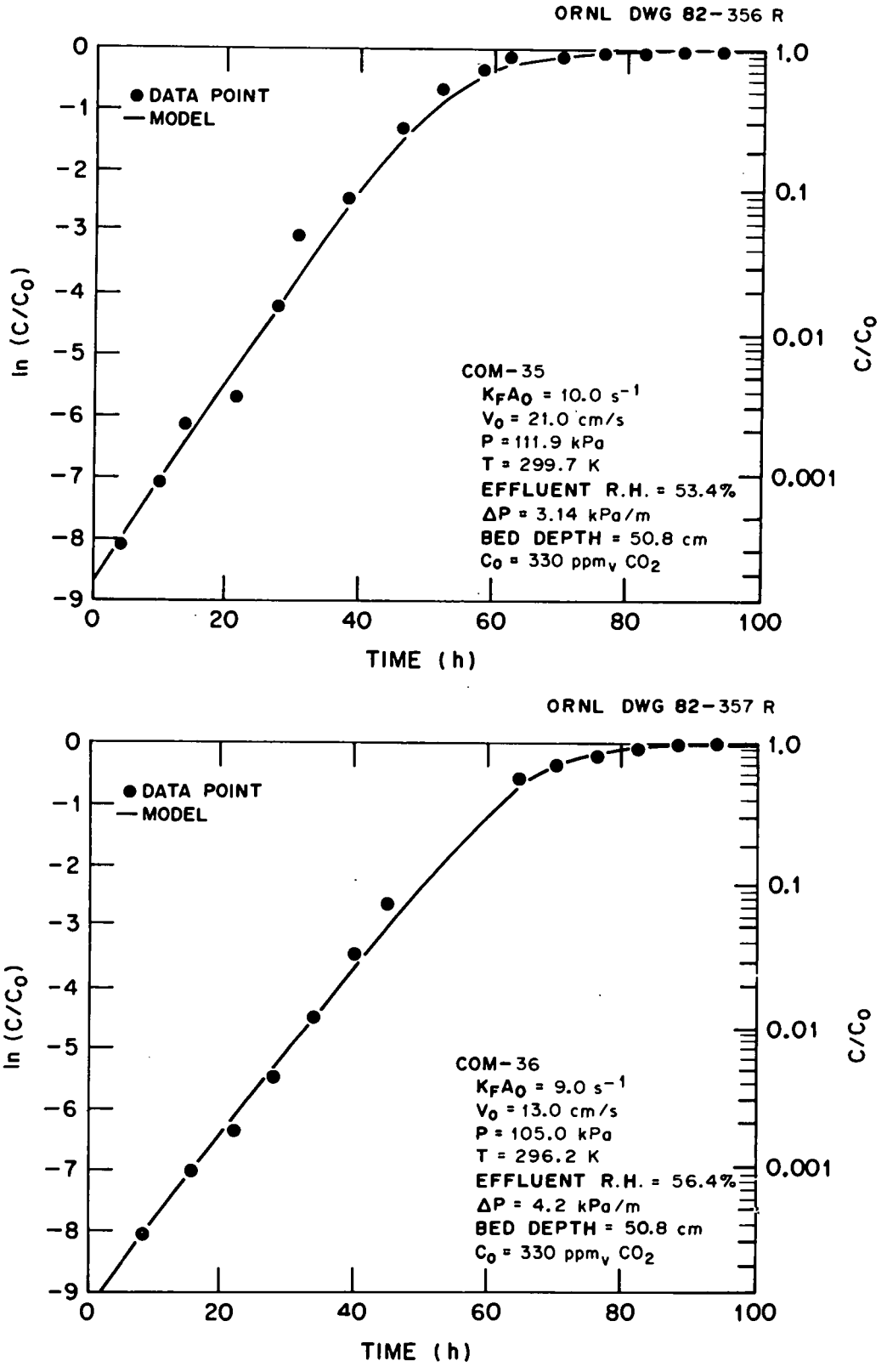

Fig. 9. Breakthrough curves and model-predicted breakthrough curves for typical 10.2-cm-ID fixed-bed runs.

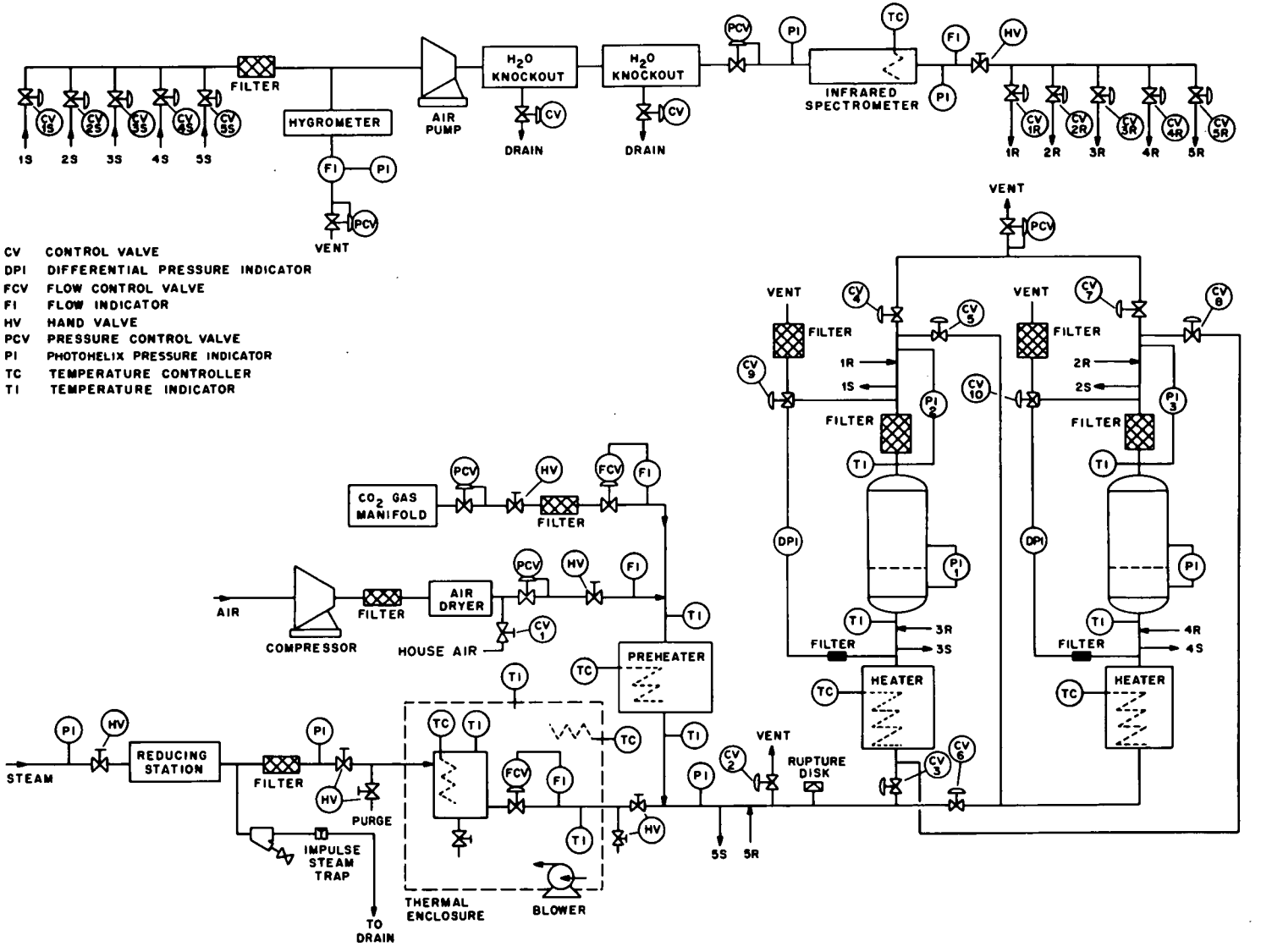

Fig. 10. The ^{14}C-immobilization pilot unit.

ORNL-Photo 2415-82

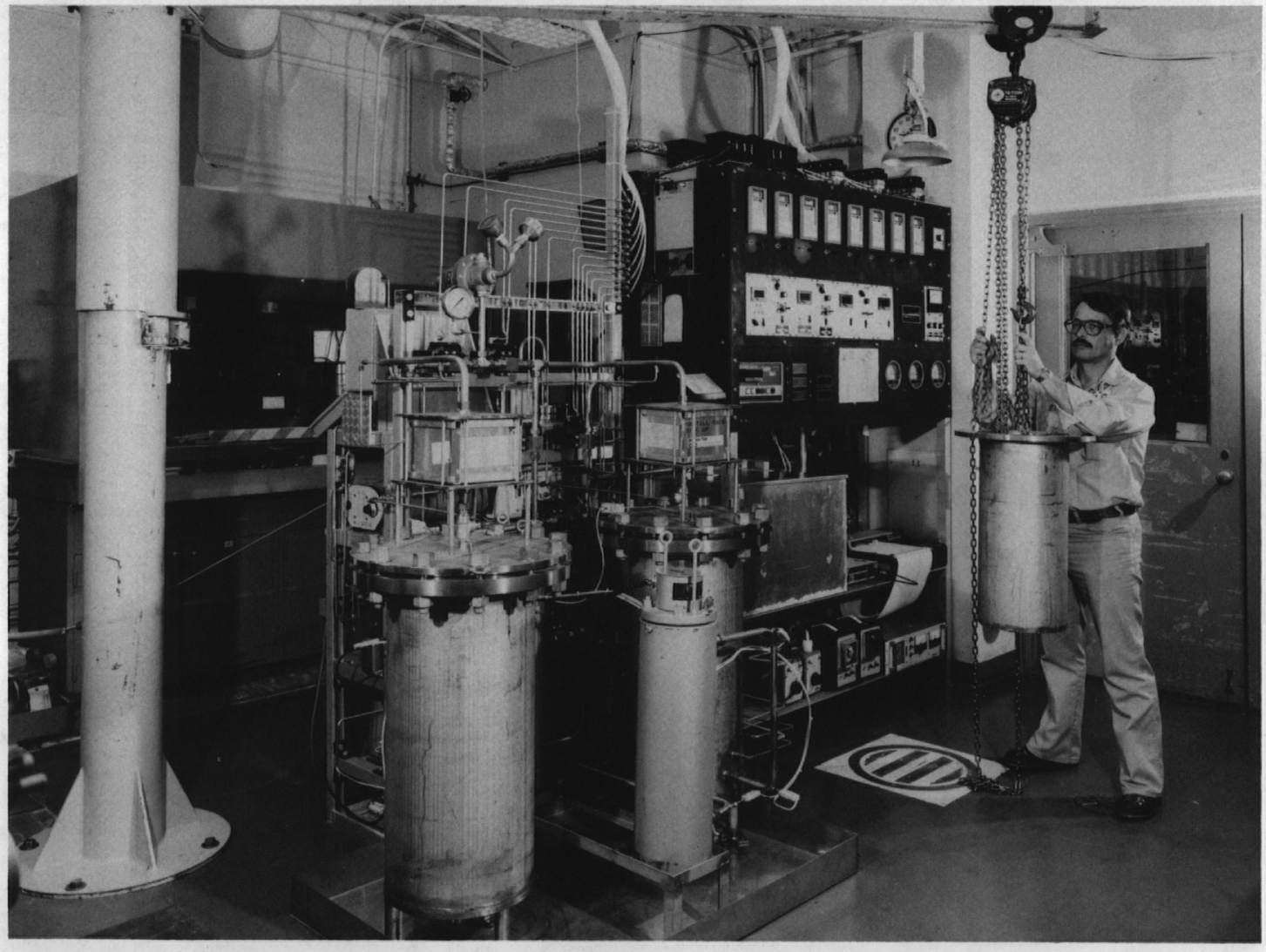

Fig. 11. The ^{14}C-immobilization pilot plant.

breakthrough. This factor and its potential significance will be addressed in a later section. In the subsequent sections, various aspects of the ^{14}C Immobilization pilot unit will be discussed. These sections are intended to describe the process in greater detail, cite potential problem areas, recommend process instrumentation, and provide general design and operating information.

5.1 GAS FLOW STATIONS

Blending of the ^{14}C immobilization pilot unit which consisted of air, steam, and CO_2 feed gas was an important aspect of this study (Fig. 10). Air was obtained from an in-house air supply system (dewpoint <-40°C) and back-up air was provided by a supply system consisting of a Kellogg-American Model 340 air compressor, an after-cooler, and a Kellogg-American Kel-Air Model 35 dryer. Steam was obtained from an in-house, 100 psig, process steam line and CO_2 was obtained from a gas manifold with cylinders. The flow rates of air (0-25 ft^3/min), steam (0-9.99 L/min), and CO_2 (0-500 scm) were monitored with Hastings-Raydist Model FC-2P mass flow meters. For air flow, pressure (100 psig) was reduced via a Masoneilaw pressure regulator, and flow was regulated via a 1.5-in. gate valve. The flow rate was extremely stable although occasional chatter of the pressure regulator occurred. Hastings-Raydist Model FC-2P flow controllers and control valves were used for control of steam and CO_2 flow rates. During the course of the experimental studies, no CO_2 was added to the process stream and hence, the CO_2 flow control system was tested only during process shakedown.

As discussed in a preceeding section, relative humidity is a crucial variable in the operation of this process. During these studies, the relative humidity was controlled by the metered addition of steam to the dry air stream and by control of the gas stream temperature and pressure. A detailed schematic of the steam supply system is given in Fig. 12. Process steam (100 psig) was filtered and condensate was removed via a bucket-type steam trap. Steam pressure was reduced from 100 psig to 20 psig upon passing through a Masoneilaw pressure regulator. The

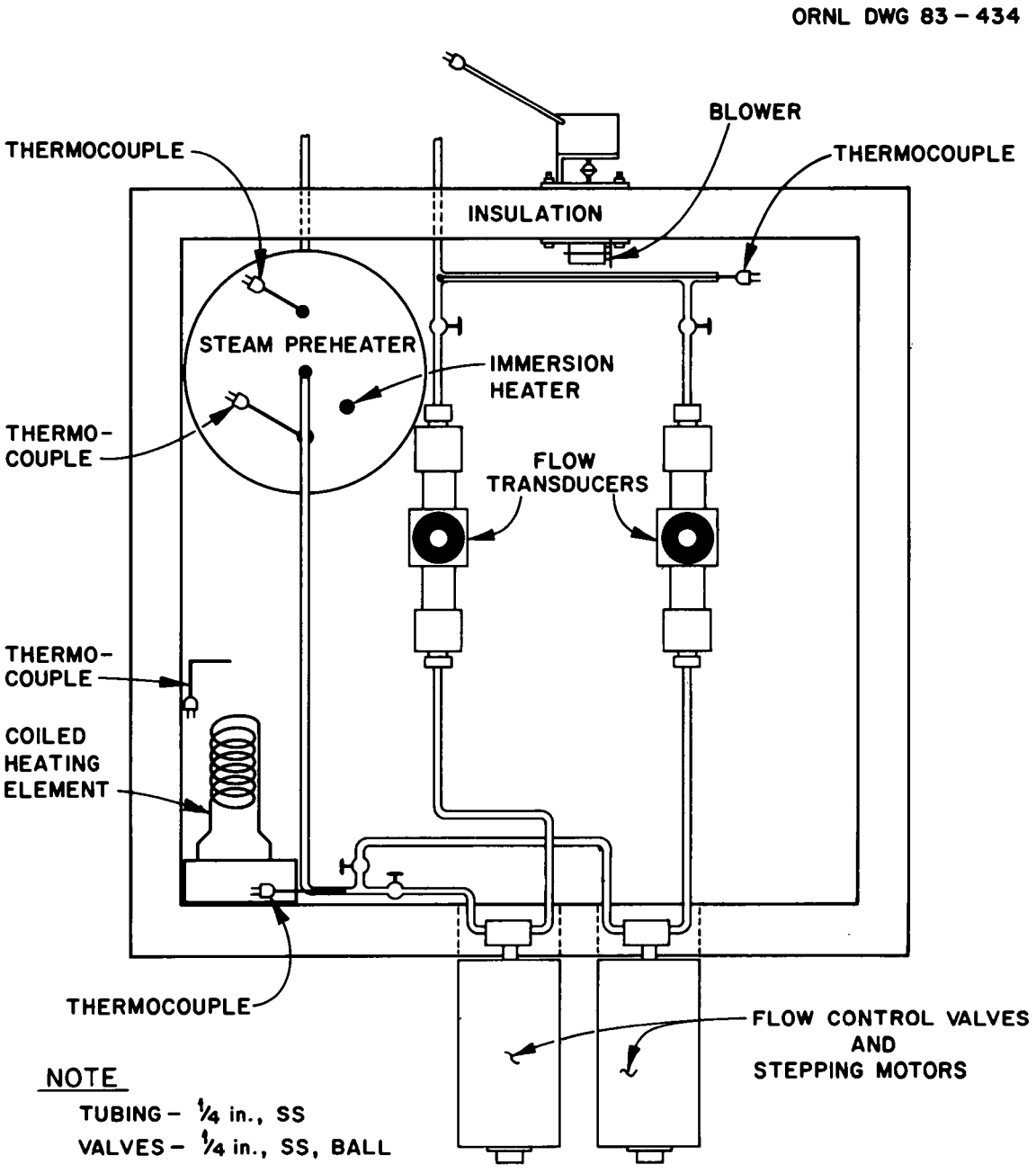

Fig. 12. The steam supply system enclosed within the thermal box.

superheated steam then entered a thermal box (+120°C) and passed through a preheater (130°C), one of two flow control valves, and one of two mass flow transducers. A portion of the steam from the preheater was vented so as to remove or blow out any condensate that might be present in the preheater. The metered steam was then routed to the air supply line where it was injected at the axial centerline. All external steam lines were insulated and several were wrapped and heated with furnace wire. The thermal box was constructed of aluminum and its top could be removed for access to the flow tranducers, valves, etc. The box was insulated with 3.8-cm (1.5 in.) of Fiberfax insulation. The temperatures of the steam preheater and thermal box were controlled by Barber-Coleman model 527Z temperature controllers. For the thermal box, heat was supplied by a Calrod heater and air circulated by a blower coupled to a Eastern Model B-1 motor. Because of the elevated temperature of the thermal box (120°C), this motor and the two stepping motors for the flow control valves were located external to the box as shown in Fig. 12. Temperatures throughout the system were monitored with Type K thermocouples and an Omega Trendicator digital output.

The steam flow controller was electronically coupled to the air flow meter so as to insure a constant steam/air ratio, because of the importance of relative humidity as a process variable. Although fluctuations in air flow were seldom, this procedure insured greater consistancy of the process relative humidity. The calibration curve for the mass flowmeter was only used to provide an approximate valve, because of the difficulties associated with the determination of mass flow near saturation or dewpoint conditions. All water concentrations used in the evaluation of the experimental data were obtained by gas stream analysis via a dewpoint hygrometer (traceable to the National Bureau of Standards). A detailed discussion of the gas analysis instrumentation will be presented in a subsequent section.

Significant problem areas included: (1) gradual degradation of thermocouple wires in the thermal box, (2) occasional thermal-related problems with the steam control valves, and (3) occasional chatter of the pressure reduction regulator for the air stream. Steam flow did fluctuate slightly because of the periodic blow down of the bucket-type steam trap. Therefore, a continuous trap, such as an orifice trap, is recommended for condensate removal. No detailed studies were conducted to determine the long-term stability of the factory calibration of the mass flowmeters. However, the units did operate in an acceptable manner under rather stringent conditions although high temperature cables are recommended. The seals in the flow control valves did suffer thermal degradation, and one valve failed and complete closure of these valves was often difficult.

5.2 PILOT UNIT DESIGN

The principal material of construction for the pilot unit was stainless steel; e.g., stainless steel 0.75-in. tubing was used for bulk gas flow. Flow control (on/off) was possible via pneumatically actuated 0.75-in. Whitey ball valves. The temperature (Fig. 10) of the process stream was controlled by Wellman 3000 Watt, 240 volt electric heaters which were connected to Barber-Coleman Model 527Z temperature controllers. Thermocouples (Type K) that were connected to a Cole-Parmer Model 8388 scanner and Omega Trendicator digital temperature output were located throughout the system. Figure 13 shows that a cannister (either 10- or 12-in.-ID) inside the 14-in.-ID reactor vessel contained the $Ba(OH)_2 \cdot 8H_2O$ flaked reactant. The two reactors used in this study were identical with the exception that the porous stainless steel gas distributor plate was not included in the second reactor. We speculated that plugging of the sintered metal frit or distributor could be a significant problem and that the fixed bed would provide adequate distribution of the gas, and the latter was determined to be the case. The sintered metal distributor resulted in a pressure drop of 1.37 kPa (0.2 psig). Although the reactor vessels are designed to meet the pressure code at 150 psig, the vessels were not coded because of the anticipated experimental conditions, the time involved for coding, and the cost. To abide by pressure code requirements for uncoded vessels, a 11.1 psig rupture disc (Size 3, Type CDC, material 316 TEF, Continental Disc Corporation) was installed in the system.

ORNL DWG 85-755

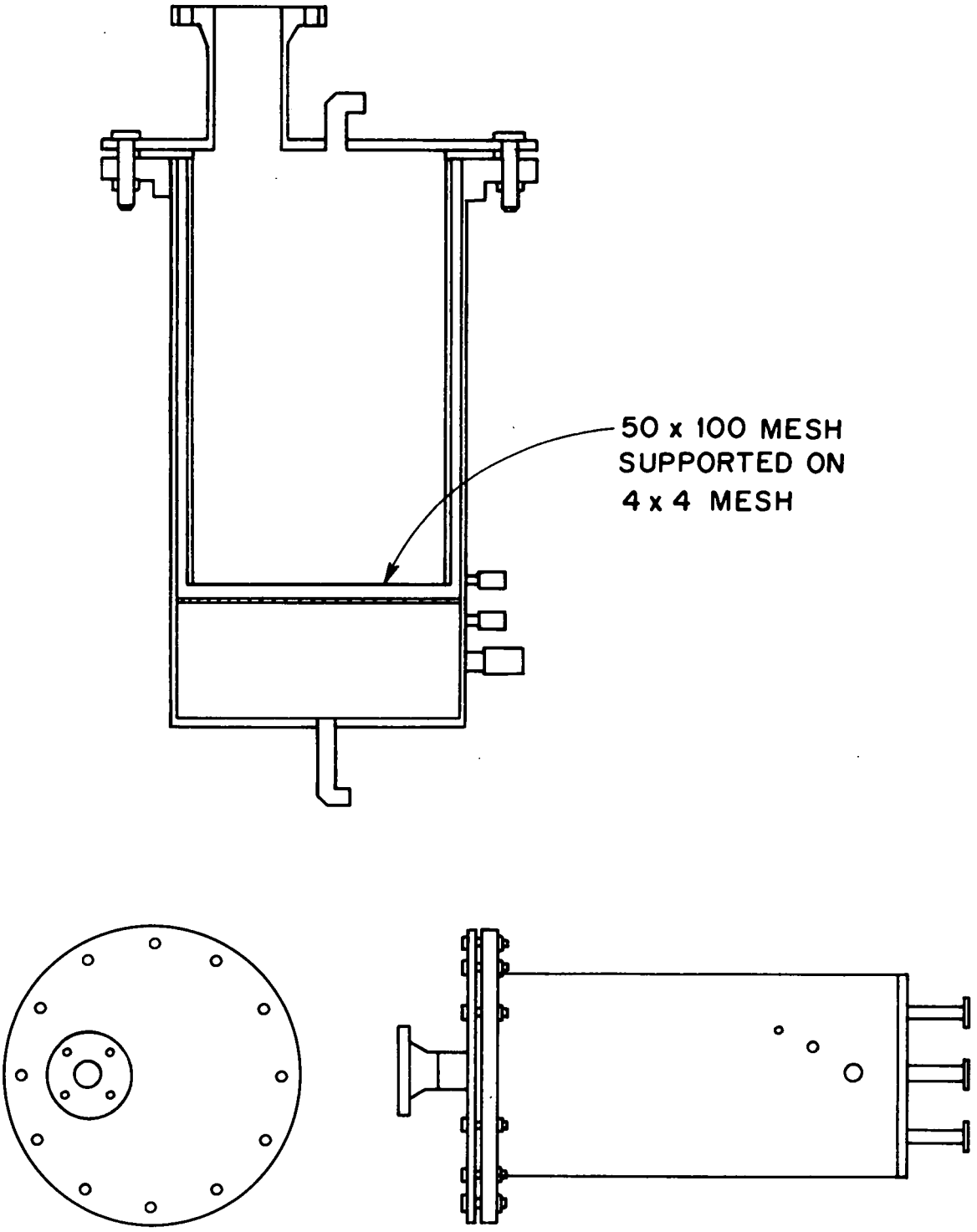

Fig. 13. Schematic of the reactor housing and cannister.

The gas flow through the reactor was upflow. A screen assembly was placed on top of the reactant to minimize bed expansion and particle fluidization. Typically, the bed depth would increase from 43.0 to 48.3 cm (17 to 19 in.) during a run. The pressure drop across the gas disperser was monitored with a Dwyer Photohelix. In the course of these studies, no significant increase in pressure drop across the disperser (an indication of plugging) was observed. Pressure and thermocouple ports at the top and bottom of the reactor enabled the monitoring of absolute and differential pressures and temperatures. The effluent gas passed through a HEPA filter (Model M6-G, Ultra Aire® Filter manufactured by MSA, resistance of 0.90 @ 50 cfm) in the event of significant particle ellutriation from the fixed bed. Dwyer Photohelix differential pressure sensors were used to monitor the pressure drop across the filters and to determine the existence of significant particle loadings on the filters. During the course of these studies, no problems were observed. The effluent gas then flowed either through a second preheater and reactor prior to flowing through a Cash Acme Type FR, 0.75-in. size back pressure regulator or flowed directly to the back pressure regulator. The typical back pressure at the regulator was 109.6 kPa (1.2 psig).

The spent reactant was removed in one of two ways after CO_2 breakthrough and column loading. The canisters (Fig. 11) may be removed from the reactor vessel via a 0.5-ton boom crane manufactured by Contrx Industries, Inc. They can then either be disposed of or the spent reactant transferred to a larger vessel. A second method was also used in these studies in which the product was directly transferred from the canister via a vacuum system.

With respect to suggested design changes, considerable pressure drop resulted from the contraction and expansion of the gas stream upon entering and leaving the various process vessels and from flow through 0.75-in. tubing and fittings at these flow conditions; it is suggested that 1.5- or 2-in. pipe be used on a system of similar size. These studies have indicated that a sintered metal frit is not required to distribute the gas.

A schematic of a prototype unit, capable of processing a 170 m^3/h (100 ft^3/min) air-based gas stream, is shown in Fig. 14. The system consists of: (1) a cartridge or drum housing, (2) a slightly modified 55-gal stainless steel drum containing the reactant/product, (3) a connection cone, (4) a housing cap, and (5) ancillary plumbing hardware. Modifications to the drum consist of: (1) standard drum rims at each end, which are sealable with standard drum lids and contraction bands, and (2) a screen grid at the base of the drum to support the reactant/product. The drums could be loaded with $Ba(OH)_2 \cdot 8H_2O$ reactant flakes either on or off-site. Upon CO_2 breakthrough and loading, the drums containing the $Ba^{14}CO_3$ product would then be sent to a disposal site for either direct storage, or storage as part of a concrete matrix. For gas flow rates >170 m^2/h, it is recommended that units of similar size, situated in parallel, be used.

5.3 GAS ANALYSIS AND PROCESS INSTRUMENTATION

Numerous 0.75- and 0.25-in. Whitey ball valves are located within the system for bulk flow control and for gas sampling (Figs. 10 and 11). For valve actuation, electronic DC signals from a Texas 5TI logic controller are converted to penumatic signals using modular Humphrey TAC electric air valves. The Whitey ball valves were then actuated pneumatically via Whitey actuators. Gas samples may be routinely taken and returned from any one of five points within the system. Sampling from these locations may be controlled by the logic controller. The sample gas is filtered and a portion of it fed to either an EG&G Model 660 or a General Eastern Model 1200 APS hygrometer sensor. These units utilize the "vapor condensation on a mirror" principle, thus providing a true dewpoint determination. The small sensor volume and the resulting small gas throughput (0.5 L/min) enables this portion of the gas sample to be vented to the atmosphere. A Fairchild Model EB-1824 back-pressure regulator is used to maintain constant sensor pressure because of the sensitivity of the dew point to pressure changes. The pressure is determined via a Dwyer Magnahelix and an absolute pressure is determined via knowledge of the

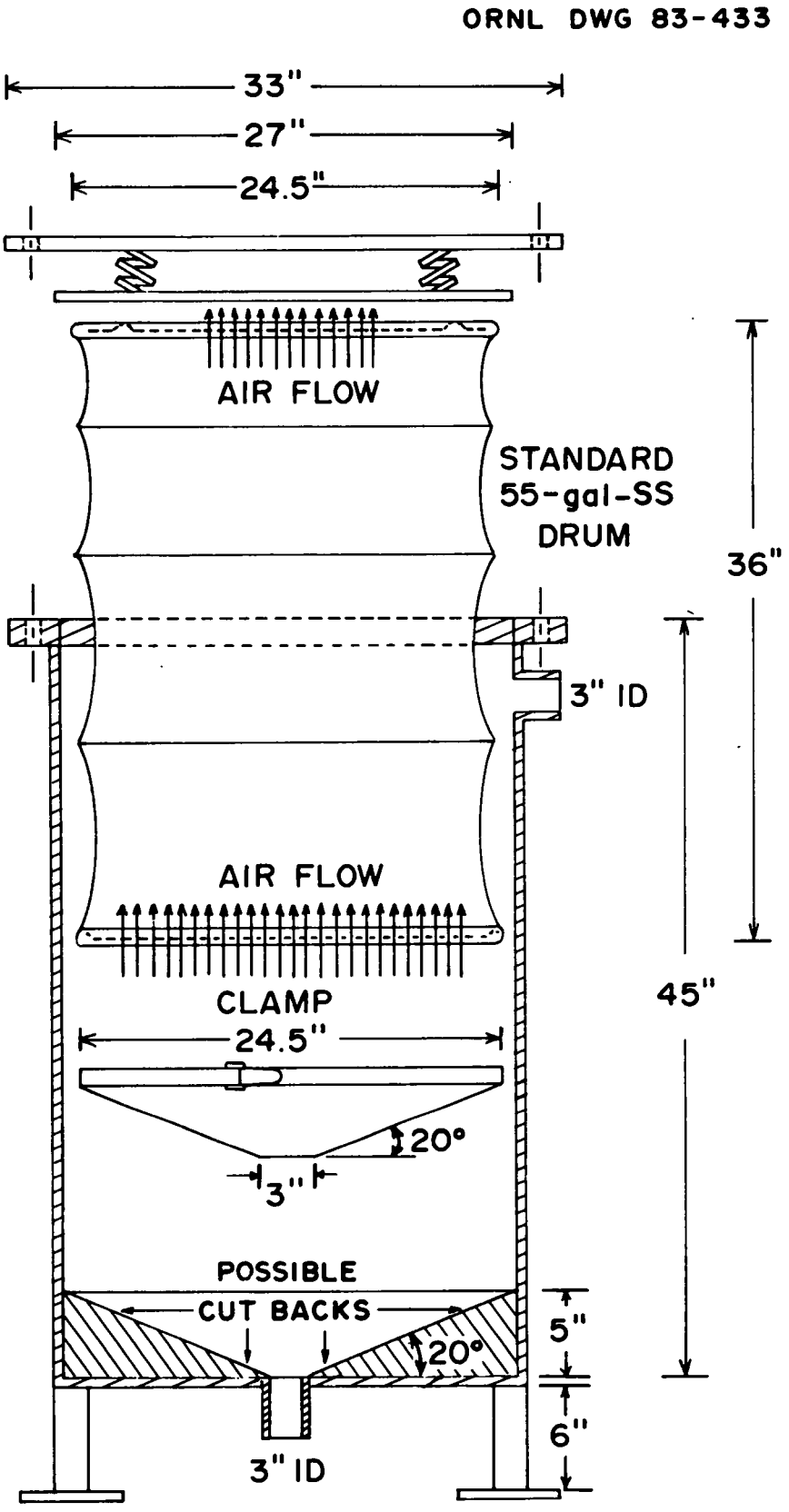

Fig. 14. Schematic of a prototype unit.

barometric pressure. The remainder of the off-gas sample is pressurized via a metal bellows pump, fed to two knockout vessels for H_2O removal, and then sent to a Wilks-Foxboro Miran 1A infrared spectrometer for CO_2 analysis. This latter unit, described elsewhere,[21,32] is capable of analyzing CO_2 over the continuous 100 ppb_v to 330 ppm_v CO_2 range. The throughput is appreciable because of the 5.6-L sensor volume and to ensure an adequate response time. The sample stream is recycled to the pilot unit. The factory-calibrated hygrometers are traceable to the National Bureau of Standards. The calibrations are routinely checked via the recombination of a 2.58% H_2O-0.544% O_2 gas mixture in helium over a Nixox catalyst (Houdry Chemicals) at 200°C; the resulting dewpoint is ∿8.1°C at 14.7 psig. The infrared spectrometer was calibrated and routinely checked with CO_2-bearing gas standards obtained from the Bureau of Mines and commercial vendors. No interference from large variations in water vapor concentration was observed.

As previously cited, gas preheaters controlled by Barber-Coleman Series 527Z temperature controllers were located before each reactor so as to provide the desired influent temperatures. The pressure drop across each column and the gauge pressure at the base of the column were monitored via Foxboro Model E13DH differential pressure cells. Dwyer Photohelix pressure gauges/switches monitor the pressure drop across the gas distributors and HEPA filters. Thermocouples were located throughout the system for temperature control and sensing.

The overall pilot unit may be controlled by a 5TI logic controller manufactured by Texas Instruments. The unit is currently capable of monitoring 8 DC and 16 AC input signals (X prefix) and providing 24 DC and 16 AC output signals (Y prefix). The input/output relay designation is presented in Fig. 15.

The logic controller monitors alarm signals from the CO_2 analyzer, hygrometer, flowmeters, timers, and pressure and temperature sensors. When properly programmed, the unit is capable of sensing an alarm condition such as a CO_2 concentration of 1 ppm_v in the effluent gas stream and actuating valves in the proper sequence, at prescribed time intervals, such that flow is diverted to the second column. Programming for the

Input Assembly No. 1		Output Assembly No. 1		Output Assembly No. 2	
Terminal designation	Terminal name and type	Terminal designation	Terminal name and type	Terminal designation	Terminal name and type
X-0	Manual switch/DC	Y-0			
X-1	Manual switch/DC	Y-1	Relay-air compressor power/DC	Y-24	Air compressor power relay/AC
X-2		Y-2		Y-25	30-h timer relay/AC
X-3	Air flow meter-low alarm/DC	Y-3	Valve 9/DC	Y-26	10-h timer relay/AC
X-4	30-h timer/DC	Y-4	Instrument access air valve/DC	Y-27	
X-5	10-h timer/DC	Y-5		Y-28	
X-6	IR-high alarm/DC	Y-6		Y-29	
X-7	Air flow meter-high alarm/DC	Y-7		Y-29	
X-8		Y-8		Y-30	
X-9	Hygrometer-high alarm/AC	Y-9		Y-31	Temperature controller No. 1 power relay/AC
X-10	Photohelic No. 1-low alarm/AC	Y-10	Valves 2S-2R/DC		
X-11	Photohelic No. 1-high alarm/AC	Y-11	Valves 4S-4R/DC	Y-32	Temperature controller No. 2 power relay/AC
X-12	Photohelic No. 2-low alarm/AC	Y-12	Valves 1S-1R/DC		
X-13	Photohelic No. 2-high alarm/AC	Y-13	Valves 3S-3R/DC	Y-33	Temperature controller No. 3 and 4 power relay/AC
X-14	Photohelic No. 3-low alarm/AC	Y-14	Valves 5S-5R/DC		
X-15	Photohelic No. 3-high alarm/AC	Y-15	Valves 10/DC	Y-34	Temperature controller No. 5 and 6 power relay/AC
X-16	Temperature controller[a] No. 8-high alarm/AC	Y-16	Valve Backup/DC		
		Y-17	Valve 5/DC	Y-35	
X-17	Temperature controller[a] No. 7-high alarm/AC	Y-18	Valve 3/DC	Y-36	
		Y-19	Valve 6/DC	Y-37	
X-18	Temperature controller[a] No. 6-high alarm/AC	Y-20	Valve 2/DC	Y-38	
		Y-21	Valve 8/DC	Y-39	
X-19	Temperature controller preheater No. 5-high alarm/AC	Y-22	Valve 4/DC		
		Y-23	Valve 7/DC		
X-20	Temperature controller heater A, No. 4-high alarm/AC				
X-21	Temperature controller heater B, No. 3-high alarm/AC				
X-22	Temperature controller steam pot No. 2-high alarm/AC				
X-23	Temperature controller thermal box No. 1-high alarm/AC				

[a] Backup temperature controllers.

Fig. 15. 5TI System input/output record.

logic controller was not completed because of time constraints and early program termination. A second area of interest was the use of an Apple Plus II minicomputer for data logging. A Techmar Model AD213 A/D-timer-counter with 14 bit resolution over a 0 to 10 volt range and programmable gains of 1, 10, 100, and 500, and capable of monitoring 26 single-ended inputs was obtained. Applicable software may be found in ref. 39.

With respect to instrumentation recommendations, the Miran 1A and the EG&G Model 660 Dew Point Hygrometer or General Eastern Model 1200APS are highly recommended for CO_2 and H_2O analysis, respectively. A Miran II was tested and, although the instrument possessed excellent sensitivity, we encountered difficulties in obtaining the desired resolution over the available output span. For the concentration range of interest, $\sim$3 orders of magnitude change in the output signal are required. The Humphrey TAC3 electric air valves and the Whitey actuators and ball valves are highly recommended. However, a spring return on the actuators, rather than air-actuation in both directions, would be preferred so as to reduce the number of air supply lines by a factor of 2. The Foxboro Model E13DH differential pressure sensors provided excellent resolution and stability. With respect to the logic control and data logging systems, it is recommended that the two functions be combined. The 5TI logic controller is no longer state-of-the-art. One would likely desire a combined control/data logging system, which could be integrated into the overall process control system for the plant.

6. EXPERIMENTAL PILOT UNIT STUDIES

A total of eight experimental runs were conducted with the ^{14}C Immobilization pilot unit with a typical run lasting $\sim$260 h. Therefore, the total operating time on the pilot unit was $\sim$2100 h or $\sim$88 d. Data from these experimental runs are given in Figs. 16-23. The influent gas stream temperature was $\sim$27°C and the influent CO_2 concentration (C_o) was assumed to be the nominal air concentration (330 ppm_v). Relative humidity

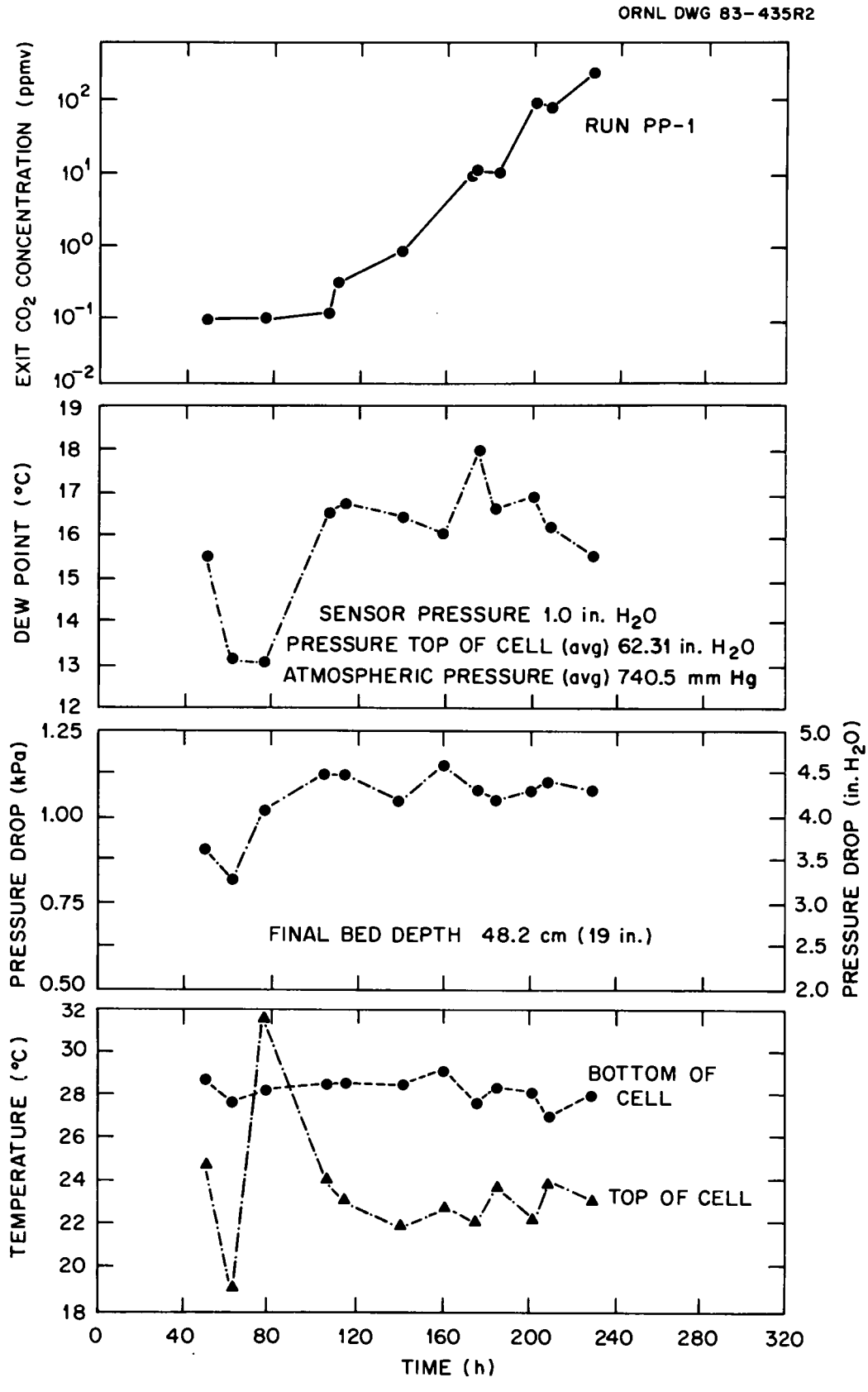

Fig. 16. Run PP-1 data.

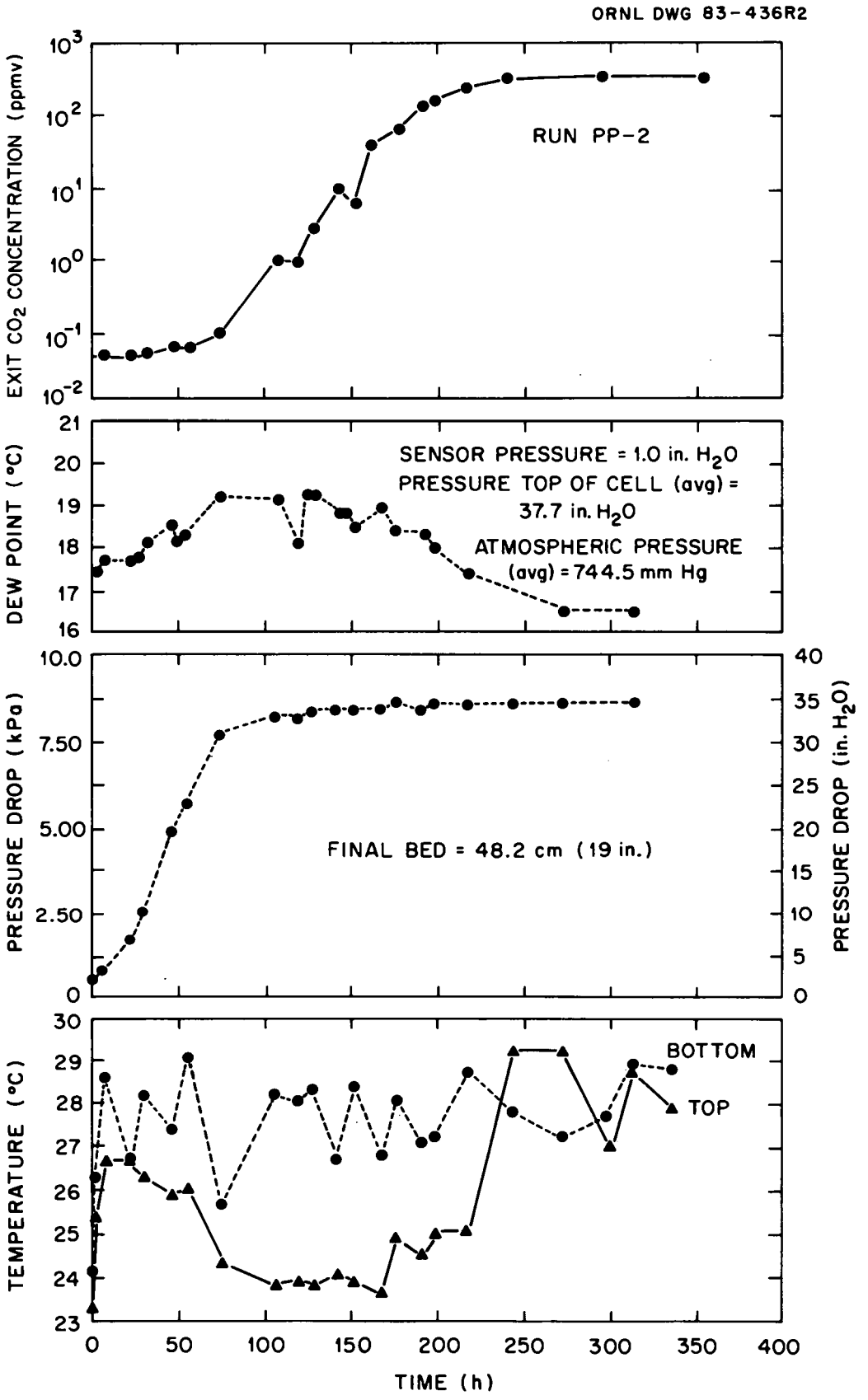

Fig. 17. Run PP-2 data.

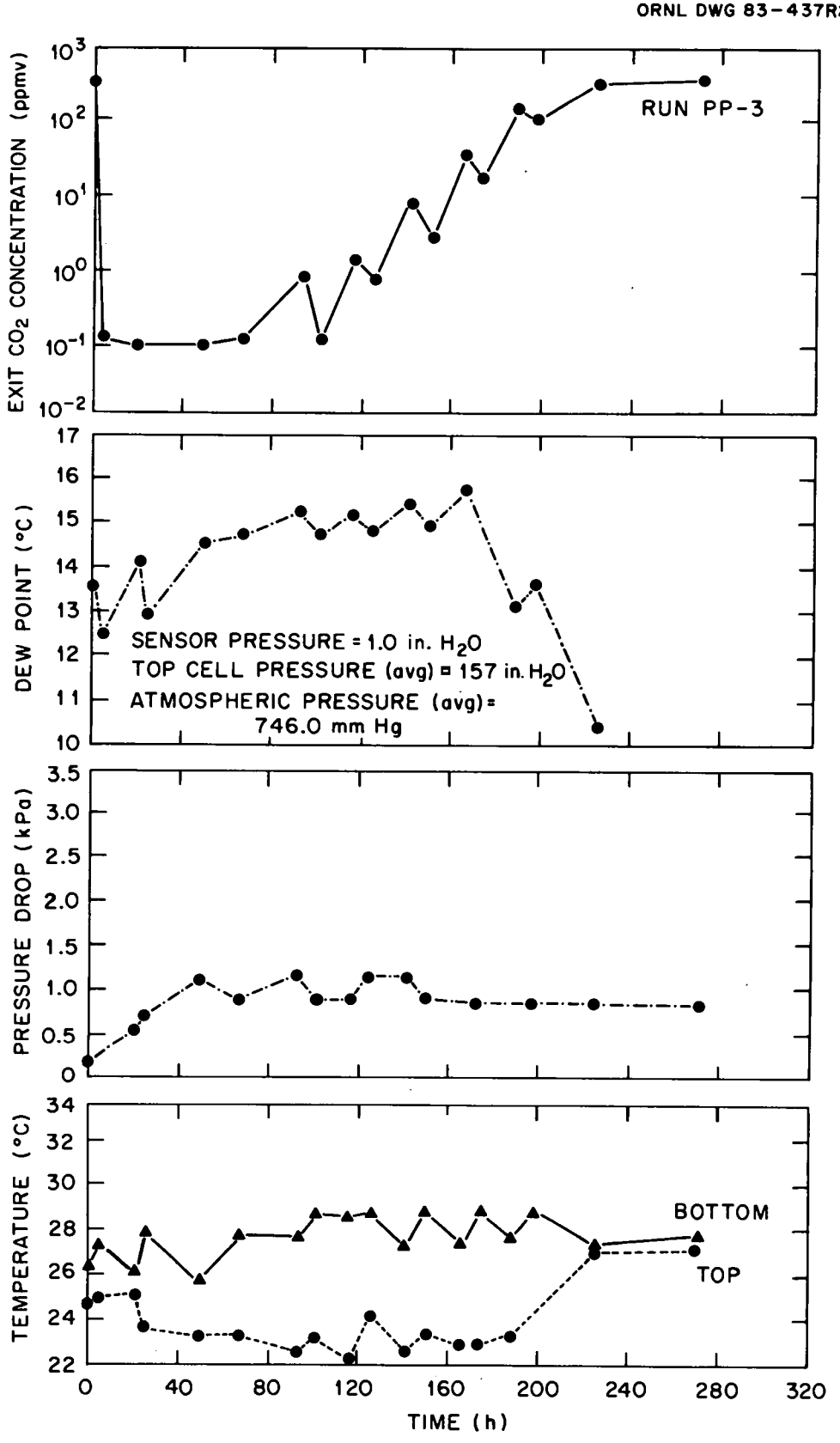

Fig. 18. Run PP-3 data.

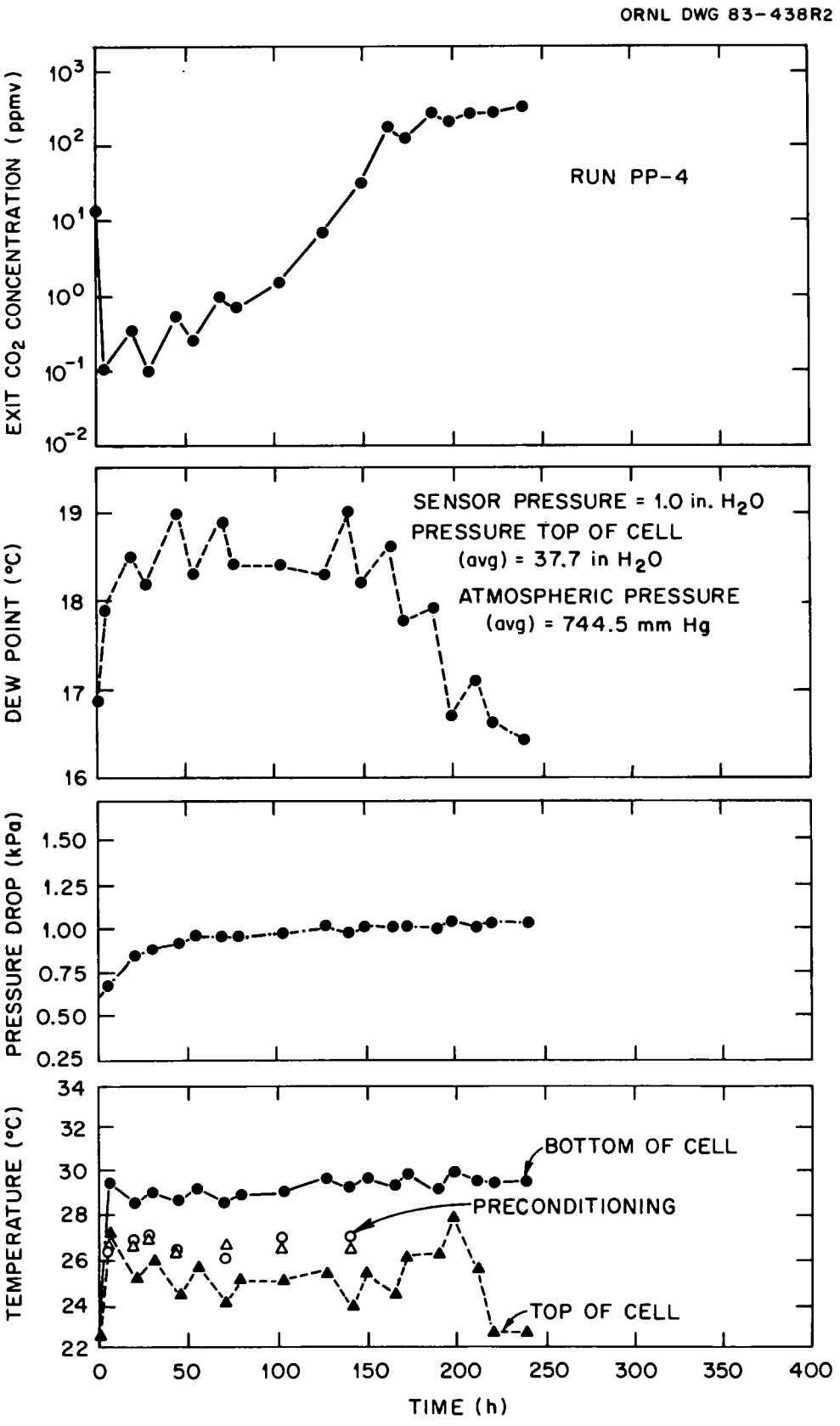

Fig. 19. Run PP-4 data.

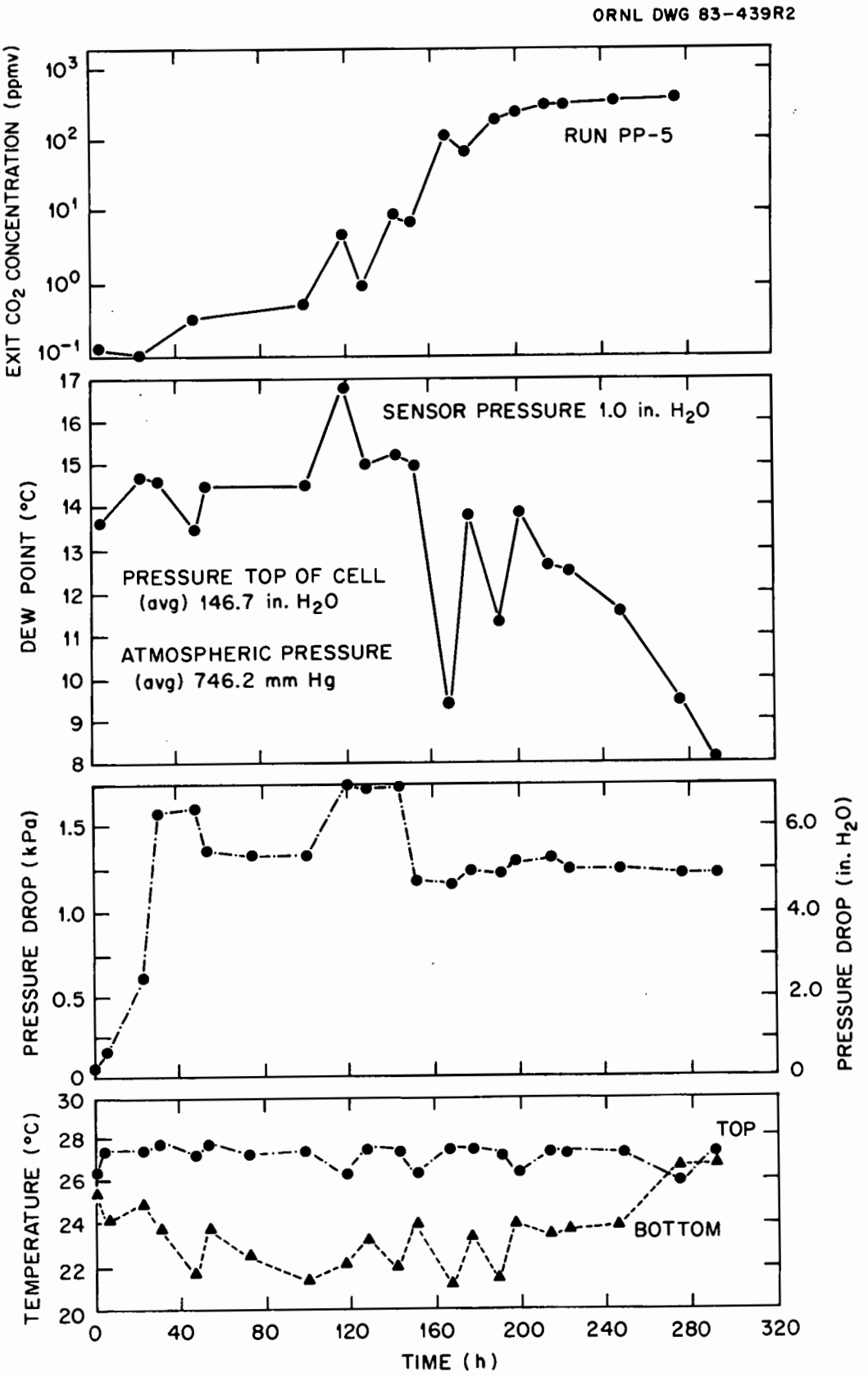

Fig. 20. Run PP-5 data.

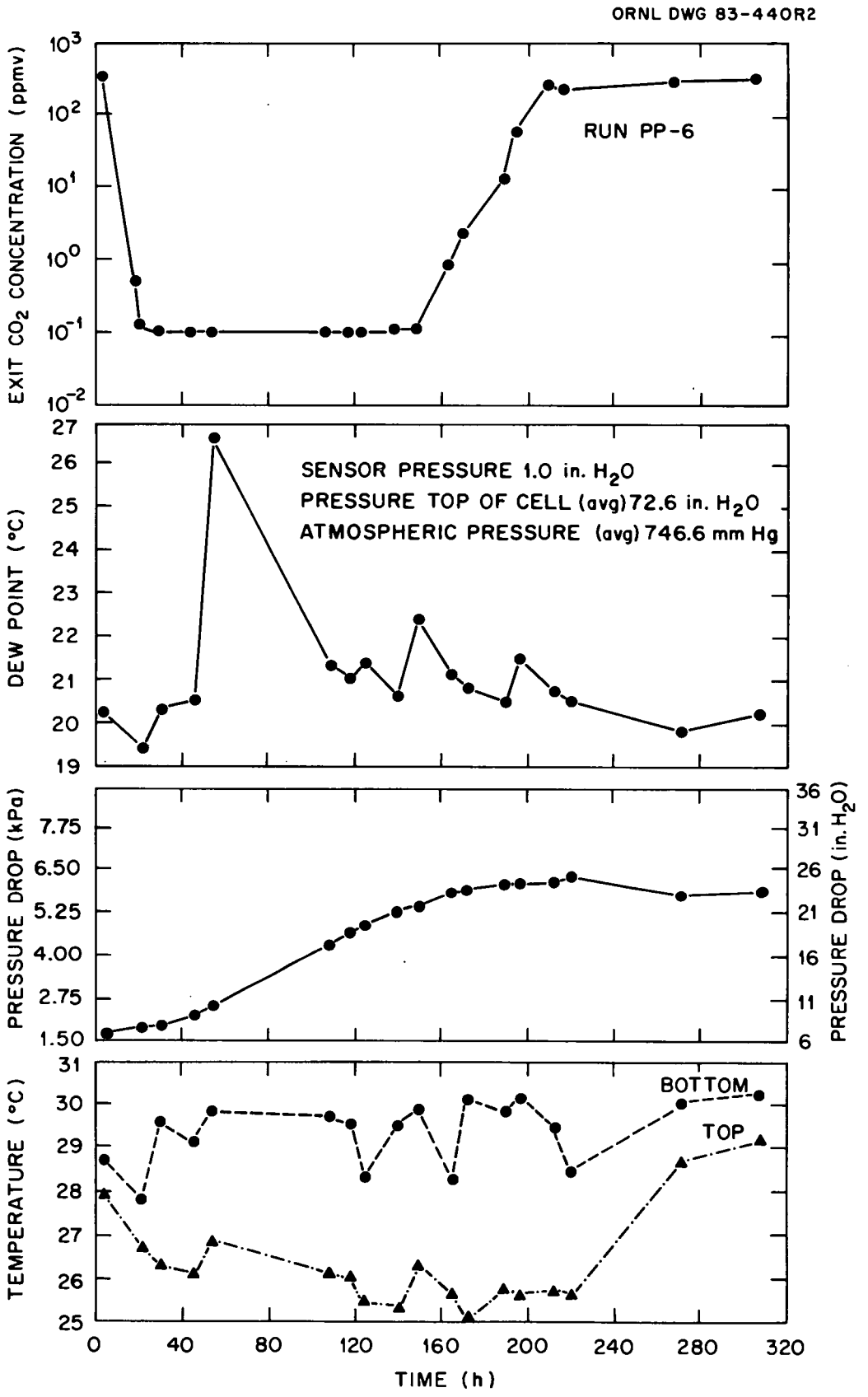

Fig. 21. Run PP-6 data.

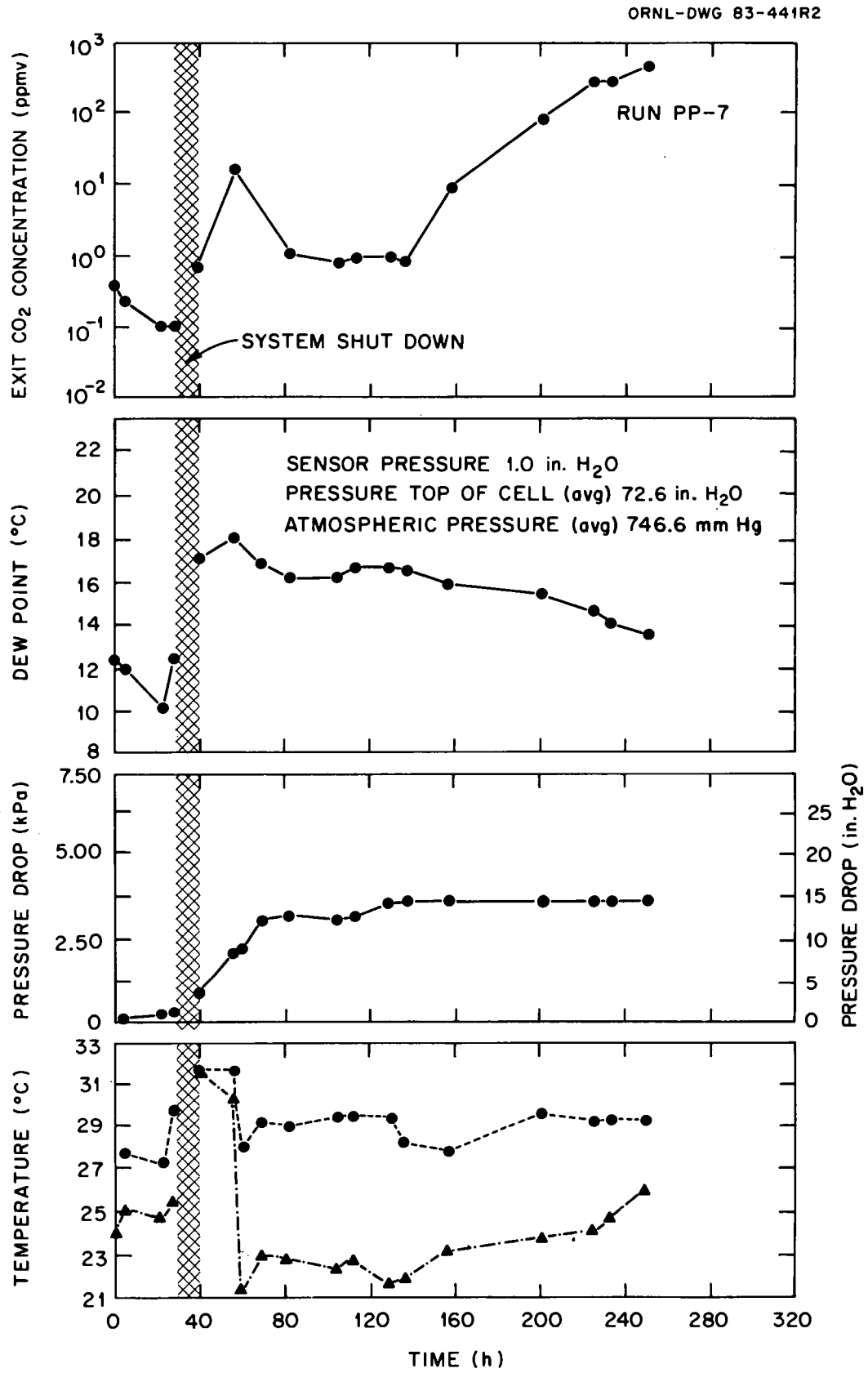

Fig. 22. Run PP-7 data.

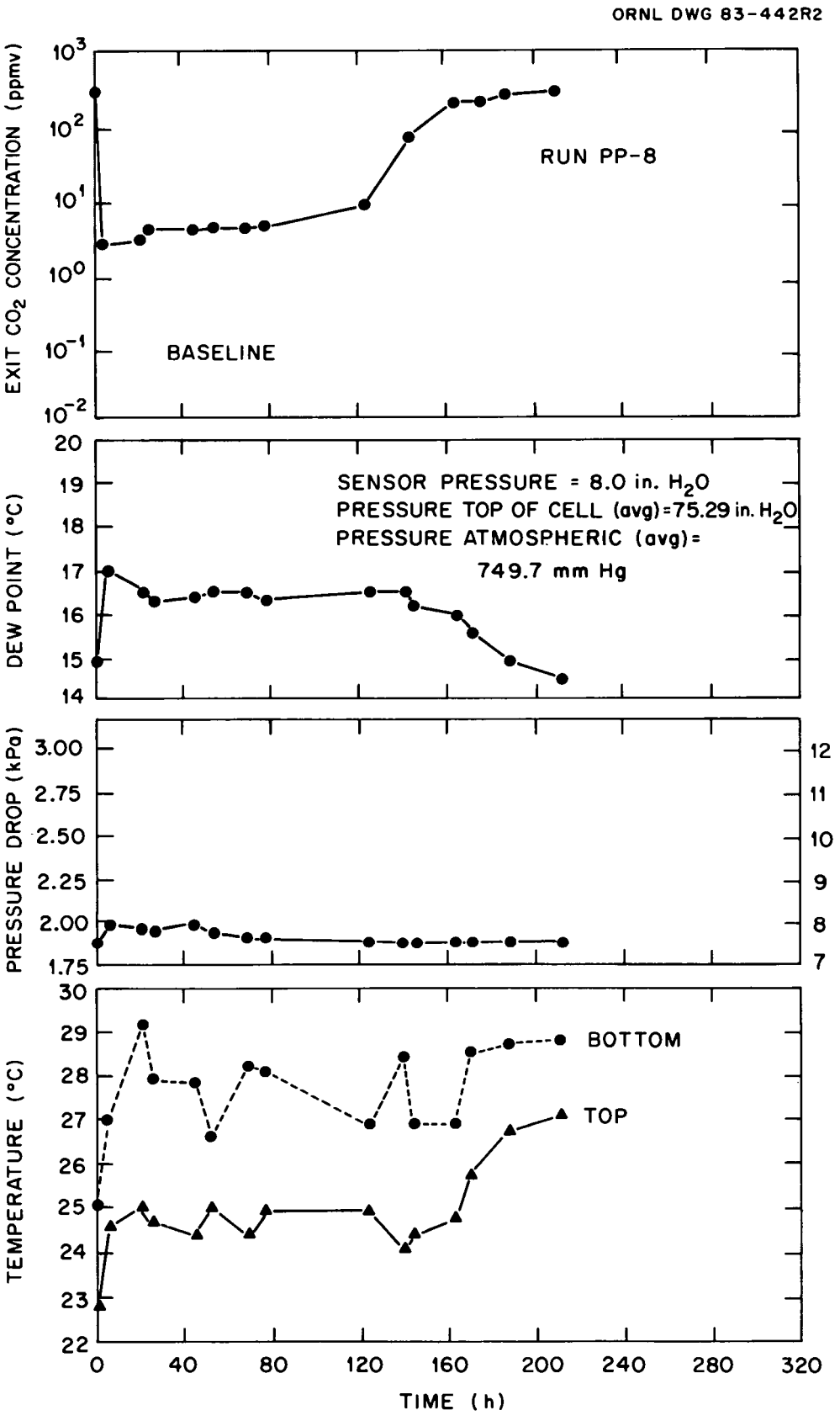

Fig. 23. Run PP-8 data.

of the influent gas stream was the variable of interest. In Figs. 16-23, the sensor pressure and the pressure at the top of the cell are differential pressures; the reference or base pressure is atmospheric pressure. Therefore, the time sensor pressure is the sensor pressure plus atmospheric pressure. With the exception of Run PP-8, the superficial gas velocity was 12.9 cm/s at reference conditions.[a] For Run PP-8, the superficial gas velocity at reference conditions was 18.6 cm/s. Again with the exception of PP-8, each 30.5-cm-diam (12-in.-diam) canister contained 31.8 kg (70 lb) of reactant. The canister diameter for PP-8 was 25.4 cm (10 in.) and it contained 22.1 kg (48.7 lb) of reactant. The initial bed depth was 44.5 cm (17.5 in.) and it was observed to increase by $\sim$3.81 cm (1.5 in.) due to bed expansion during a typical run. A 100-mesh wire screen was placed over the bed to prevent particle entrainment. However, no increase in pressure drop across a downstream HEPA filter was observed, thus indicating little if any entrainment of fines.

In each of the runs given in Figs. 16-23, there was a period of excellent CO_2 removal which was followed by CO_2 breakthrough. The effluent dewpoint was observed to initially increase with time and then to fall to the influent dewpoint. The gradual increase in dewpoint resulted from water being produced by the CO_2-$Ba(OH)_2 \cdot 8H_2O$ reaction and a portion of that water being sorbed to hydrate the bed to $Ba(OH)_2 \cdot 8H_2O$. The gradual increase in CO_2 concentration resulted from the decrease in the overall carbonation reaction as complete column loading was approached. In those cases where the increase in pressure drop is appreciable (PP2, PP6), the pressure drop increase continued as a function of bed conversion. In those cases where it is not appreciable (PP3, PP4, PP5), the bulk of the increase in the pressure drop occurs during the initial stages of the run. With respect to influent and effluent temperatures, the temperatures gradually diverge as the effluent gas temperature decreased due to the endothermic reaction and then converged with CO_2 breakthrough.

---

[a]Reference temperature and pressure defined as 21.1°C (70°F) and 101.3 kPa (1 atm).

The primary intent of runs PP-1, PP-2, PP-3, PP-5, and PP-7 was to determine the effect of relative humidity upon the operating properties of the system. The CO_2-free effluent gases from runs PP-3, PP-5, and PP-7 were used to hydrate the commercial $Ba(OH)_2 \cdot 8H_2O(7.47H_2O)$ flakes to $Ba(OH)_2 \cdot 8H_2O$ for runs PP-4, PP-6, and PP-8, prior to contact with CO_2-bearing streams. These studies were conducted to determine if prior hydration of the bed at an appropriate relative humidity would enable subsequent CO_2 sorption at much higher relative humidities, in the absence of significant pressure drop problems.

Since the intent of the pilot unit studies was to provide developmental, operational, and experimental information, the quality of the experimental data was often not as good as one would desire, because of problems associated with the initial shakedown of the process and various unscheduled upsets during process operation. The early termination of the program also had a detrimental effect on the quality of the experimental data. Ideally, one would desire a much broader data base. Various characteristics of the process will now be addressed.

6.1 PROCESS THERMODYNAMICS

Whereas prior studies on the 10.2-cm-ID reactors were conducted under near-isothermal conditions (the reactor was jacketed), studies conducted with the pilot unit were performed under near-adiabatic conditions. Upon start-up of a run, three thermal-related phenomena occurred within the bed.

1. Upon process start-up, the inlet gas temperature of 27°C caused an increase in the temperature of the bed from its initial temperature of 22°C.
2. The commercial $Ba(OH)_2 \cdot 8H_2O(7.47H_2O)$ flakes hydrated (an exothermic reaction) to $Ba(OH)_2 \cdot 8H_2O$. The enthalpy change for the hydration step is -58.2 kJ/mol-H_2O.[21,22]
3. The reaction of CO_2 with $Ba(OH)_2 \cdot 8H_2O$ and the subsequent release of 9 water molecules as vapor is endothermic. The enthalpy change is +36.4 kJ/mol-CO_2.[21,22]

The magnitude of the effect of each of the preceding thermal effects will now be discussed.

6.1.1 Thermodynamics — Process Startup

The temperature of the influent and effluent streams rose quickly from 22°C to ~27°C upon process startup as shown by the preconditioning of PP-4 (that is the contacting of the bed with a CO_2-free gas). Experimental studies to be detailed in a subsequent section indicated that for the preconditioning conditions of PP-4, the thermal contribution from the hydration step was not large. Since the gas stream contained little CO_2, thermal effects from the carbonation reaction would be negligible. Confirmation of these experimental observations and the preceding analysis is possible via the following argument.

Assuming negligible resistance to heat transfer within the flake (i.e., a uniform flake temperature) and negligible heat conduction between flakes, the following energy balances and boundary conditions may be developed:

Gas Phase:

$$\rho_G C_P \frac{\delta T_G}{\delta t} = GC_P \frac{\delta T_G}{\delta z} = hA (T_G - T_s) \qquad (1)$$

Boundary conditions: $T_G=22°C \quad t=0 \quad z>0$
$T_G=27°C \quad t\geq 0 \quad z=0$

Solid Phase:

$$\rho_s C_s \frac{\delta T_s}{\delta t} = hA (T_G - T_s) \qquad (2)$$

Boundary conditions: $T_s=22°C \quad t=0 \quad z>0$

where

ρ_G = gas density ($1.17 \cdot 10^{-3}$ g/cm^3),

C_p = gas specific heat (1.01 J/g·K),

T_G = gas temperature (K),

t = time (s),

G = ($1.75 \cdot 10^{-2}$ g/cm^2·s) mass flow rate/cross sectional area,

z = axial length (cm),

h = heat transfer coefficient (J/cm^2·K·s),

A = specific area (cm^2/cm^3),

T_s = solid temperature (K),

ρ_s = bulk solid density (0.98 g/cm^3), and

C_s = solid specific heat (~2.30 J/g·K).

Although correlations exist for predicting heat transfer coefficients for irregular shaped packings, the following approach was used because of difficulties in: (1) the determination of A, the area available for heat or mass transfer, and (2) the availability of mass transfer data for the system of interest. Prior modeling studies on the 10.2-cm-ID reactor had indicated mass transfer across the gas film to be the controlling resistance. For this system, the controlling partial differential equations for the gas and solid phases were solved numerically. Comparison of the model-predicted breakthrough curves with actual data enabled an appropriate rate expression to be developed, which was of the form:

$$R = K_F A_O (1 - X) C \qquad (3)$$

where

K_F = gas film mass transfer coefficient (cm/s),

A_O = initial surface area available for mass transfer (cm^2/cm^3),

X = reactant conversion, and

C = reactant concentration (g/cm^3).

The 1-X term compensates for the fact that the area available for reaction will decrease with conversion because of the nonuniform thickness of the flakes. Values of the modified mass transfer, $K_F A_O$, were determined from the breakthrough curves. Using a representative value of A_O for our

system (A_o=10.8 cm^2/cm^3), the experimental K_F value (0.7 cm/s) was found to be representative of literature values.

Based upon the analogy between heat and mass transfer as proposed by Chilton and Colburn, one may use the j-factor equations in the following manner:[40,41]

$$j_H = j_M \tag{4}$$

$$j_H = \frac{h}{C_p G}\left[\frac{\mu}{\rho_G D}\right]^{2/3} \tag{5}$$

$$j_M = \frac{K_F \rho_G}{G}\left[\frac{\mu}{\rho_G D}\right]^{2/3} \tag{6}$$

where

j_H = j factor for heat transfer,

j_M = j factor for mass transfer,

G = mass flow rate/cross sectional area [$g/(cm^2 \cdot s)$],

μ = viscosity [1.88 $g/(cm \cdot s)$], and

D = diffusivity (0.163 cm^2/s).

Rearranging Eqs. (5) and (6), we get:

$$\frac{h}{C_p G} = \frac{K_F \rho_G}{G} \tag{7}$$

Multiplying both sides by A_o, the initial area available for heat or mass transfer, the desired equation for predicting the modified heat transfer coefficients, hA_o, from the modified mass transfer coefficients, $K_F A_o$, is obtained:

$$hA_o = C_p \rho_G K_F A_o \tag{8}$$

$$= 8.93 \cdot 10^{-3} \text{ J/cm}^3 \cdot \text{K} \cdot \text{s}$$

With this information, an exact solution to the controlling partial differential equations may be obtained by using the technique of Schumann.[42] From an experimental perspective, Furnas demonstrated Schumann's solution to be applicable to a system similar to that of present interest.[43] However, the solution is rather cumbersome and requires use of the Bessel function. For the purpose of this analysis, such a rigorous approach is not required. On a per unit bed volume, the heat capacity or content of the gas phase as compared to the solid phase differs by ~3 orders of magnitude. Therefore, a change of 5 K in the gas phase will have a negligible effect on the energy balance and the term in Eq. (1):

$$\rho_G C_p \frac{\delta T_G}{\delta t} = 1.18 \cdot 10^{-3} \frac{\delta T_G}{\delta t} \tag{9}$$

will be dropped from the gas phase energy balance. Solutions to the resulting differential equations for the appropriate boundary conditions may be obtained, again via the method of Schumann.[42] However, as before, such solutions will not be required since we are only interested in an order of magnitude analysis. Rearranging the gas and solid phase energy balances (Eq. 1 and 2) we get:

$$\frac{\delta T_G}{\delta z} = \frac{hA_o(T_G - T_s)}{GC\rho} = 0.505 \ (T_G - T_s), \text{ K/cm} \tag{10}$$

$$\frac{\delta T_s}{\delta t} = \frac{hA_o(T_G - T_s)}{\rho_s C_s} = 3.96 \cdot 10^{-3} \ (T_G - T_s), \text{ K/s} \tag{11}$$

$$= 14.2 \ (T_G - T_s), \text{ K/h}$$

or

$$\frac{\delta T_G}{\delta z} = 28.1 \frac{\delta T_s}{\delta t}, \text{ units of K, cm, h.} \quad (12)$$

From the preceding equations, it appears that the gas phase temperature gradient will be sharp and the solid phase temperature will rise rapidly, as compared to the total run time of ~260 h. To raise the temperature of the bed from 22 to 27°C, the net energy requirement is 368 kJ.

6.1.2 Thermodynamics — The Carbonation Reaction

Thermodynamic analysis of the CO_2-$Ba(OH)_2 \cdot 8H_2O$ gas-solid reaction has indicated the reaction to be endothermic (ΔH_R = 364.4 kJ/mol-CO_2), when the water product is released as vapor. However, if the gas stream should be saturated in water vapor, the water product must exist as a liquid and the reaction becomes exothermic (ΔH_R = -3.17 kJ/mol-CO_2). Assuming: (1) the reactant is fully hydrated, (2) the CO_2 sorption occurs under near-adiabatic conditions, (3) the effluent CO_2 concentration is zero, (4) the water product is released as vapor, and (5) the process is pseudo-steady-state ($dT_G/\delta t$, $\delta X_{CO_2}/\delta t$=0); the temperature drop of the gas stream may be calculated via a gas phase energy and mass balance.

Energy Balance of Gas Phase:

$$GC_p \frac{dT_G}{dz} = R_{CO_2} \Delta H_R \quad (13)$$

CO_2 Mass Balance of Gas Phase:

$$\frac{G}{MW} \frac{\left(dX_{CO_2}\right)}{dz} = R_{CO_2} \quad (14)$$

where

G = mass flow rate/cross sectional area [g/(cm^2·s)],

R_{CO_2} = molar rate of reaction (mol-CO^2/cm^3·s),

MW = molecular weight of air (28.95), and

X_{CO_2} = mol or volume fraction of CO_2.

The influent CO_2 mol fraction is that of air (0.00033) and the effluent will be 0.0 because of complete CO_2 removal ($\Delta X_{CO_2} = X_{CO_2}$). It will be assumed that G, Cp, R_{CO_2}, and ΔH_R are weak functions of temperature and that G will remain constant because of the dilute CO_2 concentrations. Rearranging and combining Eqs. (13) and (14), one would predict a temperature drop in the gas stream of:

$$\Delta T_G = \frac{\Delta H_R X_{CO_2}}{C_p\ (MW)} = \frac{(364,400)(0.00033)}{(1.01)(28.95)} = 4.11\ K \qquad (15)$$

6.1.3 Thermodynamics — The Hydration Reaction

The reactant used in these studies was commercial $Ba(OH)_2 \cdot 8H_2O$ flakes which possessed a water stoichiometry of 7.47 H_2O. A description of the reactant characteristics was presented in Sect. 2. Since experimental studies indicated $Ba(OH)_2 \cdot 8H_2O$ to be the desirable species for CO_2 sorption [3 orders of magnitude greater reactivity than either $Ba(OH)_2 \cdot 3H_2O$ or $Ba(OH)_2 \cdot H_2O$] and the pilot unit was operated under conditions which favored the formation of $Ba(OH)_2 \cdot 8H_2O$, one would expect to observe a temperature effect from the exothermicity of the hydration step [ΔH_H = -58.2 kJ/(mol-H_2O)]. The magnitude of this hydration effect upon the effluent gas stream temperature would then be dependant upon the rate of hydration and CO_2 sorption. The pseudo-steady-state, gas-phase energy balance is of the form:

$$GC_p\left(\frac{dT_G}{dz}\right) = R_H\ \Delta H_H - \left[(R_{CO_2})(\Delta H_R)\right] \qquad (16)$$

where R_H is the molar rate of hydration [mol/(cm^3·s)] and ΔH_H is the heat of hydration (J/mol). The total enthalpy change for the hydration of an entire canister of reactant (32 kg) is

$$\Delta H = \Delta H_H \frac{M}{MW_R} (8.0 - S) \tag{17}$$

where

M = initial reactant mass (32 kg),

MW_R = molecular weight of reactant (= 305.5 for $Ba(OH)_2 \cdot 7.47\ H_2O$), and

S = hydration stoichiometry of the reactant (7.47 H_2O); or

$$\Delta H = \frac{(-58.2)(32{,}000)}{(305.5)} (8.0 - 7.47) = -3{,}231 \text{ kJ} \tag{18}$$

Using the preceding equations derived from a gas phase energy balance (Eq. 16) and assuming a given rate of hydration, the resulting temperature change of the effluent gas may be calculated (Eq. 15). The results of this analysis with and without an accompanying carbonation reaction with 330 ppm_v CO_2 and assuming an initial bed temperature of 295 K is presented in Table 2.

The question as to whether the rate of hydration is controlled by mass transfer across the gas film or by chemical reaction kinetics requires further analysis. Prior studies for this system have indicated that transfer of CO_2 across the gas film is the controlling resistance in the overall carbonation reaction. Employing an analogy between the mass transfer of CO_2 and H_2O, the rate equation for hydration would be of the form:

Table 2. Effluent gas stream temperature as a function of hypothetical time for the complete hydration of $Ba(OH)_2 \cdot 7.47H_2O$[a]

Time (h)	Temperature change (K)	
	Hydration alone	Hydration with CO_2 reaction ($330\ ppm_v\ CO_2$)
0.1	36.83	36.6
1.0	24.95	23.5
5.0	10.24	7.2
10.0	5.90	2.411
16.9	3.72	0.0
100.0	0.68	3.35
∞	0.00	4.11

[a]Initial bed assumed to be 295 K.

$$R = K_F A_o (1-X)\left[X_{H_2O} - X_{H_2O\ (E)}\right] C_B \qquad (19)$$

where

$K_F A_o$ = modified mass transfer coefficient ($\sim 8 s^{-1}$ for the system of interest),

X = solid conversion,

$X_{H_2O} = P_{H_2O}/P_s$, mol or volume fraction of H_2O vapor,

P_{H_2O} = water vapor pressure,

P_s = system pressure,

$X_{H_2O(E)} = P_{H_2O(E)}/P_s$, equilibrium mol or volume fraction of H_2O vapor,

$P_{H_2O(E)}$ = water vapor pressure in equilibrium with $Ba(OH)_2 \cdot 8H_2O$, and

C_B = bulk gas water vapor concentration, mol H_2O/L.

When considering the experimental data presented in Figs. 16 to 23, it is interesting to note that in no case did the water vapor pressure in the

effluent gas decrease sufficiently so as to approach the equilibrium vapor pressure of 1.29 kPa (9.6 mm Hg) (or the corresponding dewpoint of ~10.7°C at 1 atm) of $Ba(OH)_2 \cdot 8H_2O$. Therefore, assuming a representative difference in the bed between water vapor pressure in the bulk gas and the equilibrium vapor pressure of $Ba(OH)_2 \cdot 8H_2O$ to be 533 Pa (4 mm Hg) and assuming negligible reactant conversion (X~0), the following rate expression may be obtained:

$$R = 0.0017 \text{ mol } H_2O/(L \cdot s).$$

The time required for the complete hydration of a typical canister, assuming mass transfer control, would be 0.27 h. Therefore, based upon the data presented in Table 2, an increase in effluent gas temperature of ~34 K would be predicted. Such an increase was not observed as indicated in Figs. 16 to 23.

Upon first analysis, this observation would appear to be in conflict with prior studies on the hydration of $Ba(OH)_2 \cdot 3H_2O$ to $Ba(OH)_2 \cdot 8H_2O$. Those studies were conducted using a microbalance and elaborate pressure control instrumentation and are reported elsewhere.[22] The hydration reaction was examined in the absence of a diluent gas (only water vapor). Indications were that both the dehydration of commercial $Ba(OH)_2 \cdot 8H_2O$ flakes to $Ba(OH)_2 \cdot 3H_2O$ and the subsequent rehydration could be modeled via a shrinking core-type model based upon planar geometry. The studies were conducted at two temperatures and the rate of hydration was observed to be proportional to relative humidity. Data analysis showed that the rate was dependent upon the difference between the water present on the particle surface for a given relative humidity, and that required for $Ba(OH)_2 \cdot 8H_2O$ to be stable. In the regime studied (relative humidities of 30 to 60%) the number of layers of surface water increases nearly linearly with relative humidity. An in-depth review of this analysis is presented elsewhere.[32] As previously stated, the studies, conducted on 150 mg samples, indicated the rate of hydration or dehydration to be dependant upon the system relative humidity and the $Ba(OH)_2 \cdot 8H_2O$ vapor pressure.

Assuming a similar rate of rehydration for the canister beds of interest and assuming a negligible resistance to mass transfer through the gas film, one would predict the time required for bed hydration to range from 0.17 to 6.4 h. Hence, in the absence of a carbonation reaction and based upon the analysis presented in Table 1, a temperature increase of the effluent gas stream of 8.49 to 33.8 K would be predicted. As indicated in Figs. 16 to 23, such a temperature increase was not observed. Therefore, the authors speculate that the kinetic rates of hydration of $Ba(OH)_2 \cdot 3H_2O$ to $Ba(OH)_2 \cdot 8H_2O$ and $Ba(OH)_2 \cdot 7.47H_2O$ to $Ba(OH)_2 \cdot 8H_2O$ differ by at least an order of magnitude. Such is not totally surprising as the hydration of $Ba(OH)_2 \cdot 3H_2O$ was modeled via an advancing interface-type model (shrinking or expanding core model applied to planar geometry) and one might expect the formation of such a distinct interface to be less favored for the more fully-hydrated $Ba(OH)_2 \cdot 7.47H_2O$. Hence, it appears that the hydration mechanism is likely altered or impeded.

7. CHARACTERIZATION OF PRESSURE DROP PHENOMENA

The conditions for the treatment of high volumetric flow rates of air are restricted because of accompanying increases in the pressure drop across the fixed beds. Prior studies conducted under near-isothermal conditions led us to believe that the increases in pressure drop resulted form two phenomena.[22] First, conditions for the hydration of the substoichiometric reactant are often such that rapid recrystallization takes place and the particle curls as shown in Fig. 8. This curling then results in greater turbulence and an increase in pressure drop. Second, upon conversion to $BaCO_3$, the flakes are ~70% porous and are susceptible to degradation and subsequent plugging of pore spaces by fines, thus causing an increase in the pressure drop. Based upon the pressure drop data as presented in Fig. 7, we concluded that for successful process operation, the conditions of hydration must be such that the effluent relative humidity remains <60%. Furthermore, it was speculated that the increase in pressure drop likely results from the capillary condensation of water in V-shaped pores, a phenomenom that would become significant at

~60% relative humidity. It was also speculated that CO_2 sorption at relative humidities significantly >60% might be possible by use of a prior hydration of the bed at relative humdities <60%. However, the results of the pilot unit studies conducted under near-adiabatic conditions indicated:

(1) Prior hydration of the bed had minimal effect upon pressure drop during subsequent CO_2 sorption at humdities >>60%.

(2) The correlation of pressure drop data obtained under near-adiabatic and near-isothermal conditions was best when the correlation was based upon influent relative humidities (Fig. 24).

Pressure drop data and influent and effluent relative humidities for the eight runs are presented in Table 3. The system pressure used for relative humidity calculations was the average pressure which existed within the bed prior to termination of the run.

Therefore, based upon Fig. 24 and Table 3, it appears that hydration conditions may affect the pressure drop, but the principal effect is associated with the conditions of the CO_2-$Ba(OH)_2 \cdot 8H_2O$ reaction. More importantly, those conditions which exist during process start-up at the frontal edge of the mass transfer zone when the CO_2 concentration is great and the bed conversion is near unity appear to be very important. This factor will be addressed in the conclusion to this section.

In order to develop a better understanding of the flow characteristics of the gas stream through the fixed bed, the pressure drop across the bed was determined as a function of gas velocity for unreacted $Ba(OH)_2 \cdot 8H_2O$ and $BaCO_3$-product beds; the results are given in Table 4. The pressure drop for both the unreacted and reacted beds varied with V (the superficial velocity at system conditions) to the 0.94 to 1.22 power. Prior studies on the 10.2-cm-ID reactor had indicated the pressure drop across reacted beds to be proportional to $V^{1.4}$ (Table 5).[22] Data obtained on unreacted beds for these studies are of questionable quality because of instrumentation limitations.

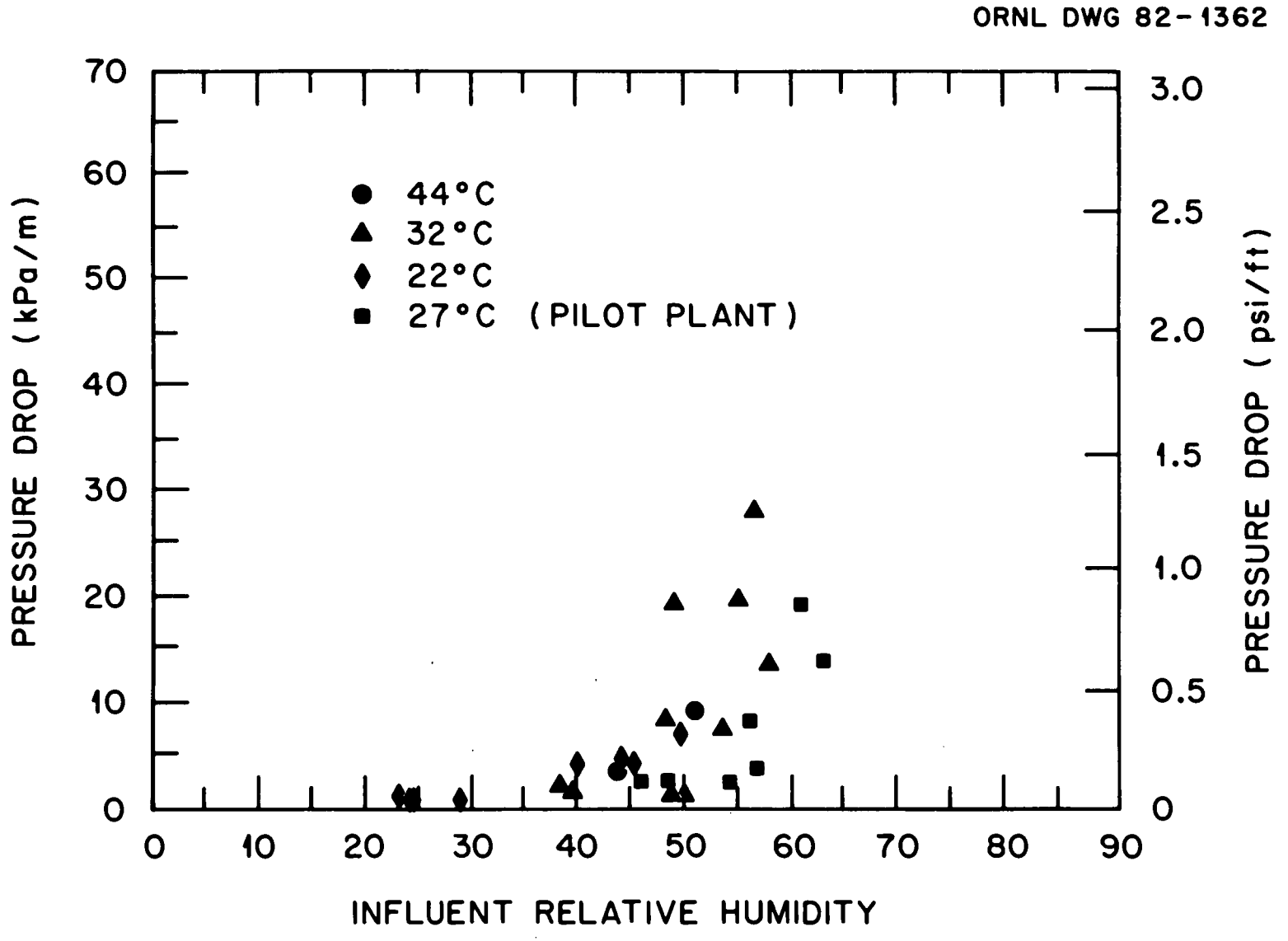

Fig. 24. Influent relative humidity.

Table 3. Data tabulation from pilot unit studies

Run	Superficial velocity (cm/s)	Influent relative humidity (%)	Effluent relative humidity (%)	Pressure drop (kPa/m)	$K_P A_0$ (s^{-1})
PP1	13.8	46.9	77.4	2.19	5.0
PP2	13.8	63.6	85.5	18.9	5.0
PP3	13.8	49.4	79.2	2.51	5.0
PP4	13.8	54.9	77.6	2.24	5.0
PP5	13.8	57.8	90.1	3.83	5.0
PP6	13.8	65.2	91.9	13.7	8.0
PP7	13.8	57.4	97.2	7.92	5.0
PP8	20.1	69.9	94.4	4.37	8.0

Table 4. Pressure drop correlation, $\Delta P/L = BV^n$, (kPa/m), for fixed beds of $Ba(OH)_2 \cdot 8H_2O$ and $BaCO_3$

Sample	-ln(B)	n[a]	Correlation coefficient
$Ba(OH)_2 \cdot 8H_2O$:			
PP5-A	2.5716	1.145	0.9983
-B	2.0391	0.975	0.9986
PP6	2.3365	0.943	0.9933
$BaCO_3$:			
PP4	2.0974	1.012	0.9972
PP5-A	1.5246	1.219	0.9999
-B	1.3857	1.116	0.9999
PP6	-0.5644	1.117	0.9999

[a]Average value of n = 1.075.

Table 5. Application of the model $\Delta P/L = BV^n$, (kPa/m), for correlating pressure drop across converted beds of commercial $Ba(OH)_2 \cdot 8H_2O$ flakes. (V has units of cm/s)

COM run No.	Relative humidity (%)	Superficial velocity V_o (cm/s)	Temperature (K)	n[a]	-ln(B)	Correlation coefficient
54	47.8	13.65	317.5	1.35	2.55	0.992
50	48.5	8.73	296.3	1.40	1.98	0.997
53	53.1	8.89	303.9	1.46	1.92	0.998
52	54.2	8.66	296.2	1.38	2.22	0.993
56	54.8	14.16	316.2	1.35	1.59	0.997
49	54.9	13.94	305.3	1.48	1.65	0.998
55	59.1	9.08	304.0	1.34	0.245	0.999
48	60.2	8.65	296.3	1.42	0.225	0.998
46	61.2	17.50	299.7	1.48	1.68	0.998
57	62.6	9.08	304.0	1.41	0.335	0.999
40	63.3	13.88	305.2	1.44	0.315	0.999
45	66.4	18.50	296.1	1.29	-1.05	0.999
47	69.6	8.93	296.0	1.41	-0.415	0.999

[a] $n(\text{average}) = 1.40$, $\sigma = 0.058$.

In the prior study, attempts to model the pressure drop via a form of the Ergun equation, $\Delta P/L = AV + BV^2$ in which A and B are physically consistent with the system of interest, failed. In the Ergun equation, the AV and the BV^2 terms generally account for the pressure drop contributions of the shear and turbulent or inertial forces. Hence, because of the decreased functional dependancy of superficial velocity on pressure drop for the present studies (n = 1.08 versus 1.40), the gas stream flow patterns in these studies appear to be less turbulent than those of the preceding studies. One possible factor contributing to this deviation is that the reactant was constrained in the prior studies and bed expansion was nominal, whereas considerable bed expansion (~1.5 in.) did occur during a typical run with the pilot unit. The effect of the differing flow patterns upon the mass transfer characteristics will be discussed in the next section.

8. MASS TRANSFER PROCESS MODELING

The modeling of mass transfer processes occurring within fixed beds has been studied extensively by Haag[22] in a preceding publication. In that work, a mass transfer model of the $Ba(OH)\cdot 8H_2O$ process for CO_2 sorption under near-isothermal conditions was developed. The intent of this section will be to review that model and to extend its application to the present system of interest.

8.1 MODEL FORMULATION AND SOLUTION

Based upon an analysis and comparison of the Thiele Modulas, the Damkoler number, and the Biot number and observed trends in the experimental data, mass transfer of CO_2 through the gas film surrounding the flaked particles was considered the most likely controlling resistance. Furthermore, upon an examination of the Peclet number and the observed CO_2 concentration profiles within the beds, the assumption was made that the effect of dispersion would be nominal. Based upon these assumptions, the controlling partial differential equation for the gas phase is:

$$\varepsilon \frac{\delta C}{\delta t} + V \frac{dC}{\delta z} = -K_F AC, \tag{20}$$

with the following boundary conditions:

$$C = 0 \qquad t = 0 \qquad z > 0$$

$$C = C_o \qquad t > 0 \qquad z = 0$$

The controlling partial differential equation (PDE) for the solid phase is:

$$\frac{\rho}{MW} \frac{\delta X}{\delta t} = K_F AC \tag{21}$$

with a boundary condition of $X = 0$, $t = 0$, $z > 0$.

where

ε = bed voidage,

C = concentration (mol/cm^3),

C_o = influent concentration,

t = time (s),

V = superficial gas velocity (cm/s),

z = axial distance (cm),

K_F = gas film mass transfer coefficient (cm/s),

A = area available for mass transfer (cm^2/cm^3),

ρ = bulk density of solid (g/cm^3),

MW = reactant molecular weight (~308), and

X = fractional reactant conversion.

The reactant used in these studies was flake-like in nature and the particle thickness varied by a factor of two or greater. A shrinking-core model, assuming planar geometry, was used for modeling purposes. The following empirical equation was used since the surface area available for mass transfer would vary with fractional conversion due to the varying particle thickness and because of the complexities in developing an exact correlation [i.e. $A = f(X)$]:

$$A = A_0 (1 - X^n) \tag{22}$$

where A_0 = initial area available for mass transfer, and n = arbitrary constant. A numerical solution was required because of the nonlinear nature of the preceding partial differential equations. However, the complexity of the solution and the computer time required to obtain a solution was reduced by the following change of variables:

$$\Theta = t - \frac{\varepsilon z}{V} \quad ; \quad S = \frac{z}{V} \quad ; \text{ and } \overline{C} = \frac{C}{C_o} . \tag{23}$$

The transformed partial differential equations were then of the form:

$$\frac{\delta \bar{C}}{\delta S} = -K_F A_0 (1-X^n)\bar{C} , \qquad \bar{C} = 1 \quad S = 0 \quad \Theta > 0 \tag{24}$$

$$\frac{\rho}{MW} \frac{\delta X}{\delta \Theta} = K_F A_0 (1 - X^n)\bar{C}, \qquad X = 0 \quad S > 0 \quad \Theta = 0 \tag{25}$$

Solutions to these equations were obtained via the application of finite difference techniques. Because of stability problems in obtaining a solution to the original PDE's (functions of t and z), the preceding transformation into the θ and s planes reduced the required computer time by 3 to 5 orders of magnitude. The development of the concentration profile as a function of Θ and S is presented in Fig. 25. For large values of Θ, $\Theta \approx t$

(i.e. $\Theta = t - \frac{\varepsilon z}{\bar{V}}$, $t >> \frac{\varepsilon z}{\bar{V}}$).

Upon the development of a concentration profile within the bed, a pseudo-steady state condition exists and the concentration and conversion profiles then advances through the bed essentially unchanged for all larger values of Θ or t (Figs. 25 and 26). The conversion profile within the bed behaves in an analogous manner. Comparison of the developed concentration and conversion profile, functions of Θ and S, respectively, indicated that they are essentially identical. The developed conversion and concentration profiles are shown in Fig. 27 as a function of $K_F A_0$, S, and assuming $A = A_0(1-X)$. (The empirical expression for A was determined via a fit of the model-predicted breakthrough curves for various A=f(X) with the experimental breakthrough curves.) With knowledge of the concentration profile within the bed or as a function of S, the breakthrough curve may be determined for a given z_o and t_o value via the equation:

$$z - z_o = \bar{V}(t-t_o) \tag{26}$$

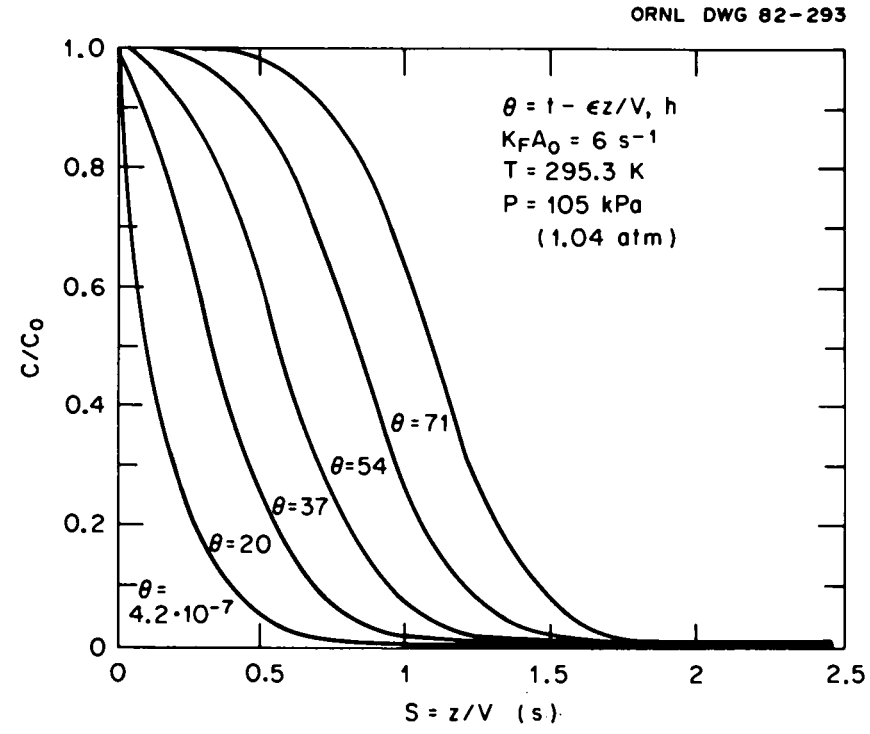

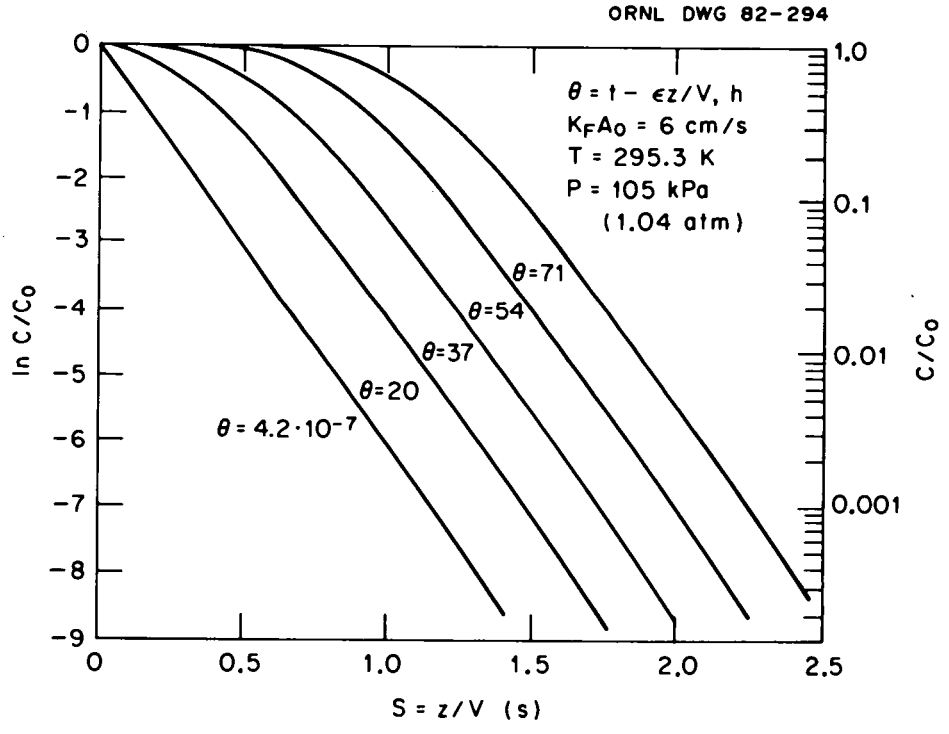

Fig. 25. Development of the concentration, and the natural logarithm of the concentration, profiles as a function of Θ and S.

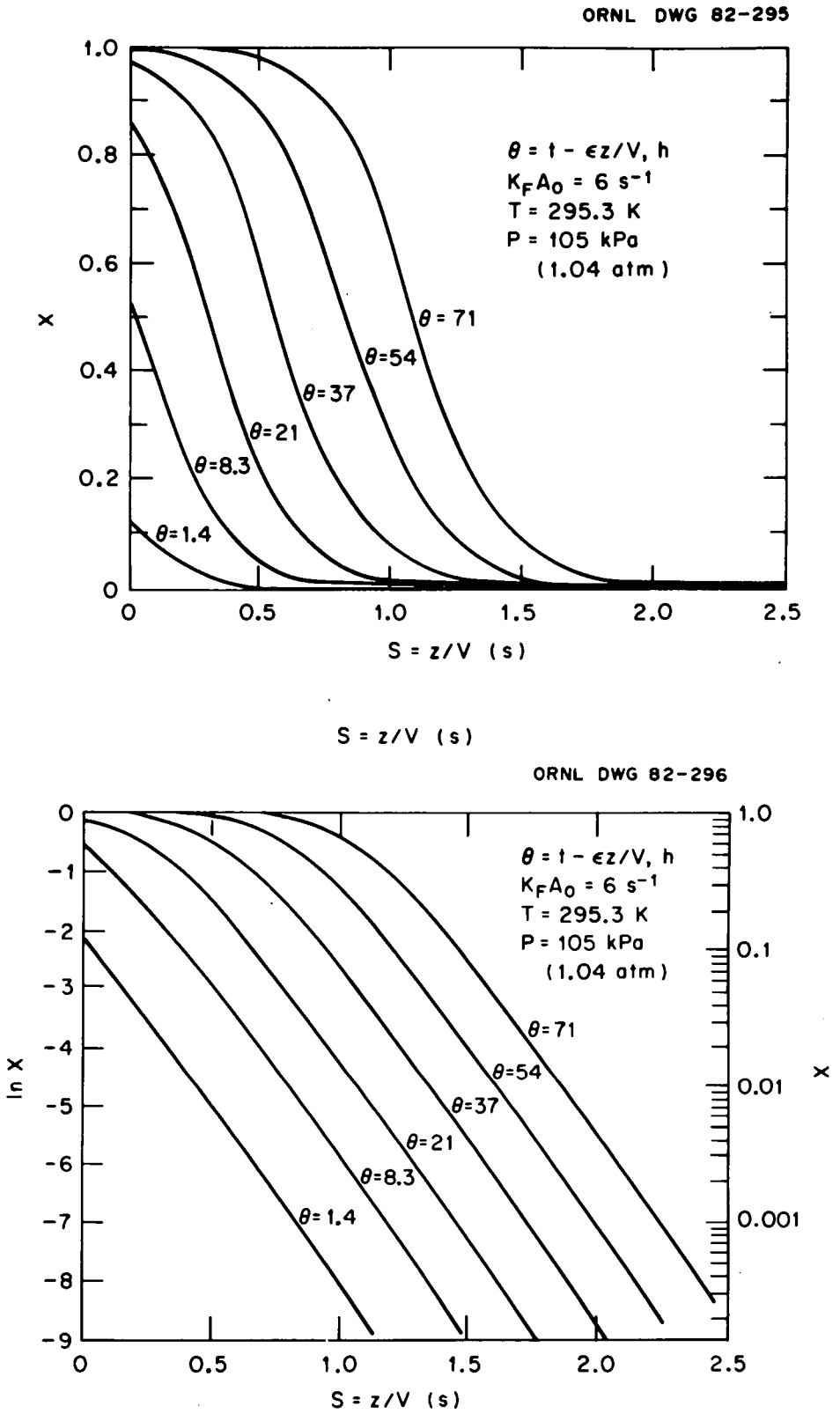

Fig. 26. Development of the conversion, and the natural logarithm of the conversion, profiles as a function of Θ and S.

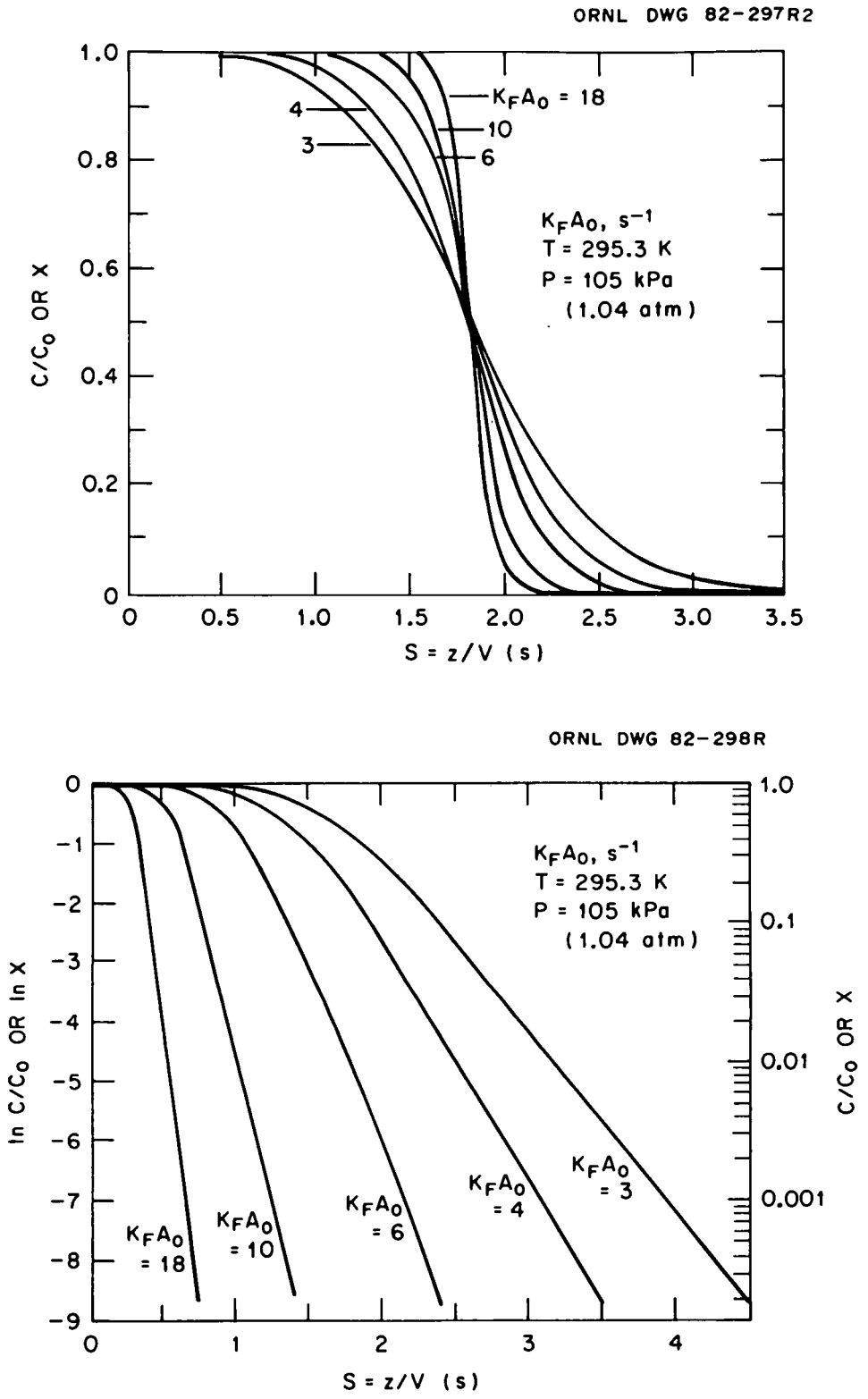

Fig. 27. Developed concentration or conversion, and natural logarithm of developed concentration or conversion, profiles as a function of the K_FA_o coefficient and S.

where

V = rate of movement of mass transfer zone (cm/s) = (MW)(V)(C_o/ρ).
The results of this transformation for varying values of K_FA_0 are provided in Fig. 28. The functional dependancy of superficial velocity upon the breakthrough curve appears only in the magnitude of K_FA_0, not in the transformation because of the terms involved in the transformation. This is not the case for the conversion profile within the bed whose length is a linear function of velocity since S = z/V.

8.2 DETERMINATION OF K_FA_0 COEFFICIENTS

Values for the K_FA_0 coefficients were determined (Figs. 29 to 32) and are presented in Table 2 by overlaying the model-predicted breakthrough curves developed in the preceding section onto the experimental breakthrough curves. The data was reasonably consistent and indicated a K_FA_0 ≈5 to 8 s^{-1}. Prior studies at a similar superficial velocity (≈13.8 cm/s) on the isothermal 10.2-cm-ID reactor had indicated the K_FA_0's of 7 to 10 s^{-1}. Hence, values for the adiabatic system are noticeably less than for the isothermal system at similar conditions. This observation is consistent with prior pressure drop studies from which it was speculated that the decreased pressure drop dependency upon superficial velocity for the adiabatic system (as compared to the isothermal system) resulted from the expansion of the bed in the former case. Pressure drop dependancy upon velocity is an indication of the tortuosity of the flowpath of the gas stream through the bed and hence the extent of turbulence. Thus, a lower value of the modified mass transfer coefficient, K_FA_0, is consistent with less turbulance and the observed reduction in pressure drop dependancy with velocity (i.e. $\Delta P/L \propto V^{.95}$ to $V^{1.20}$ for adiabatic studies as opposed to $\Delta P/L \propto V^{1.40}$ for isothermal studies, see Sect. 7).

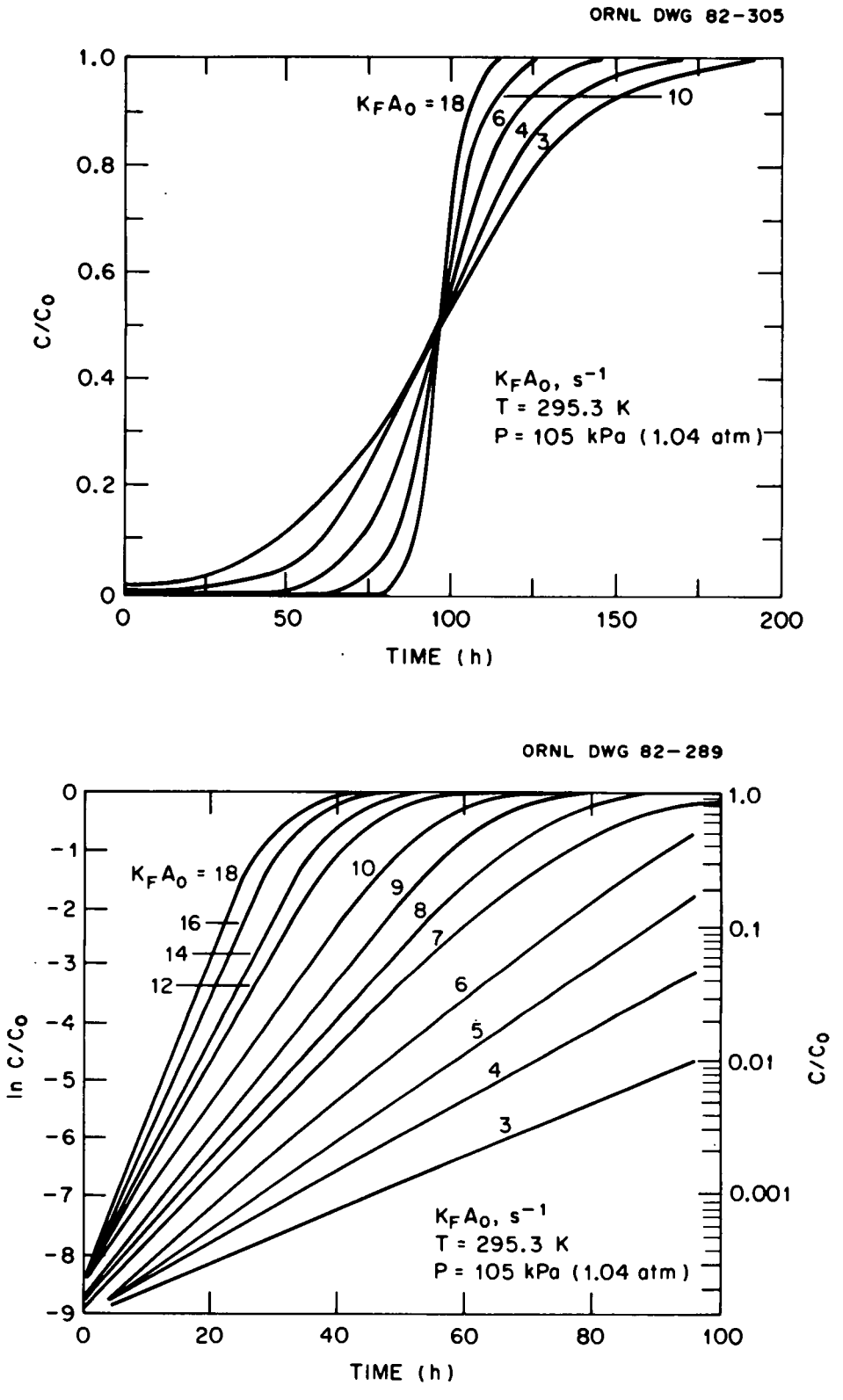

Fig. 28. Developed breakthrough, and the logarithm of the developed breakthrough, profiles as a function of the K_FA_0 coefficient and time.

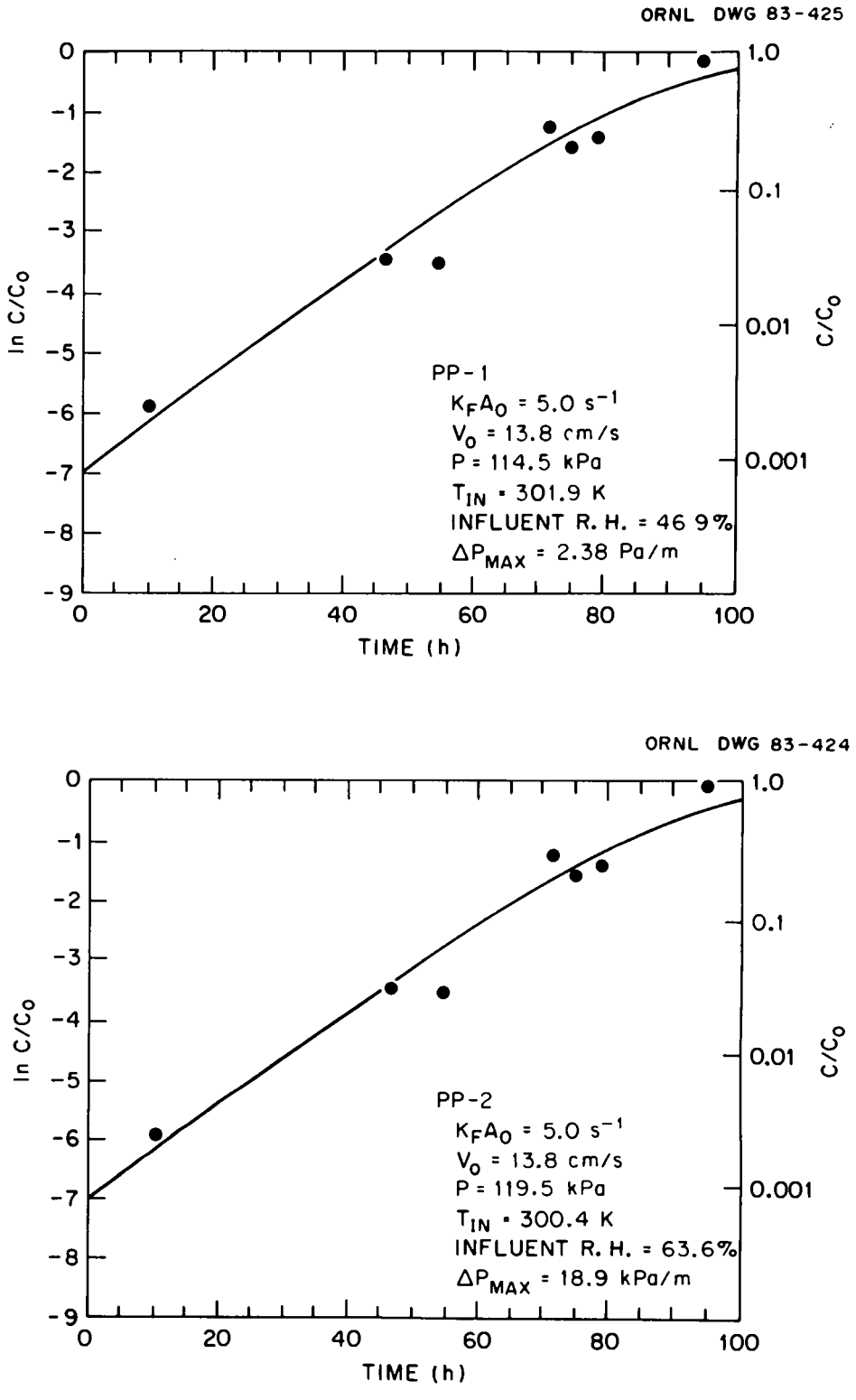

Fig. 29. Breakthrough overlays for Runs PP-1 and PP-2.

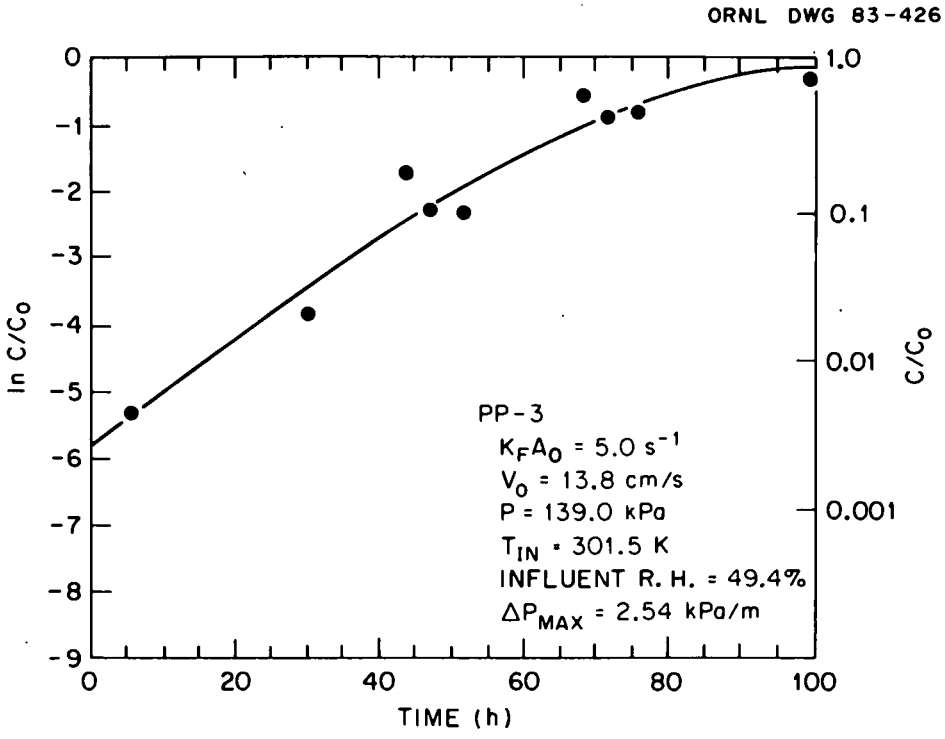

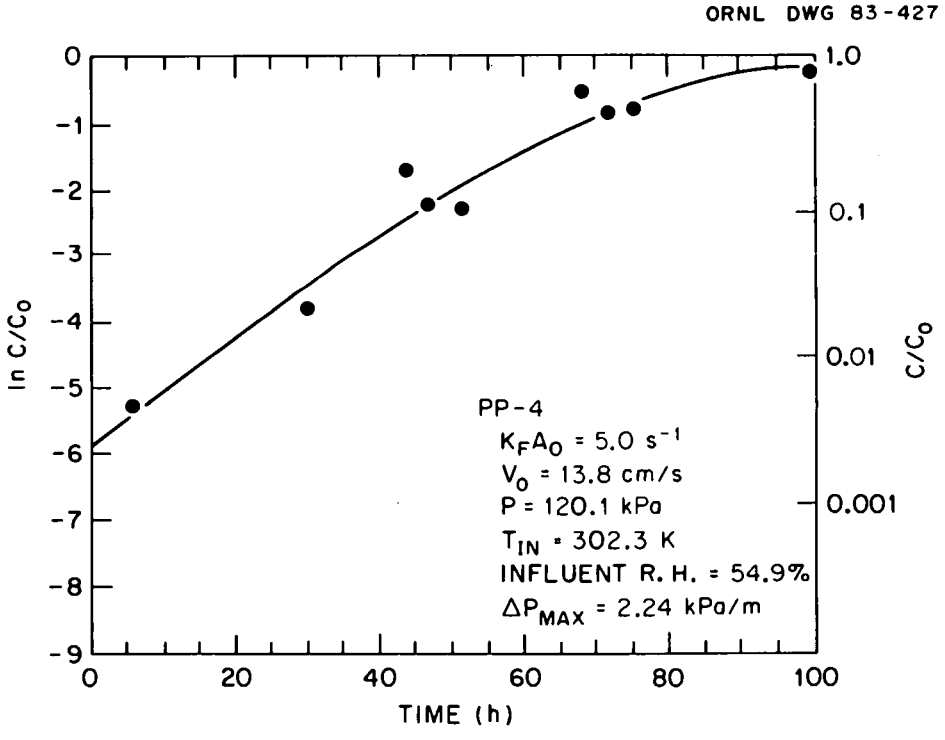

Fig. 30. Breakthrough overlays for Runs PP-3 and PP-4.

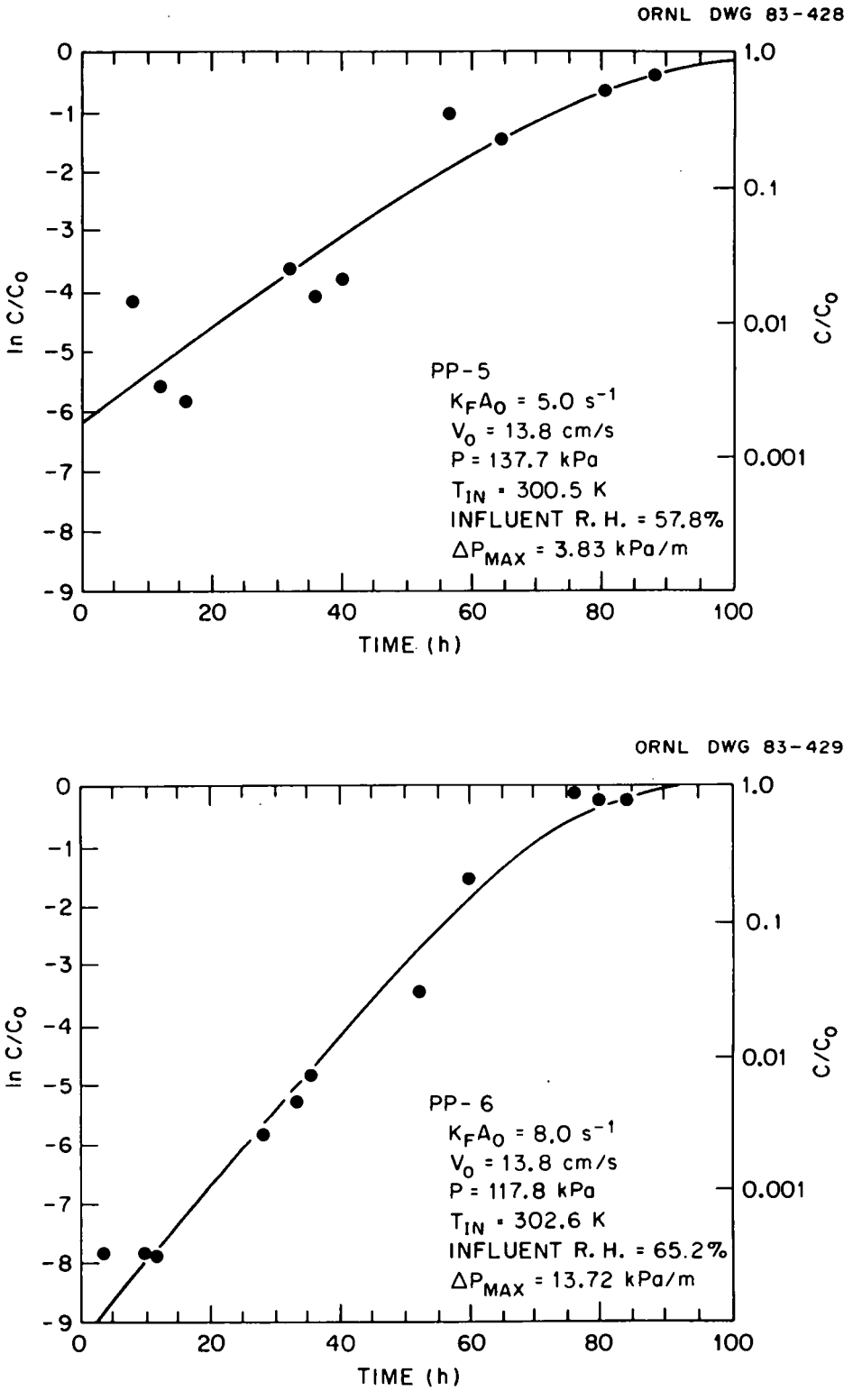

Fig. 31. Breakthrough overlays for Runs PP-5 and PP-6.

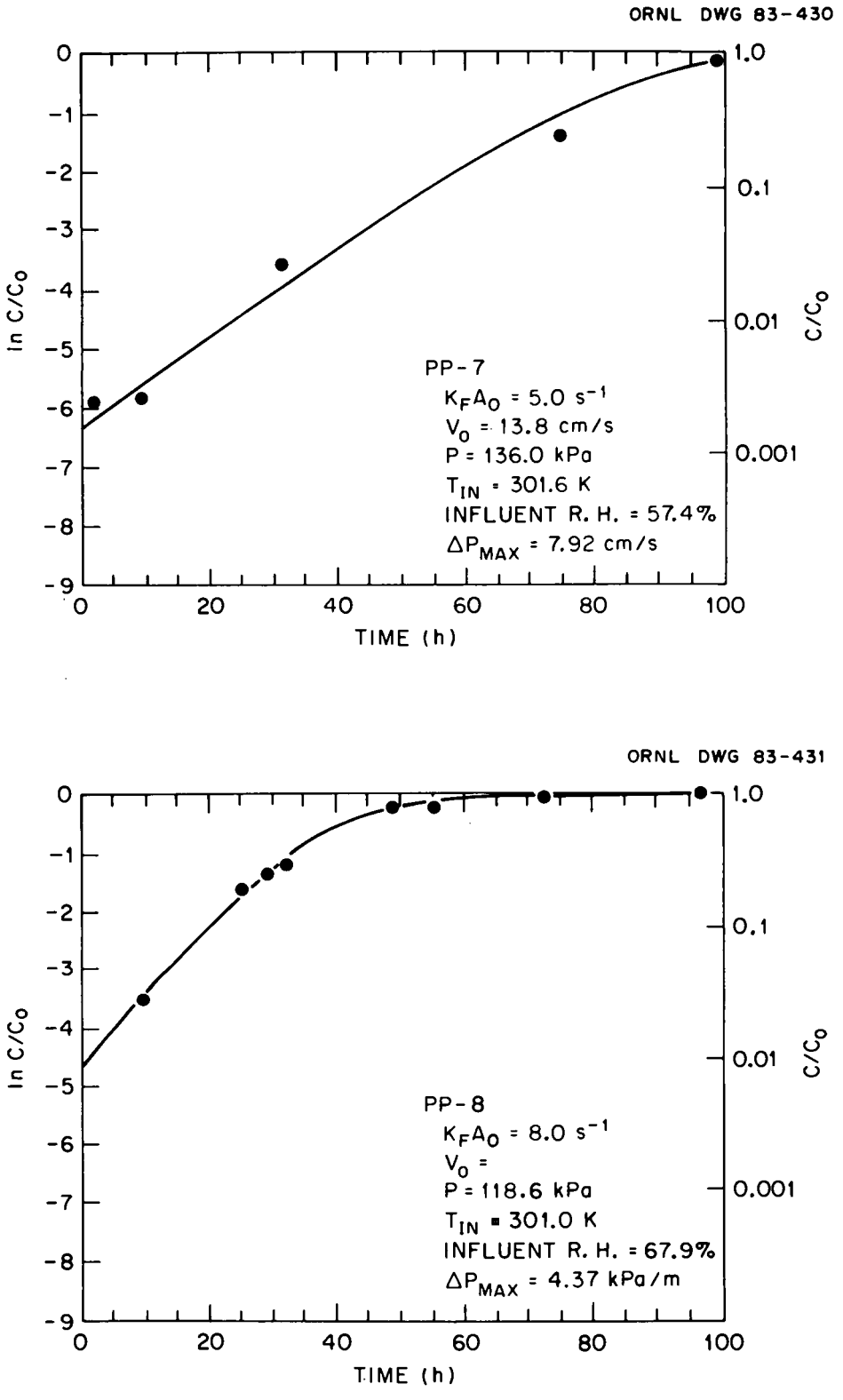

Fig. 32. Breakthrough overlays for Runs PP-7 and PP-8.

9. OBSERVATIONS FROM PILOT PLANT OPERATIONS

Successful operation of the $Ba(OH)_2 \cdot 8H_2O$ process has been demonstrated under near-adiabatic and near-isothermal conditions. When operating at water vapor pressures where $Ba(OH)_2 \cdot 8H_2O$ is stable, high CO_2 removal efficiencies and high reactant utilizations were routinely observed. A major factor of concern in the successful operation of this process has been the observed increased in pressure drop associated with increases in the the relative humidity of the process stream.

Studies on the 10.2-cm-ID reactor under near-isothermal conditions indicated that an operating envelope existed. The lower constraint results from the requirement that the influent water vapor pressure must be greater than the dissociation vapor pressure of $Ba(OH)_2 \cdot 8H_2O$, e.g., 775 Pa (5.8 mm Hg) at 22°C and 1.64 kPa (12.3 mm Hg) at 32°C. With respect to the upper limit of the envelope, isothermal studies at 22 and 32°C indicated that the onset of significant increases in pressure drop could be correlated with relative humidity of the influent or effluent as opposed to water vapor pressure which is indicative of a surface adsorption phenomenon. For the isothermal studies, the effluent relative humidity differed from the influent value by the contribution from the water reaction product (relative humidity increased ~6.3% at 32°C, ~11.4% at 22°C). In Fig. 7, we could not distinguish a unique dependency upon either influent or effluent relative humidities. However, we observed recrystallization and curling of the sub-stoichiometric flakes when hydration occurred and also the onset of appreciable pressure drop at ~60% relative humidity, possibly attributed to the capillary condensation of water in pores and rapid recrystallization. Therefore, we speculate that the controlling condition is the effluent relative humidity which is when the bulk of the bed hydration has occurred. It was hypothesized that the flakes which hydrated at relative humidities >60% were more fragile and degraded upon conversion to $BaCO_3$.

Consistency of the pressure drop data from the pilot studies performed under near-adiabatic conditions was possible only when influent relative humidities were compared (Fig. 33). Table 2 shows that the

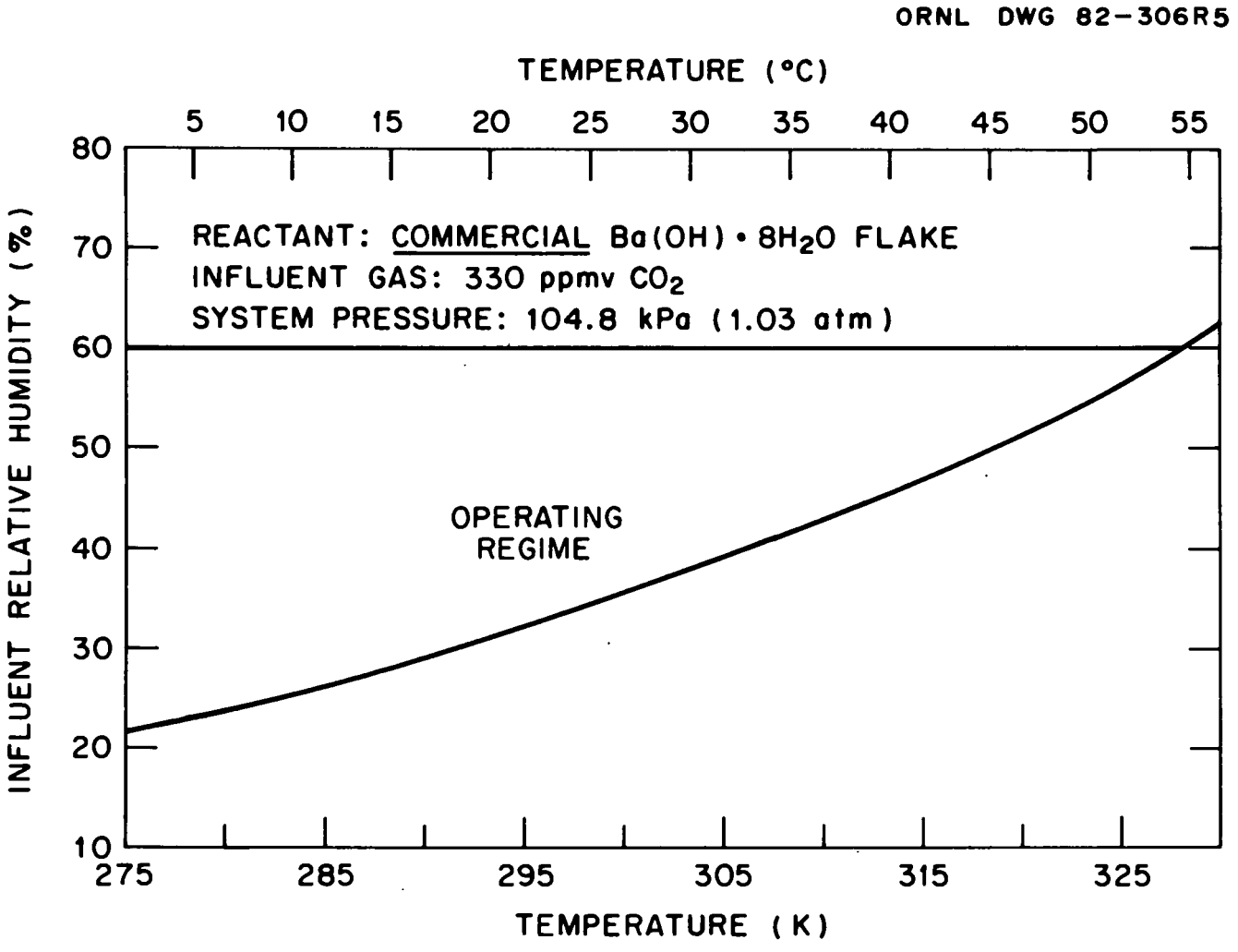

Fig. 33. Proposed operating regime of process operability for treating air-based (330-ppm_v-CO_2) gas streams under isothermal and adiabatic conditions.

influent and effluent relative humidities could be distinguished since the latter were 30% greater. Furthermore, if the preceding hypothesis, based upon effluent relative humidity and hydration of reactant was correct, one could then prehydrate a bed at relative humidities <60% and then operate the CO_2 sorption process at relative humidities >>60%. But experimental studies on the pilot unit indicated that prior hydration had little if any effect upon pressure drop; pressure drop was nominal for effluent relative humidities >>60%. Furthermore, consistency of isothermal and adiabatic pressure drop data was possible when the analysis was based upon influent relative humidity. The ramifications of these observations are striking since the regime of process operability is greatly increased. The regime, based upon influent relative humidity, is limited on the lower side by the dissociation vapor pressure of $Ba(OH)_2 \cdot 8H_2O$ and on the upper side by ~60% relative humidity.

From a mechanistic perspective, these observations are more difficult to explain than the previous results since the portion of the unreacted bed contacting the gas stream at influent relative humidity conditions is small. However, the following hypothesis is presented: In Sect. 8, the process model predicted a period of time during which a pseudo-steady-state conversion and concentration profile developed within the bed. Based upon an analysis of the breakthrough curves, the rate of reaction within the bed was modeled via on expression of the form:

$$R_{CO_2} = K_F A_o C_o (1-X) X_{CO_2} \tag{27}$$

where

$K_F A_0$ = modified mass transfer coefficient (~5 s^{-1}),

C_o = inlet CO_2 concentration (~$1.35 \cdot 10^{-5}$ mol CO_2/L),

X = $Ba(OH)_2 \cdot 8H_2O$ fractional conversion, and

X_{CO_2} = CO_2 fraction remaining.

After development of the conversion and concentration profiles within the bed, the model predicts that the fractional conversion of gas and the fraction of solid reactant (1-X) will be approximately equal.

Therefore, the maximum rate of reaction under those conditions would occur at $X = 0.5$ and $X_{CO_2} = 0.5$ or:

$$R_{CO_2} = (5)(1.35)(10^{-5})(0.5)(0.5) = 1.69 \cdot 10^{-5} \text{ mol } CO_2/(L \cdot s)$$

However, $X_{CO_2} = 1.0$ and $X = 0.0$ upon the start-up of a run and the corresponding rate of reaction is:

$$R_{CO_2} = (5)(1.35)(10^{-5})(1)(1) = 6.75 \cdot 10^{-5} \text{ mol } CO_2/(L \cdot s)$$

or four times greater than the maximum observed during the normal operation of the bed; i.e., in the presence of developed concentration and conversion profiles. Perhaps the conditions existing within the bed during process start-up are crucial with respect to significant increases in pressure drop. Therefore, the influent relative humidity, the heat requirement to raise the bed to process conditions ($\sim\Delta 5°C$), the exothermic hydration reaction, and the endothermic carbonation reaction appear to be important factors during the formation of the developed conversion and concentration profiles. If this is the case, one would expect the pressure drop across downstream columns situated in series, which would only experience developed conversion and concentration profiles, would be expected to be considerably less. Unfortunately, testing this hypothesis is not possible as all runs for a given superficial velocity were performed on a bed using a similar start-up procedure ($X_{CO_2} = 1.0$ and $X = 0.0$) and possessing similar length. In these studies, the total pressure drop across the bed was monitored (not the pressure drop across bed segments). However, the physical characteristics of the $BaCO_3$ product support the hypothesis. Typically, the lower portions of the bed (the zone of rapidly developing conversion and concentration profiles) were severely degraded and in several cases a porous plug formed; but the extent of deviation from the initial flake-form decreased further up the bed. The increase in pressure drop was not continuous with conversion, but occurred largely

during the early portion of the run. Therefore, the increase in pressure drop at ~60% relative humidity may not be observed for successful process operation with developed conversion and concentration profiles. For those conditions, the upper limit of process operability (as presented in Fig. 33) would be relaxed (increased); but additional studies would be required to verify that hypothesis.

10. CONCLUSIONS

Process technology for the removal of $^{14}CO_2$ from air-based gas streams via the $Ba(OH)_2 \cdot 8H_2O$ process has been demonstrated at the bench- and pilot- scales. The process is capable of high CO_2 removal efficiencies (effluent concentrations <100 ppb), high reactant utilizations (>99% conversion), and possesses acceptable operational properties at near-abmient conditions. Although a comprehensive cost analysis was not conducted, the technology is cost competitive with other suggested technologies for $^{14}CO_2$ removal and disposal. Those process alternatives include (1) the double alkali process (NaOH scrub with $Ca(OH)_2$ backscrub), (2) the Ca(OH) slurry reactor, and (3) CO_2 sorption on molecular seive with subsequent fixation via $Ca(OH)_2$ slurry. Therefore, based upon cost analyses for the above processes for $^{14}CO_2$ removal and disposal, we estimate a process cost of <$10/man-rem for the treatment of the air-based off-gas stream at a 1500 MTHM [45 GW(e)·y] LWR fuel reprocessing plant. Assuming a 500 ft^3/min air-based gas stream, 14 Curies/MTHM, a dosage of 400 to 590 Curie/man-rem, the reactant cost ($0.43/lb, June, 1981) would be ~$0.10/man-rem or ~$88/day. The process would generate ~60 kg/day (131 lb/day) or 0.093 m^3/day (3.3 ft^3/day) of $BaCO_3$. By prior CO_2 removal from air-based streams, which are used to agitate process vessels and purge process cells, the waste handling and process costs could be significantly reduced. Experimental studies have shown no difficulties in obtaining a process decontamimation factor of 100 for an influent gas stream of 10 ppm, since effluent concentrations of <100 ppb were routinely observed during experimental studies. However, absolute measurement of

concentrations <100 ppb were not possible because of instrumentation limitations. Thermodynamically, no restrictions were predicted for concentrations down to the part-per-trillion level.

The flaked reactant used in this study was purchased from the Sherwin Williams Company and manufactured at their Coffeyville Plant, Coffeyville, KS. We were notified that the product was being discontinued because of a lack of demand and they were uncertain as to the possibility of a competitor producing the flaked product or of eventually resuming production.[34] G. L. Haag visited the plant and the plant process was discussed in detail; it is extremely simple and appears to require minimal control. It consists of distributing a $Ba(OH)_2 \cdot 8H_2O$ magma (~78°C) on a stainless steel conveyor belt, which is 1 m (40 in.) wide and ~5 m (16 ft) long. The underside of the belt is cooled with process water such that the magma solidifies prior to falling off the conveyor belt, whereupon it falls into a hopper and is conveyed with augers. The flakes are variable in thickness with an average thickness of 3 mm (1/8 in.). Safety standards for the process were not stringent. If a flaked form is not commercialy available, we envision no major difficulty or appreciable increase in cost/man-rem in using particulate $Ba(OH)_2 \cdot 8H_2O$ and contracting the flake-forming operation to a second party. Particulate $Ba(OH)_2 \cdot 8H_2O$ is readily available in commercial quantities and experimental studies have indicated the precise hydration stoichiometry of the flake to not be extremely critical. Sherwin-Williams specifications indicate reactant stoichiometries of $Ba(OH)_2 \cdot 7.1H_2O$ to $Ba(OH)_2 \cdot 7.8H_2O$. Our analysis of their material indicated $Ba(OH)_2 \cdot 7.5H_2O$. For future testing purposes, ~1,000 lbs of the flaked reactant remain at ORNL from this study.

Operation at superficial velocities >>13 cm/s must be approached with caution because of potential pressure drop problems and additional bed expansion and gas channeling. Studies were not conducted as to the effect of influent CO_2 concentrations >330 ppm. The shape of the concentration and conversion profiles within the bed and the resulting breakthrough curves may be predicted by using the process model developed during these studies. From an operational standpoint, we should consider the possibility of saturating the gas stream with water vapor, because of the

increased reaction rate and the accompanying decrease in water content at saturation (because of a reduction in gas stream temperature causing greater net endothermicity). Furthermore, the potential for a significant increase in pressure drop during the initial start-up of the process, prior to the formation of the pseudo steady-state conversion and concentration profiles, must be evaluated. No detailed studies were conducted on the effects of process operation under water-saturation conditions. However, efficient CO_2 removal from an 80% CO_2 gas stream was observed even though the reaction was exothermic and water condensed within the bed. Based upon the speculation in the preceding section and the increase in pressure drop associated with conditions during process start-up (most notably for influent relative humidities >60%), pressure drop problems probably would increase for CO_2 concentrations >330 ppm and decrease for concentrations <330 ppm.

An alternative novel technology under development by Ontario Hydro-Canada using a high humidity, ambient temperature, CO_2-$Ca(OH)_2$ gas-solid reaction is of particular interest. For several years, we have exchanged ^{14}C immobilization information with Ontario Hydro via a DOE-approved exchange agreement. Because of the many analogies between the two systems, this exchange of information has been helpful and conducted in a cordial atmosphere. Continued monitoring of this work is recommended.

11. REFERENCES

1. H. Bonka, "Contamination of the Environment by Carbon-14 Produced in High-Temperature Reactors," Kerntechnik. 15(7):297 (1973).

2. W. Davis, Jr., Carbon-14 Production in Nuclear Reactors, ORNL/NUREG/TM-12 (February 1977).

3. C. D. Kunz, "Continuous Stack Sampling for ^{14}C at the R. E. Ginna Pressurized Water Reactor," Trans. Am. Nucl. Soc. 38: 100 (1981).

4. C. O. Kunz, W. E. Mahoney, and T. W. Miller, "Carbon-14 Gaseous Effluents from Boiling Water Reactors," Trans. Am. Nucl. Soc. 21: 91 (1975).

5. C. O. Kunz, W. E. Mahoney, and T. W. Miller, "C-14 Gaseous Effluent from Pressurized Water Reactors," pp. 229-34 in Proceedings of the Health Physics Society 8th Midyear Symposium, CONF-741018 (1974).

6. M. J. Kabat, "Monitoring and Removal of Gaseous Carbon-14 Species," Proceedings of the 15th DOE Nuclear Air Cleaning Conferference, CONF-780819 (1979).

7. H. Schuttelkopf, Releases of $^{14}CO_2$ from Nuclear Facilities with Gaseous Effluents, Kernsforschungszentrum, Karlsruhe, KFK 2421, June 1977 (translated from German) ORNL-tr-4527 (1978).

8. Exxon Nuclear Idaho Company, Inc., Program Strategy Document for the Management of Radioactive Airborne Wastes — Draft, prepared for Department of Energy, Idaho Operations Office (1981).

9. P. J. Magno, C. B. Nelson, and W. H. Ellett, "A Consideration of the Significance of Carbon-14 Discharges from the Nuclear Power Industry," p. 1047 in Proceedings of the Thirteenth AEC Air Cleaning Conference, CONF-740807 (1975).

10. G. G. Killough, A Diffusion-Type Model of the Global Carbon Cycle for the Estimation of Dose to the World Population from Releases of Carbon-14 to the Atmosphere, ORNL/TM-5269 (1977).

11. G. C. Killough et al., Progress Report on Evaluation of Potential Impact of ^{14}C Releases from an HTGR Reprocessing Facility, ORNL/TM-5284 (1976).

12. L. Machta, "Prediction of CO_2 in the Atmosphere," in Carbon and the Biosphere, G. M. Woodwell and E. V. Pecan, eds., Technical Information Center, Office of Information Services, U.S. Atomic Energy Commission (August 1973).

13. J. W. Snider and S. V. Kaye, "Process Behavior and Environmental Assessment of ^{14}C Releases from an HTGR Fuel Reprocessing Facility," in Proceedings of the ANS-AIChE Topical Meeting, Sun Valley, Idaho, Aug. 5-6, 1976.

14. L. Pauling, "Genetic and Somatic Effects of Carbon-14," Science 128: 1183 (1958).

15. J. Schwibach, H. Riedel, and J. Bretschneider, Studies on the Emission of Carbon-14 from Nuclear Facilities (Nuclear Power Plants and Reprocessing Plants): Its Measurement and the Radiation Exposure Resulting from Emissions, Series of the Institute for Radiation Hygiene of the Federal Health Office, 20 (translated from German), OLS-80-233, Oak Ridge National Laboratory, Oak Ridge, TN (1979).

16. Radiological Significance and Management of Tritium, Carbon-14, Krypton-85, Iodine-129 Arising from the Nuclear Fuel Cycle, Nuclear Energy Agency, Organization for Economic Cooperation and Development, Paris, France (1980).

17. G. G. Killough and P. S. Rohwer, "A New Look at the Dosimetry of ^{14}C Released to the Atomsphere as Carbon Dioxide," Health Phys. 4: 141 (1978).

18. G. G. Killough et al., "Dose Equivalent due to Atmospheric Releases of Carbon, Chap. 11 in Models and Parameters for Environmental Radiological Assessment, C. W. Miller, Ed., (1984), DOE/TIC-11468.

19. G. G. Killough and J. E. Till, "Scenarios of ^{14}C Releases from the World Nuclear Industry from 1975 to 2020 and the Estimated Radiological Impact," Nucl. Saf. 19(5): 602 (1978).

20. T. W. Fowler and C. B. Nelson, Health Impact Assessment of Carbon-14 Emissions from Normal Operations of Uranium Fuel Cycle Facilities, EPA 520/5-80-004 (1981).

21. G. L. Haag, "Carbon-14 Immobilization via the CO_2–$Ba(OH)_2$ Hydrate Gas-Solid Reaction," in Proceedings of the 16th DOE Nuclear Air Cleaning Conference, CONF-801038 (1981).

22. G. L. Haag, Application of the CO_2-$Ba(OH)_2 \cdot 8H_2O$ Gas-Solid Reaction for the Treatment of Dilute CO_2-Bearing Gas Streams, Ph.D. Dissertation, University of Tennessee, Knoxville, 1982;

ORNL-5887 (Sept. 1983).

23. Handbook of Chemistry and Physics, 52nd ed., The Chemical Rubber Co., Cleveland, Ohio, 1972, pp. 13-70.

24. W. F. Linke and A. Seidell, Solubilities of Inorganic and Metal Organic Compounds, 4th ed., American Chemical Society, Washington, D.C., 1958.

25. A. G. Croff, An Evaluation of Options Relative to the Fixation and Disposal of ^{14}C-Contaminated CO_2 as $CaCO_3$, ORNL/TM-5171 (1976).

26. A. G. Evans et al., Management of Radioactive Waste Gases from the Nuclear Fuel Cycle — Volume 1, Comparison of Alternatives, NUREG/CR-1546, DPST-NUREG-80-5, vol. 1 (1980).

27. D. W. Holladay, Experiments with a Lime Slurry in a Stirred Tank for the Fixation of Carbon-14 Contaminated CO_2 from Simulated HTGR Fuel Reprocessing Off-Gas, ORNL/TM-5757 (1978).

28. D. W. Holladay, An Experimental Investigation of the Distribution of Krypton from Simulated HTGR Fuel Reprocessing Off-Gas During the Removal and Fixation of CO_2 by the CO_2-$Ca(OH)_2$ Slurry Reaction, ORNL/TM-6539, (1982).

29. D. W. Holladay and G. L. Haag, "Removal of ^{14}C-Contaminated CO_2 from Simulated LWR Fuel Reprocessing Off-Gas by Utilizing the Reaction Between CO_2 and Alkaline Hydroxides in Either Slurry or Solid Form," pp. 548-69 in Proceedings of the 15th DOE Nuclear Air Cleaning Conference, CONF-780819 (1979).

30. K. J. Notz et al., "Processes for the Control of $^{14}CO_2$ During Reprocessing," presented at the International Symposium on Management of Gaseous Wastes from Nuclear Facilities, Vienna, Austria, Feb. 18-22, 1980.

31. G. R. Bray et al., Assessment of Carbon-14 Control Technology and Costs for the LWR Fuel Cycle, EPA 520/4-77-013 (1977).

32. J. L. Kovach, Review of Carbon-14 Control Technology and Cost, NUCON 8EP555/01, Nuclear Consulting Services, Inc., Columbus, Ohio (1979).

33. G. L. Haag, Carbon-14 Immobilization Via the $Ba(OH)_2$ $8H_2O$ Process, ORNL/TM-5926 (March 1983).

34. J. Nillis, Sherwin Williams Co., Coffeeville, KS., personal communication to G. L. Haag, 1981.

35. M. Michaud, "Contribution to the Study of the Hydroxides of Potassium and Barium," Rev. Chim. Minerale t.5: 89 (1968).

36. M. Michaud, Inorganic Chemistry — Study of the Binary Water—Barium Hydroxide System, C. R. Acad. Sci. Paris 262.CV: 1143 (1966).

37. B. A. Kondakov, P. V. Kovtunenko, and A. A. Bundel, "Equilibria Between Gaseous and Condensed Phases in the Barium Oxide—Water System," Russ. J. Phys. Chem. 38(1): 99-102 (1964).

38. H. Manohar and S. Ramaseshan, "The Crystal Structure of Barium Hydroxide Octahydrate—$Ba(OH)_2$ $8H_2O$," Zeit. fur Kristall. Bd. 119, 357 (1964).

39. P. K. Warme, Curve Fitter, Interactive Microware, Inc., State College, Pa., 1980.

40. T. H. Chilton, and A. P. Colburn, "Mass Transfer (Absorption) Coefficients, Prediction from Data on Heat Transfer and Fluid Friction," Ind. Eng. Chem. 26 1183 (1934).

41. R. B. Bird, W. E. Stewart, and E. N. Lightfoot, Transport Phenomenom, Wiley, New York, 1960.

42. T. E. W. Schumann, "Heat Transfer: A Liquid Flowing Through a Porous Prism," J. Franklin Inst. 208, 405 (1929).

43. C. C. Furnas, "Heat Transfer from a Gas Stream to a Bed of Broken Solids," Ind. Eng. Chem. 22, 26 (1930).

ORNL-6100
Dist. Category UC-70

INTERNAL DISTRIBUTION

1. J. O. Blomeke
2. W. D. Burch
3. J. L. Collins
4. R. M. Counce
5. A. G. Croff
6. L. R. Dole
7. R. D. Ehrlich
8. C. S. Fore
9. C. Forsberg
10. R. W. Glass
11. D. C. Sampson
12. D. Holladay
13. E. K. Johnson
14. R. J. Jubin
15. M. V. Keigan
16. E. H. Kreig, Jr.
17. R. E. Leuze
18. J. C. Mailen
19. D. R. Moser
20. C. L. Ottinger
21-25. W. W. Pitt
26. T. H. Row
27. F. M. Scheitlin
28. M. B. Sears
29. B. B. Spencer
30. M. G. Stewart
31. O. K. Tallent
32. R. G. Wymer
33. G. C. Young
34-35. Central Research Library
36. ORNL-Y-12 Technical Library Document Reference Section
37. Laboratory Records Department
38. Laboratory Records, ORNL-RC
39. ORNL Patent Section

EXTERNAL DISTRIBUTION

DOE-Office of Assistant Secretary for Nuclear Energy (NE-1), Washington, D.C. 20545
40. J. W. Vaughen, Jr.

DOE-Office of Assistant Secretary for Defense Programs (DP-1), Washington, D.C. 20545
41. W. W. Hoover

DOE-Office of Civilian Radioactive Waste Management (RW-1), Washington, D.C. 20585
42. B. C. Rusche

DOE-Office of Support Programs (NE-70), Washington, D.C. 20545
43. E. F. Mastal

DOE-Office of Deputy Assistant Secretary for Nuclear Materials (DP-10), Washington, D.C. 20545
44. A. L. Taboas
45. G. H. Daly

DOE-Albuquerque Operations Office, P.O. Box 5400, Albuquerue, NM 87115
46. J. M. McGough

DOE-Chicago Operations Office, Bldg. 201, 9800 S. Cass Ave., Argonne, IL 60439
47. S. A. Mann

DOE-Columbus Program Office, 505 King Ave., Columbus, OH 43201
48. J. O. Neff

DOE-Idaho Operations Office, P.O. Box 1662, 550 2nd Street, Idaho Falls, ID 83401
49. R. H. Belks
50. J. B. Whitsett
51. M. A. Widmayer

DOE-Oak Ridge Operations, P.O. Box E, Oak Ridge, TN 37831
52. J. A. Lenhard

DOE-Office of Remedial Action and Waste Technology (NE-20), Washington, D.C. 20545
53. W. R. Voigt, Jr.

DOE-Richland Operations Office, P.O. Box 550, Richland, WA 99352
54. J. J. Schriber
55. M. Shupe

DOE-Savannah River Operations, P.O. Box A, Aiken, SC 29801
56. G. K. Oertel

Amoco Production Co., Research Center, 4502 East 41st Street, P.O. Box 591, Tulsa, OK 74102
57-61. Gary L. Haag

Argonne National Laboratory, 9700 S. Cass Ave., Argonne, IL 60439
62. M. J. Steindler
63. V. Trevorrow

Fermi National Accelerator Laboratory, P.O. Box 500, Batavia, IL 60510
64. J. G. Couch

Lawrence Livermore National Laboratory, P.O. Box 808, Livermore, CA 94550
65. W. Bergman

Los Alamos National Laboratory, P.O. Box 1663, Los Alamos, NM 87545
66. L. C. Borduin

Oak Ridge Gaseous Diffusion Plant, P.O. Box P, Oak Ridge, TN 37831
67. W. Golliher

EG&G Idaho, Inc., P.O. Box 1625, Idaho Falls, ID 83415
68. E. A. Jennrich

Pacific Northwest Laboratories, P.O. Box 999, Richland, WA 99352
69. T. D. Chihalla

Joint Integration Office, P.O. Box 3150, Albuquerque, NM 87190
70. J. V. Guerrero

SRL-E.I. duPont de Nemours & Co., Savannah River Laboratory, Aiken, SC 29801
71. E. L. Albenesius 72. J. L. Crandall

SRP-E.I. duPont de Nemours & Co., Savannah River Plant, Aiken, SC 29801
73. R. Maher

Y-12 Plant, P.O. Box Y, Oak Ridge, TN 37831
74. T. R. Butz

Battelle-Columbus Laboratories, 505 King St., Columbus, OH 43210
75. K. Brog

Georgia Institute of Technology, School of Chemical Engineering, Atlanta, GA 30332
76. D. W. Tedder

Goodyear Atomic, P.O. Box 628, Piketon, OH 45661
77. R. E. Anderson

Monsanto Research Corporation, Mound Facility, P.O. Box 32, Miamisburg, OH 45342
78. R. K. Blauvelt 79. M. L. Rogers

Nuclear Consulting Services, Inc., P.O. Box 29151, Columbus, OH 43229
80. J. L. Kovach

NUS Corporation, P.O. Box 369, Oak Ridge, TN 37831-0369
81. S. J. Bass

Pennsylvania State University, 202 Materials Research Laboratory, University Park, PA 16802
82. R. Roy

REECO, P.O. Box 642, Mercury, NV 89023
83. P. T. Dickman

Westinghouse Idaho Nuclear Company, Inc., P.O. Box 4000, Idaho Falls, ID 83403
84. D. A. Knecht

Given distribution as shown in TIC-4500 under category UC-70
85-388.